DESIGN AND ANALYSIS OF A COMPOSITE FLYWHEEL PRELOAD LOSS TEST RIG

A Thesis

by

JASON LEE PREUSS

Submitted to the Office of Graduate Studies of
Texas A&M University
in partial fulfillment of the requirements for the degree of

MASTER OF SCIENCE

May 2004

Major Subject: Mechanical Engineering

DESIGN AND ANALYSIS OF A COMPOSITE FLYWHEEL PRELOAD LOSS TEST RIG

A Thesis

by

JASON LEE PREUSS

Submitted to Texas A&M University
in partial fulfillment of the requirements
for the degree of

MASTER OF SCIENCE

Approved as to style and content by:

Alan Palazzolo (Chair of Committee)	Thomas Lalk (Member)
Dante DeBlassie (Member)	Dennis O'Neal (Department Head)

May 2004

Major Subject: Mechanical Engineering

ABSTRACT

Design and Analysis of a Composite Flywheel Preload Loss Test Rig. (May 2004)

Jason Lee Preuss, B.S., Texas A&M University

Chair of Advisory Committee: Dr. Alan Palazzolo

Flywheel energy storage units have become a viable alternative to electrochemical batteries in applications such as satellites, uninterrupted power supplies, and hybrid vehicles. However, this performance is contingent upon safe operation since these flywheels can release their stored energy almost instantaneously upon failure. The research presented here investigates a health monitoring technology that may give an early indication of degraded material properties in a concentric ring composite flywheel. The existence of degraded material properties is manifested as a change in mass eccentricity due to asymmetric growth of the outermost flywheel ring. A test rig concept to investigate the technology is developed in detail using a systems engineering design process. Successful detection of the change in mass eccentricity was verified analytically through dynamic modeling of the flywheel rotor and magnetic suspension system. During steady state operation detection was determined to be feasible via measurements of the magnetic bearing currents and shaft position provided by the magnetic suspension feedback sensors. A rotordynamic analysis was also conducted and predicts successful operation to the maximum operating speed of 50,000 Rpm.

DEDICATION

To all those who helped along the way, especially my parents and Esther Etzel.

ACKNOWLEDGMENTS

First and foremost, I would like to thank Dr. Alan Palazzolo for his guidance, technical expertise, and patience during the course of my research. I would also like to thank Dr. Thomas Lalk and Dr. Dante DeBlassie for serving on my advisory committee.

I would like to acknowledge Ray Beach, Ralph Jansen, Albert Kascak, Kerry McLallin, and Andy Provenza of NASA Glenn for their efforts in obtaining funding and technical monitoring of this research.

A special thanks to Polina Bondarchuk for her support, encouragement, and assistance in the presentation of the research presented here.

Last, but certainly not least, I would like to thank the personnel of the Vibration Control and Electromechanics Laboratory, especially Dr. Yeonkyu Kim and Dr. Andrew Kenny for their support and technical assistance during the course of this investigation.

TABLE OF CONTENTS

CHAPTER Page

LIST OF FIGURES

FIGURE Page

LIST OF TABLES

CHAPTER I

INTRODUCTION

1.1 Overview

Modern technology has enabled a new application for the age old flywheel in advanced flywheel energy storage systems. Flywheel energy storage systems store kinetic energy in the form of a rotating flywheel typically made of composite materials. These systems are often called mechanical batteries since electrical energy is input, stored as rotational mechanical energy, and converted back to electrical energy to provide power on demand. The basic components of a typical system include a composite flywheel, vacuum and safety containment, magnetic bearings, motor / generator, and electronics for control and power conversion. Advances in magnetic bearings, power electronics, and composites have allowed flywheel energy storage systems to surpass electrochemical batteries in terms of achievable energy density, power density, and number of discharge cycles. This is crucial in space applications where weight and longevity is of great concern. Significant research has been performed to optimize and demonstrate the technology can work. However, when failure occurs in these flywheels the energy is released almost instantaneously and can be catastrophic. Containment and health monitoring has now become a significant issue as these energy storage units are being incorporated into other systems where a failure must be avoided, or at a minimum contained (Space station, hybrid vehicles, etc). The complete containment of a composite flywheel burst requires a heavy structure and eliminates any advantage of the flywheel unit in terms of energy density. Real time heath monitoring is a viable alternative that may allow reduction of the containment requirements.

NASA Glenn Research Center (NASA-GRC) expressed a need for a means to monitor the health of a composite flywheel constructed of concentric preloaded composite rings. In response, the University of Texas Center for Electromagnetics (UT-CEM) designed a flywheel that exhibits a change in mass eccentricity when fatigue,

---

This thesis follows the style and format of the *Journal of Sound and Vibration*.

thermal expansion, or other phenomena cause a loss in preload of the outer ring. The design is such that the outer ring of the flywheel is only bonded to next inner ring on 180 degrees of the contact area. As a result, centripetal acceleration causes the outer ring to grow asymmetrically if the preload is lost. The existence of preload or compression between the rings is important since it provides the structural integrity of the flywheel. The outer ring preload is designed to be maintained to just above maximum operating speed. Therefore, the asymmetric growth would only be sensed in the operating speed range if the preload was reduced. The most notable factor that would cause a reduction in the preload is fatigue. Fatigue in the composite material causes a reduction in the ring hoop stiffness which in turn reduces the preload.

Texas A&M Vibration and Controls laboratory has been sponsored by NASA-GRC to utilize a magnetic suspension system to develop health monitoring techniques utilizing the UT-CEM Preload Loss Monitor technology. The research to be presented here focuses on the design of a test rig utilizing a magnetic suspension to demonstrate the UT-CEM technology and a means to detect the mass unbalance it generates. Indication of eccentric deformation is typically determined using an optical sensor to measure the deflection of the outermost cylinder while the flywheel is spinning. NASA-GRC has expressed a desire to utilize the installed magnetic suspension for the same purposes if possible. The latter approach does not require an optical sensor as well as any associated electronics and may yield more accurate indication of eccentric deformation. This results from the magnetic suspension sensors measuring motion at a much smaller radius than the optical sensors and therefore being less susceptible to shaft runout. At the present, this approach to flywheel health monitoring using the UT-CEM Preload Loss Monitor technology and a magnetic suspension is unique. However, there has been research in composite flywheel health monitoring that provides useful insights and can help clarify the novel contributions of the work presented here.

1.2 Literature Review

Research regarding the health monitoring of composite flywheels is just beginning as energy storage units are beginning to be incorporated into practical applications. Most of

the research conducted so far has focused on predicting and detecting the severity of flaws in the flywheel during operation.

Fisher and Lesieutre [1] propose health monitoring by detecting small changes in the balance state due to various types of flaws that can occur in composite flywheels. An experimental apparatus was constructed consisting of a rotor supported by ball bearings and attached to the housing via an array of springs to provide a low stiffness. Initially, benchtop experiments are conducted to characterize the unbalance response to each type of flaw. The flaws are simulated using tape and small masses that are released from the flywheel at speeds up to 10,000 Rpm. The resulting changes in unbalance are detected using position sensors that monitor the rotor hub and rim. Based on the data collected a controller was also developed to evaluate the severity of flaws and de-rate the maximum flywheel operating speed accordingly. Successful detection and operation of the controller was reported for changes in mass eccentricity as small as 10 microns.

Shiue, Lesieutre, and Bakis [2] propose a similar health monitoring scheme in which the balance state is monitored for changes due to small flaws in the flywheel. The influence coefficient method typically used for balancing rotors is employed to describe the balance state. This method essentially relies on an assumption of a linear relationship, described by the influence coefficients, between the rotor vibration measurement and rotor unbalance. The authors propose the use of normalized or speed independent influence coefficients since the flaws are elastic. The relationship between flaw sizes and level of unbalance are derived from a finite element analysis. Test rigs were constructed and small brass pieces used to simulate the predicted levels of unbalance and determine if they could be detected. Mass eccentricity changes as small as 80 microns were successfully detected. Further research by the authors includes the use of fracture mechanics to determine the growth rate and severity of flaws [3].

The research presented here is differentiated from prior research by the mechanism that generates the unbalance. In this case, the UT-CEM flywheel generates an unbalance due to degraded material properties that could lead to the flaws described above in prior research.

1.3 Objectives and Novel Contributions

The objectives of this research are as follows:

- Design a test rig concept that could be used to determine if a magnetic suspension system can be monitored for detection of a UT-CEM predicted change in mass eccentricity of the PLM composite flywheel.
- Verify that detection of the mass eccentricity is feasible through numerical simulation of the magnetic suspension controller and rigid body dynamics.
- Verify through rotordynamic analysis that the rig concept can operate reliably over the desired operating speed range (0-50,000 rpm).

The first objective is addressed in chapter II and will be accomplished using a top-down systems engineering design process in conjunction with technical analysis. In this process conceptual designs are generated based on the need definition and functions required of the test rig. Significant parameters are then identified to aid in identification of the best design concept. The final design is presented in detail including a complete set of fabrication drawings.

The second objective is covered in chapter III and accomplished via an analytical investigation due to limitations on the procurement of the test rig. The magnetic suspension system and rigid body dynamics of the rotor are modeled using a state space representation. Steady state response is investigated such that the detection concept is verified by observing differences in steady state response when the PLM flywheel change in mass eccentricity, residual unbalance, and shaft runout are included in the model.

In chapter IV a critical speed analysis is conducted to aid in satisfying the last objective. This analysis ensures that rotor critical speeds are sufficiently removed from the operating speed range of 20,000 to 50,000 Rpm. Rigid body modes are identified using the state space equations developed in chapter III while rotor bending modes are derived using a transfer matrix analysis.

The novel contributions of this thesis include:

- Design of a test rig concept that will allow verification of a newly developed composite flywheel health monitoring technique.
- Development of a health monitoring scheme for the PLM composite flywheel utilizing measurements of rotor displacement and currents associated with a magnetic suspension.

These contributions are unique in that there is little research regarding health monitoring of composite flywheels. In addition, the research that has been done is focused on detecting changes in unbalance caused by flaws such as cracks and delaminations that arise during operation due to degradation of the composite material. In contrast, the PLM flywheel technology incorporates a unique mechanism to create a change in unbalance when a reduction in the composite material properties occurs. Hence, there is potential for earlier and more reliable detection of impending failure. The research here will aid in the development of this unique flywheel technology.

CHAPTER II

PLM FLYWHEEL TEST RIG DESIGN

2.1 Design Process

Increasing complexity of modern systems has created the need for a well defined design process. One such design process is referred to as the systems engineering design process and is used here to present the final design solution in an organized and logical manner. Some of the main characteristics of the process include a top down approach and an emphasis on defining functional requirements [4]. The top-down approach develops a logical decision path beginning with the most basic need and ending with the "nuts and bolts". The general outline of the process is depicted below in figure 2.1.

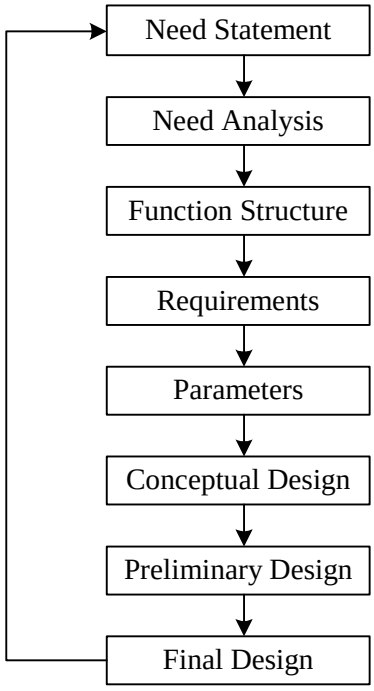

Figure 2.1: Systems Engineering Design Process

The first step in the design process is to develop a need statement, which identifies the most basic requirements the design must satisfy to be successful. The need statement is more specific than a problem statement since it often implies a solution approach. However, it should only state what will be satisfied by an approach without regard as to how it may be accomplished. In this manner, the need statement does not limit the design solution possibilities.

The need analysis is the next level of specificity in the process where the designer expands on the meaning of the need statement and identifies the top level functions the system must provide. Typical aspects of the need analysis include interpretation of the need statement, background information, and clarification of terms or concepts. The designer may also clarify any major constraints or assumptions implied or imposed by the need statement.

The function structure analysis provides a means to identify and organize the functions the design must fulfill in a hierarchical manner. Each function is characterized as a single entry and exit point, implements a single independent function, and is separately verifiable. The designer begins with the most basic functions the design must provide and continues to decompose the functions until specific functional requirements are reached. In essence, the process ends when further functional decomposition would require the designer to identify how a function would be fulfilled.

The need, need analysis, and functional analysis provide a decomposition and understanding of the design problem such that the designer can identify requirements of the system. There are two types of requirements: functional and performance. The functional requirements are taken directly from the lowest levels of the function structure and each one has specific performance requirements associated with it. Performance requirements describe how well a functional requirement must be performed and can be calculated, related to constraints, assumed, or derived from the background information.

At this point in the process, the designer has established what the design must do and is ready to generate conceptual design solutions. This creative process is aided by the identification of design parameters which can be anything that affects the design and the designer has control over. Typical examples for an energy storage system would be

energy density or power density. In any case, the parameters the designer chooses as the most important provide the basis for development of a conceptual design. The dominant parameters can then be optimized or compared to determine the best configuration of a concept. The identification of new concepts is then facilitated by defining new parameters or placing a different emphasis on previous parameters.

Ultimately, the designer must select a conceptual design to pursue further in the preliminary and final design stages. There may be several concepts based on or optimized with respect to different parameters. At a minimum, each design concept must meet the functional and performance requirements. Beyond this requirement the use of criteria provides one means of selecting a concept. Design criteria are simply desired aspects that may make one concept appear more attractive when compared to others. Once a concept is chosen, the designer moves on to the preliminary and final design stages where the level of detail is increased. It is important to note that the overall process depicted in figure 2.1 is iterated throughout the design process. It represents a top-down approach characterized by a progression from the general to specific aspects of the design.

2.2 Need Statement

Two need statements are presented below in order to clarify the relationship between the overall need concerning composite flywheel safety and the more specific need to be fulfilled by the design presented here. First, the overall need is stated below.

There is a need for structural health monitoring of flywheels constructed of preloaded concentric composite rings.

Development of technology in response to the above need gave rise to the specific need addressed in the design presented here and is stated below.

There is a need for a test rig that can be used to safely determine if a magnetic suspension system can be utilized to detect a predicted change in mass eccentricity of a UT-CEM designed composite flywheel.

This statement will be expanded upon in the need analysis.

2.3 Need Analysis

The overall need statement above originated from a desire by NASA-GRC to develop safer kinetic energy storage systems. These systems typically rely on composite flywheels with preloaded rings as the primary kinetic energy storage element. As explained in chapter I, UT-CEM developed a composite flywheel that generates a change in mass eccentricity when the material becomes degraded and structural integrity due to preload of the rings is reduced. In response, NASA-GRC has awarded Texas A&M VCEL funding to build a test rig to investigate the UT-CEM flywheel technology. UT-CEM has specially designed a flywheel for the VCEL such that the preload loss event first occurs at approximately 20,000 rpm. In addition, stress levels allow for safe operation to 50,000 rpm. As a result, several magnitudes of eccentricity can be investigated to determine the minimum eccentricity necessary for detection. Also, this provides some margin for error as predictions for the start of preload loss have no experimental basis. Detection in this case is simply being able to distinguish the effects of the mass eccentricity change from noise, shaft runout, and residual vibration.

Several major constraints are implied or arise from the background information stated above. First, operation to the maximum rated speed of 50,000 rpm is necessary to ensure all possible magnitudes of eccentricity are fully explored. Another major constraint is the physical size and characteristics of the flywheel. The composite flywheel itself is 7.35 inches in diameter, 3 inches in length, and has an inner diameter of 3.5 inches. UT-CEM designed the flywheel to be pressed onto a 3.5 inch diameter metal rim. The material and means by which the rim is interfaced with other components of the system is not constrained. These speeds and size of the flywheel combined with the inclusion of safe operation in the need statement implies two additional major constraints. First, there must be containment for the worst case scenario corresponding to a complete flywheel burst releasing all energy nearly instantaneously. The approximate kinetic energy to be contained is governed by the density, rotational velocity, and size of the flywheel. At 50,000 rpm the corresponding energy stored is 300 W-hr. In addition to containing the kinetic energy released it is important to note that when composite flywheels burst a large amount of epoxy dust is generated that can react with air to create an explosive release of

energy. An incident of this nature has been documented by researchers in the field [5]. Therefore, a vacuum or non-oxygen atmosphere is also a major constraint on the operating environment.

With the above background and major constraints in mind we can begin to decompose the need into major functions to be fulfilled. In this case, there are three top level functions derived directly from the need. First, a magnetic suspension of the flywheel must be provided. The major constraints concerning rotation speed, size, and mass of the flywheel will be important for this function. The second major function is to provide mechanical energy. Ultimately, the mechanical energy will be manifested as rotational velocity of the flywheel. Lastly, an appropriate operating environment must be provided. This function will lead to sub-functions that must address the major constraints discussed previously regarding safety and energy containment.

2.4 Function Structure

The three top level functions discussed previously must be decomposed into subfunctions until specific requirements can stated. Figure 2.2 depicts the function structure for the preload loss monitor test rig. The function structure provides a method to organize the functional decomposition of the need. The most basic functional requirements include providing mechanical energy to spin the flywheel, a magnetic suspension system, and the proper operating environment. These basic functions are decomposed until it becomes necessary to define how a particular function will be fulfilled.

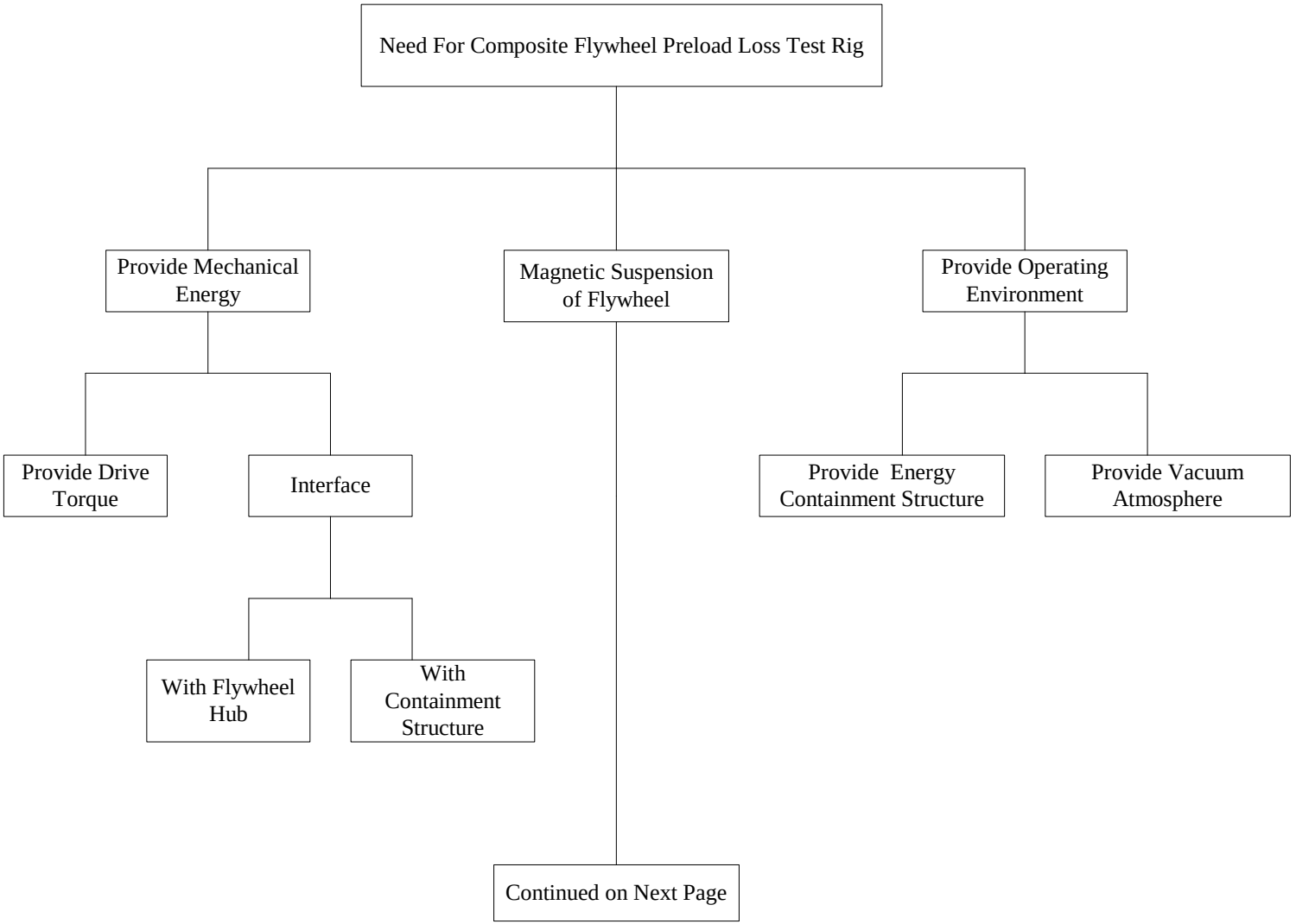

Figure 2.2: Function Structure

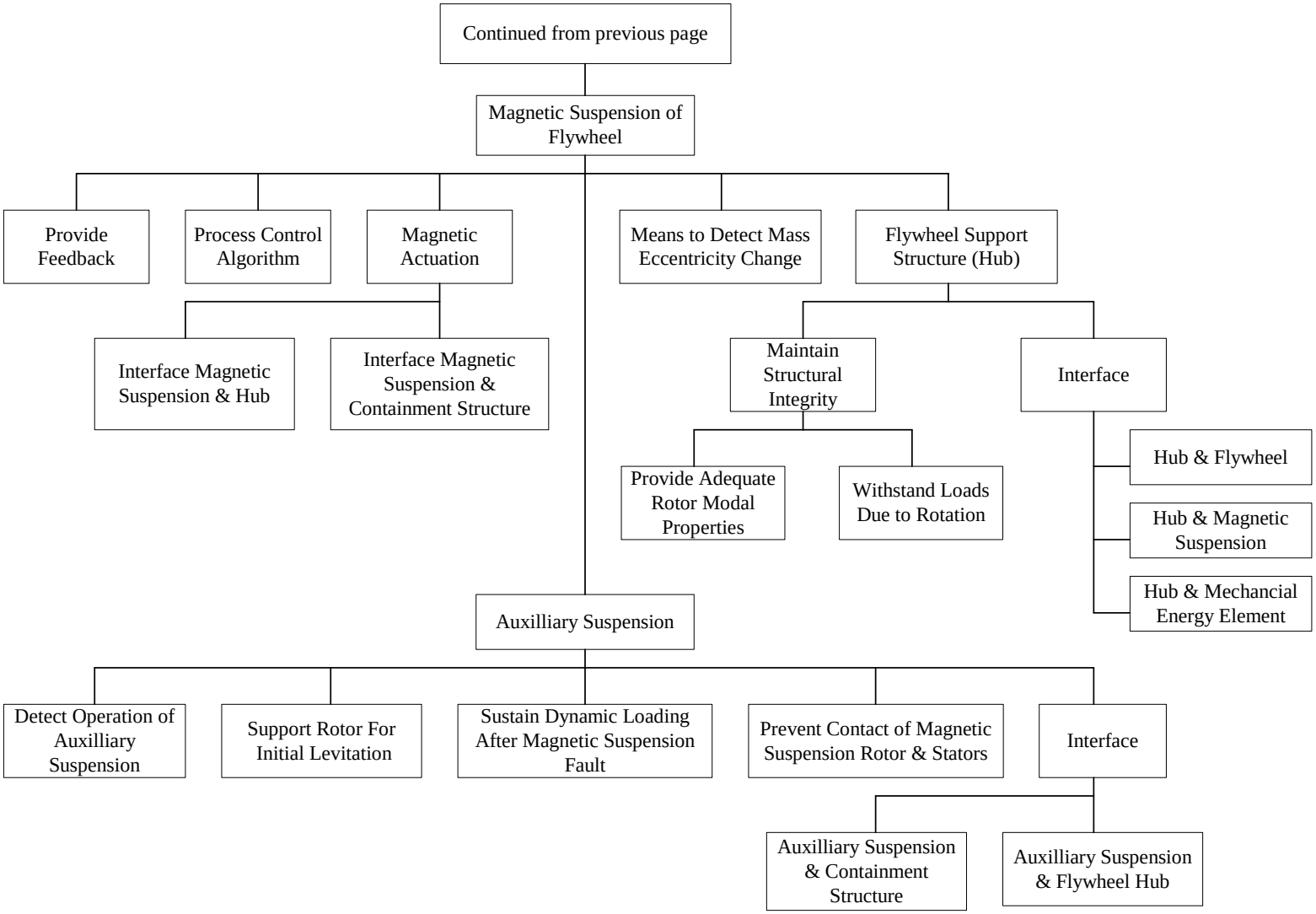

Figure 2.2 (Continued): Function Structure

2.5 Performance Requirements

The functional requirements of the PLM test rig are taken directly from the lowest levels of the function structure. Table 2.1 summarizes the specific performance requirements associated with each functional requirement. Also, the source for each performance requirement is listed. Each of these requirements must be met by any of the design solutions.

2.6 Parameters & Constraints

There are several significant parameters that will likely determine the success of the design. The first parameter is the rotor mass. This is important since the mass eccentricity generated by the PLM flywheel is applied to the entire mass of the rotor. Therefore, additional rotor mass serves only to reduce the complete rotor eccentricity whose detection is of primary interest during testing.

The second important parameter to consider is related to the interface between the mechanical energy element and the flywheel hub. The dynamic contributions at this interface must be minimal to ensure it does not influence the rotor response due to the change in mass eccentricity generated by the PLM flywheel.

Finally, the rotor modal or vibration properties are very important to the success of the design. Rotor bending modes are difficult to damp especially with magnetic bearings. Contributions from these types of modes in the operating speed range could make it difficult to distinguish between the response due the change in mass eccentricity and that which is contributed by the bending mode. Ultimately, these modes could also prevent operation to the required maximum operating speed.

The major constraint in this design effort is that the flywheel was designed and constructed prior to the test rig design process. In addition, funding considerations require the use of existing components whenever possible. Therefore, matching sizing requirements becomes difficult.

Table 2.1: Functional and Performance Requirements for PLM Test Rig

Functional Requirements	Performance Requirements	Source
1. Provide drive torque	Provide torque greater than 20 oz.-in @ 0-50000 Rpm	Calculated
2. Provide feedback	Non-contact measurement of shaft position with output gain > 100 V/in.	VCEL
3. Process control algorithm	Cutoff Frequency > 2000 Hz	VCEL
4. Magnetic actuation	Radial load capacity per axis shall be greater than 40 lb @ 1500 Hz and axial load capacity greater than 40 lb @ 0 Hz	VCEL
5. Interface hub & flywheel	Support flywheel press fit on 3.5 in. diameter X 3 in. length.	UT-CEM
6. Provide adequate rotor modal properties	Rotor bending modes to be greater than 120% of maximum operating speed (50,000 Rpm)	UT-CEM
7. Withstand rotating dynamic loads	Withstand stress due to 50,000 rpm rotation.	UT-CEM
8. Detect operation of auxiliary suspension	Electrical signal with peak to peak voltage greater than 50 mV.	VCEL
9. Support rotor for initial levitation	Keep magnetic suspension gap < .030”	VCEL
10. Sustain loading after magnetic suspension fault	Withstand loading of rotor whirling @ speeds up to 30,000 Rpm.	UT-CEM
11. Prevent contact of magnetic suspension rotor & stators	Constrain rotor motion to less than magnetic suspension air gap of .020”	VCEL
12. Provide energy containment	Withstand 300 W-hr flywheel burst	Calculated
13. Provide vacuum atm.	Absolute Pressure < 10^{-2} Torr	VCEL

2.7 Conceptual Designs

The final design to be presented in the next section was picked from several design configurations developed during the design process. During the design process a desire was expressed to operate the test rig within a containment vessel already installed in the VCEL. The vessel comprises seals for vacuum and a 4 inch thick steel liner for containment to 5000 W-hr. The test area within the structure is approximately 3 feet in diameter and 4 feet in depth. The use of this vessel essentially fulfilled the functional requirement for an operating environment. However, interfacing with the vessel was still a significant function to fulfill. The energy for rotating the flywheel would have to be transferred into the vacuum environment thus requiring some form of sealing. Three mechanical energy elements were considered. First, an existing air turbine with a carbon face seal was considered. This concept was abandoned in lieu of electric motors that could be placed in the vacuum environment. The electric motors avoid the complexity of providing a vacuum seal around a shaft rotating to 50,000 Rpm.

Two conceptual designs based on using electric motors for the mechanical energy element were considered. Figure 2.3 depicts the first concept. The first concept involves the use of a “framed” motor in which the housing, bearings, and motor shaft are an integral unit. The flywheel is supported by a one piece rotor that is coupled to the motor via a splined coupling. Two magnetic bearings provide the radial and axial forces necessary to levitate the rotor. A high speed test rig at the VCEL was utilized to test the spline coupling and was found to operate very well to 53,000 Rpm. However, initial alignment was very difficult and the dynamic contributions the coupling would provide to the PLM rotor were uncertain.

The second concept involved the use of a “frameless” electric motor. This type of motor utilizes a one piece permanent magnet as the rotor. In this case, the permanent magnet would become an integral part of the PLM rotor. A completely levitated rotor results when this type of motor is combined with a magnetic suspension. This concept eventually was chosen as the concept to develop into a final design and is presented in the next section.

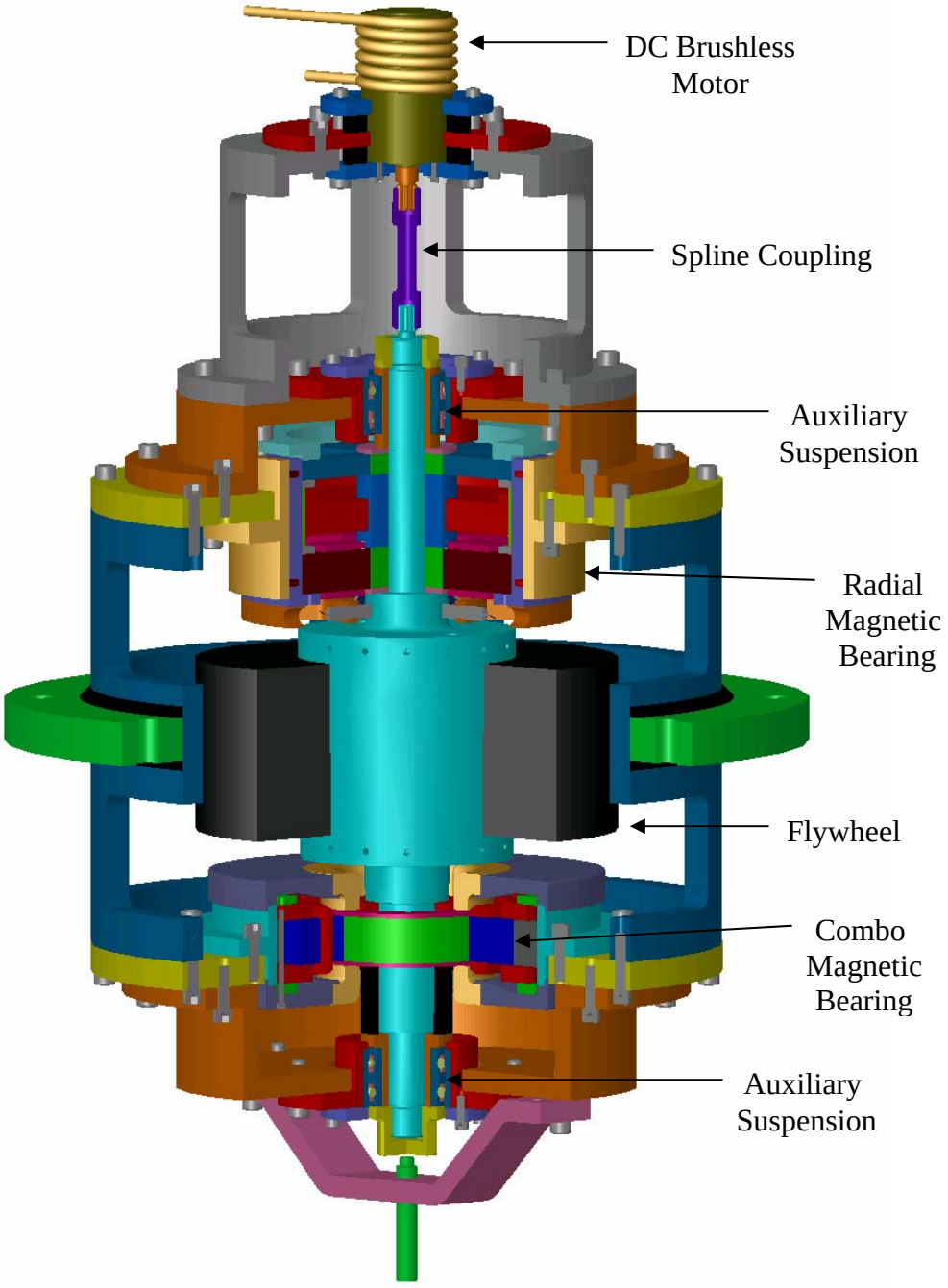

Figure 2.3: PLM Test Rig Conceptual Design 1

2.8 Final Design

The final design of the PLM test rig is depicted in figure 2.4. The test rig comprises a one piece rotor hub for the flywheel that is supported by two magnetic bearings and driven by a brushless DC motor. Angular contact ball bearings fulfill the functional requirement for an auxiliary bearing system that provides rotor support when the rotor is not levitated. A unique aspect regarding this concept is that the rotor does not physically contact any surfaces during operation. Torque and forces for levitation are provided via magnetic forces. A detailed description follows to describe the functions the sub-components fulfill.

Figure 2.5 depicts the rotating structure for the flywheel (Rotor). The rotor hub consists of a one piece titanium shaft that interfaces with the flywheel, magnetic bearings, auxiliary suspension, and motor. The titanium material was selected based on its lower density and strength to withstand rotational stresses. The lower density is important since additional rotor mass reduces the amount of rotor mass eccentricity created by the PLM flywheel. The rotor laminations provide a path for the magnetic flux of the bearings. Also, laminations are used to reduce eddy currents that arise from the time varying magnetic fields. In this case, the laminations are bonded together and assembled onto the rotor with Loctite 620 retaining compound. Replaceable sleeves are shrunk onto the rotor to provide a wear resistant interface with the auxiliary bearings since titanium has poor wear and sliding properties. 440C stainless steel was chosen as the material for the sleeves due to a low dynamic coefficient of friction and excellent wear properties. Finally, the one piece cylindrical motor magnet is assembled onto the rotor via epoxy as recommended by the motor manufacturer.

Figures 2.6 and 2.7 depict the magnetic bearings used to support the rotor during operation. These bearings were developed by the VCEL in conjunction with NASA-GRC for use in various test rigs. The “combo” bearing provides a radial load capacity of 75 lbs and an axial load capacity of 140 lbs. The radial magnetic bearing also provides 75 pounds of load capacity. The operation of the magnetic bearings, controller, amplifiers, and feedback sensors associated with the bearings are discussed in detail in chapter III.

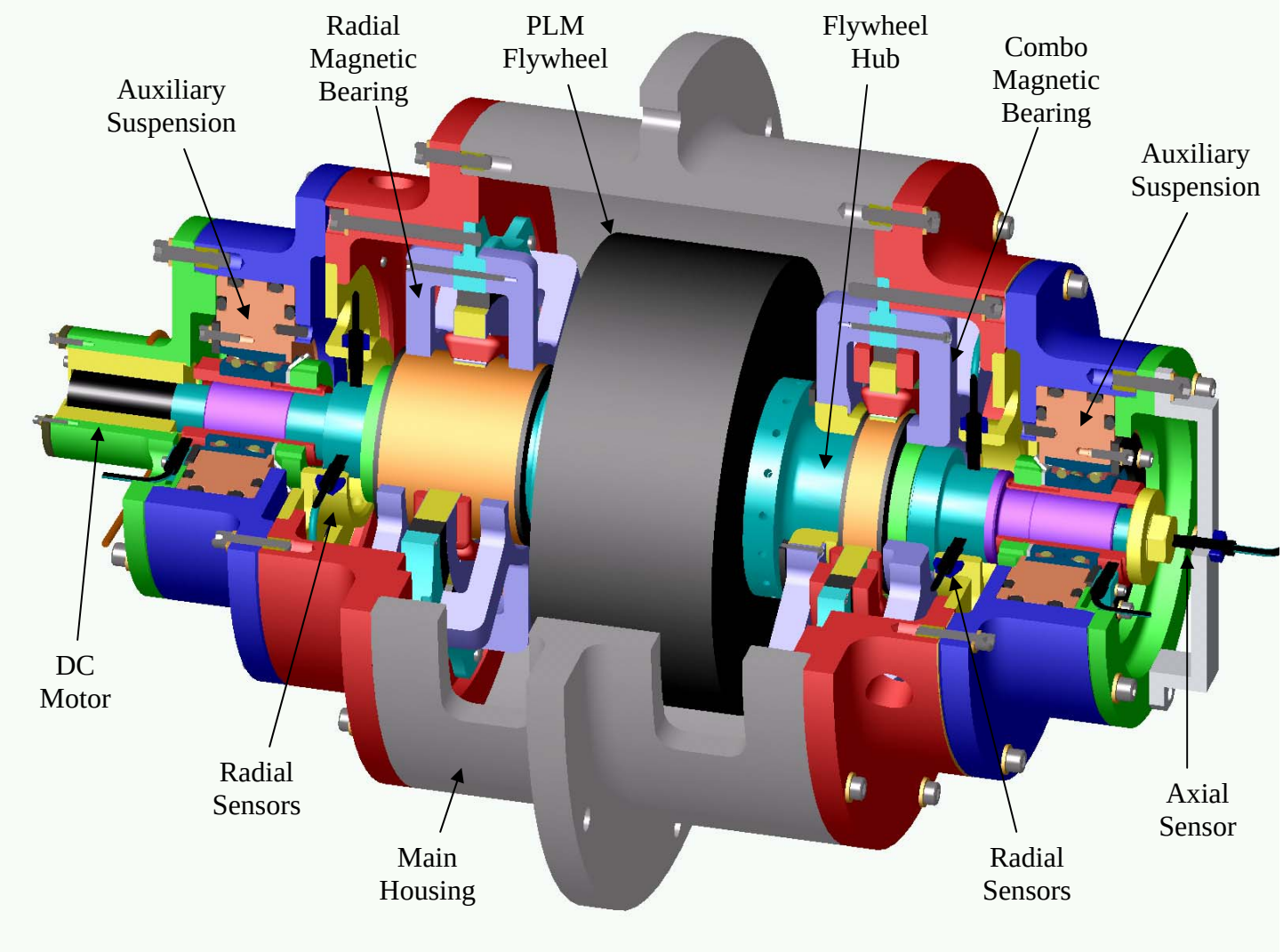

Figure 2.4: Assembly View of PLM Test Rig Final Design

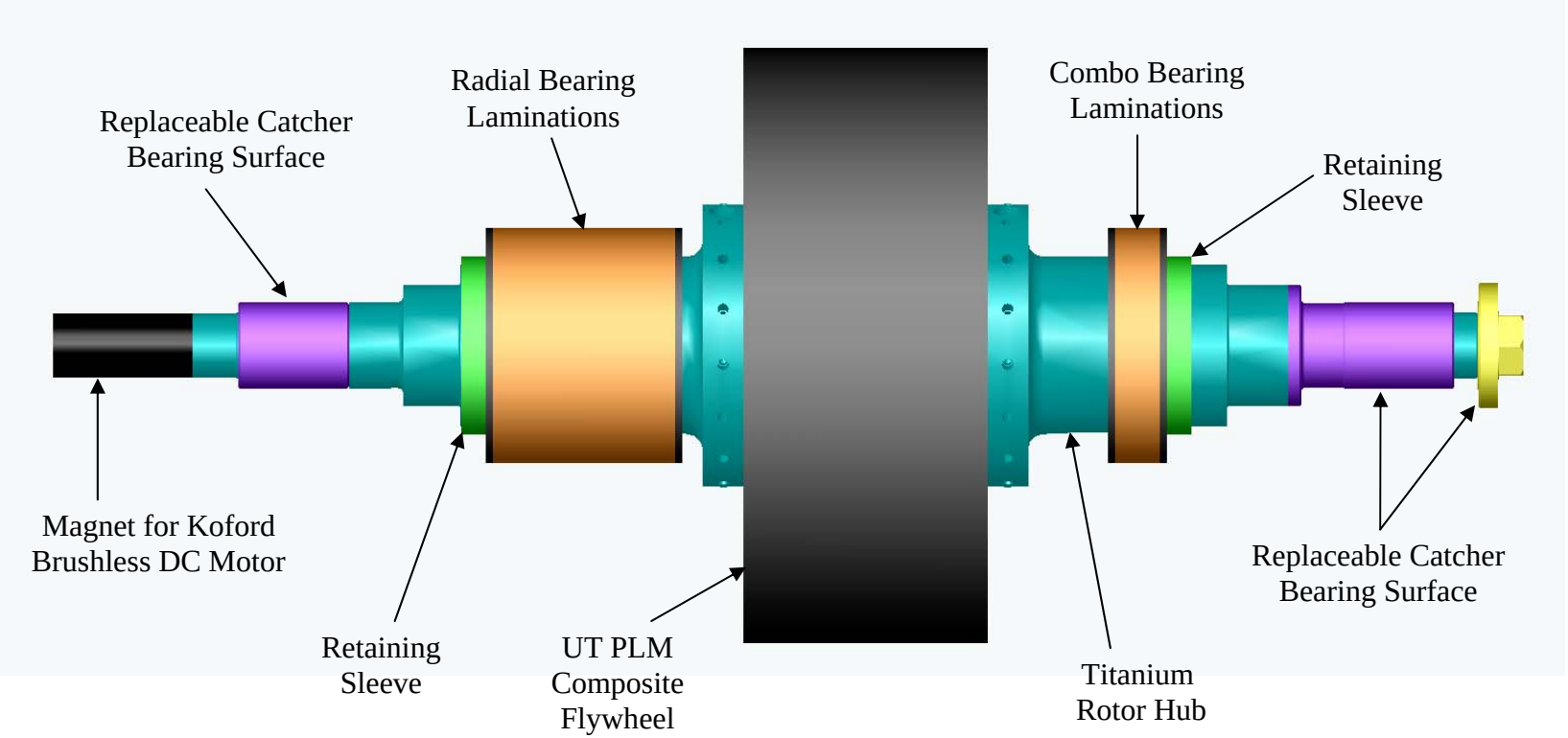

Figure 2.5: PLM Rotor Assembly

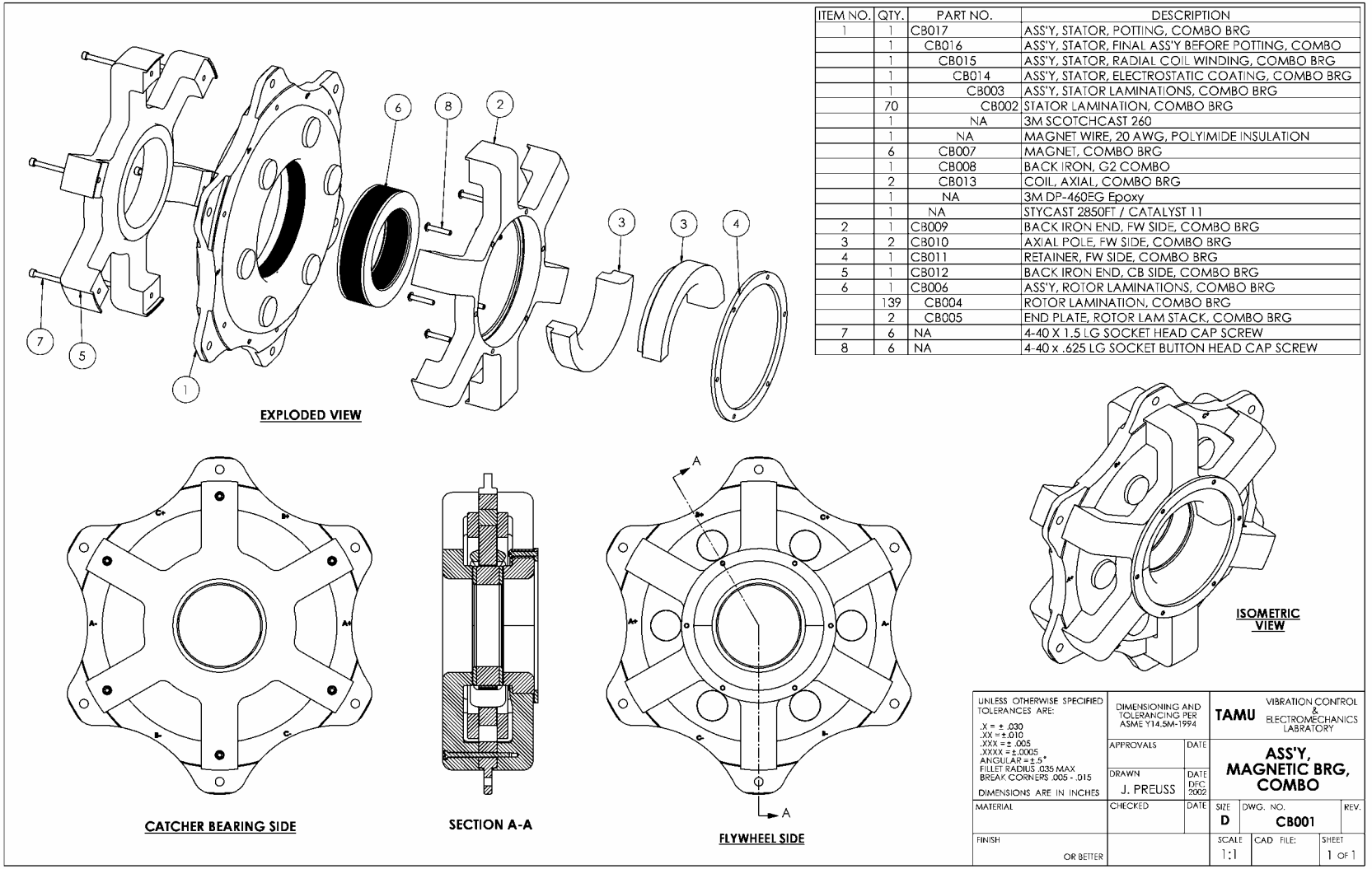

ITEM NO.	QTY.	PART NO.	DESCRIPTION
1	1	CB017	ASS'Y, STATOR, POTTING, COMBO BRG
	1	CB016	ASS'Y, STATOR, FINAL ASS'Y BEFORE POTTING, COMBO
	1	CB015	ASS'Y, STATOR, RADIAL COIL WINDING, COMBO BRG
	1	CB014	ASS'Y, STATOR, ELECTROSTATIC COATING, COMBO BRG
	1	CB003	ASS'Y, STATOR LAMINATIONS, COMBO BRG
	70	CB002	STATOR LAMINATION, COMBO BRG
	1	NA	3M SCOTCHCAST 260
	1	NA	MAGNET WIRE, 20 AWG, POLYIMIDE INSULATION
	6	CB007	MAGNET, COMBO BRG
	1	CB008	BACK IRON, G2 COMBO
	2	CB013	COIL, AXIAL, COMBO BRG
	1	NA	3M DP-460EG Epoxy
	1	NA	STYCAST 2850FT / CATALYST 11
2	1	CB009	BACK IRON END, FW SIDE, COMBO BRG
3	2	CB010	AXIAL POLE, FW SIDE, COMBO BRG
4	1	CB011	RETAINER, FW SIDE, COMBO BRG
5	1	CB012	BACK IRON END, CB SIDE, COMBO BRG
6	1	CB006	ASS'Y, ROTOR LAMINATIONS, COMBO BRG
	139	CB004	ROTOR LAMINATION, COMBO BRG
	2	CB005	END PLATE, ROTOR LAM STACK, COMBO BRG
7	6	NA	4-40 X 1.5 LG SOCKET HEAD CAP SCREW
8	6	NA	4-40 x .625 LG SOCKET BUTTON HEAD CAP SCREW

Figure 2.6: Combo Magnetic Bearing Assembly

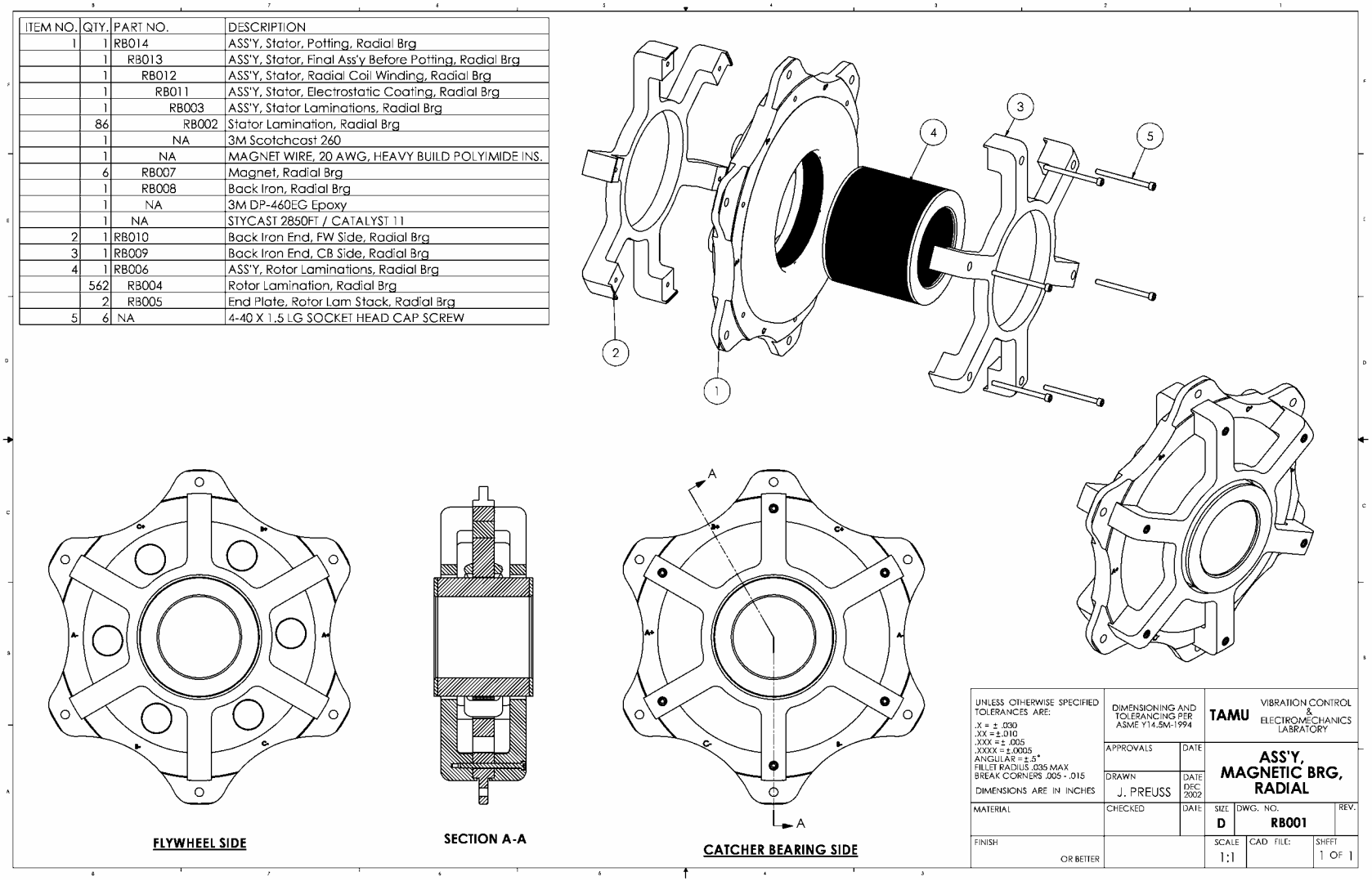

Figure 2.7: Radial Magnetic Bearing Assembly

Figures 2.8 and 2.9 depict the auxiliary bearing sub-system for the combination magnetic bearing end and radial magnetic bearing end. Both auxiliary bearing assemblies are identical with the exception of the motor assembly on the radial magnetic bearing end. The basic concept is to use ball bearings with sufficient clearance in the bore to allow levitation but prevent contact of the laminated magnetic bearing surfaces. In case the rotor falls during operation, the use of a ball bearing allows the inner race to spin and reduce the relative sliding motion between the rotor and stator surfaces. This is important to reduce wear and prevent the possibility of destructive backward whirl. In addition, the bearing housing is supported on o-rings since the ball bearings alone provide a low amount of damping. A related performance requirement was that the auxiliary bearing system would sustain loading after a magnetic bearing fault which might occur at the maximum operating speed. The specific type of bearings used are high speed greased angular contact bearings rated to 31,400 Rpm and a radial dynamic load capacity of 2,778 lbs. Research in this area suggests that the rotor whirls in the bearing clearance up to 30% of the initial rotor speed [6]. With this in mind, the bearings in the PLM test rig would see a radial loading of 563 lbs based on a clearance of .009 inches, a whirl speed of 15,000 Rpm, and total rotor mass of 19.6 lbs. The bearings are expected to sustain these loads based on the bearing ratings and short duration of the loading. A replaceable wear ring constructed of the bearing steel is incorporated in the bearing bore to mitigate premature wear.

In order to spin the rotor assembly a brushless DC motor is used. The motor is manufactured by Koford and is rated to provide 55 oz-in. of torque at 51,000 Rpm (1684 W) which satisfies the performance requirements very well. The motor consists of a stator with hall sensors to detect rotor position and a rotor that is a one piece cylindrical magnet designed to become integral with a customer supplied rotor. A PWM type driver is used to supply current to the motor while hermetically sealed electrical connectors will be used to transfer the electrical energy into the vacuum environment. Figure 2.9 depicts the motor assembly which occurs at the end of the auxiliary bearing assembly.

Finally, the magnetic bearings, auxiliary bearings, and motor are interfaced with the containment structure via an aluminum housing. Aluminum material was chosen for ease

of manufacturing and to promote thermal conduction between the containment structure and components. A bolt circle on the containment structure will receive the flange on the main housing depicted in figure 2.4.

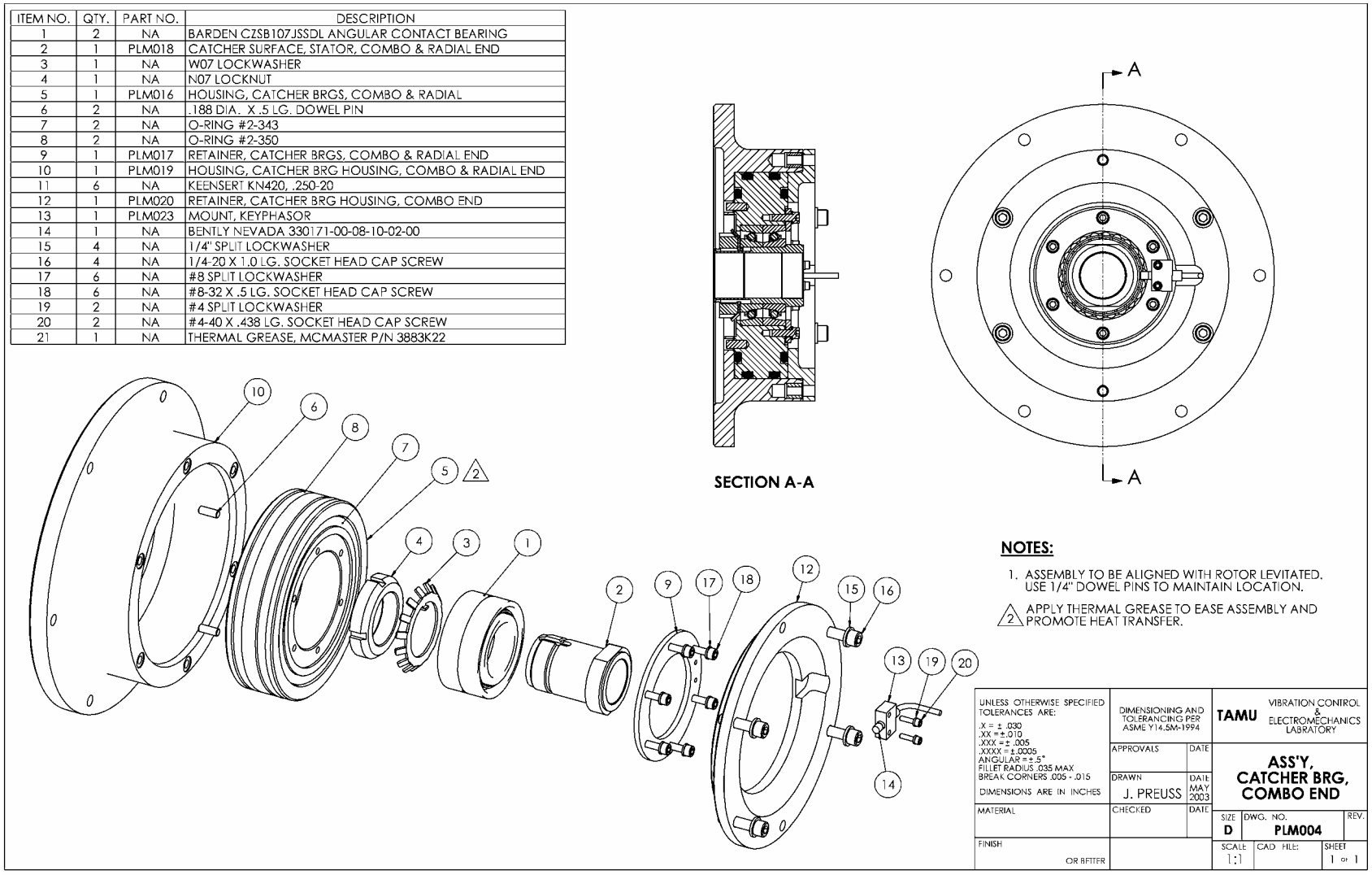

Figure 2.8: Catcher Bearing Assembly for Combo Magnetic Bearing

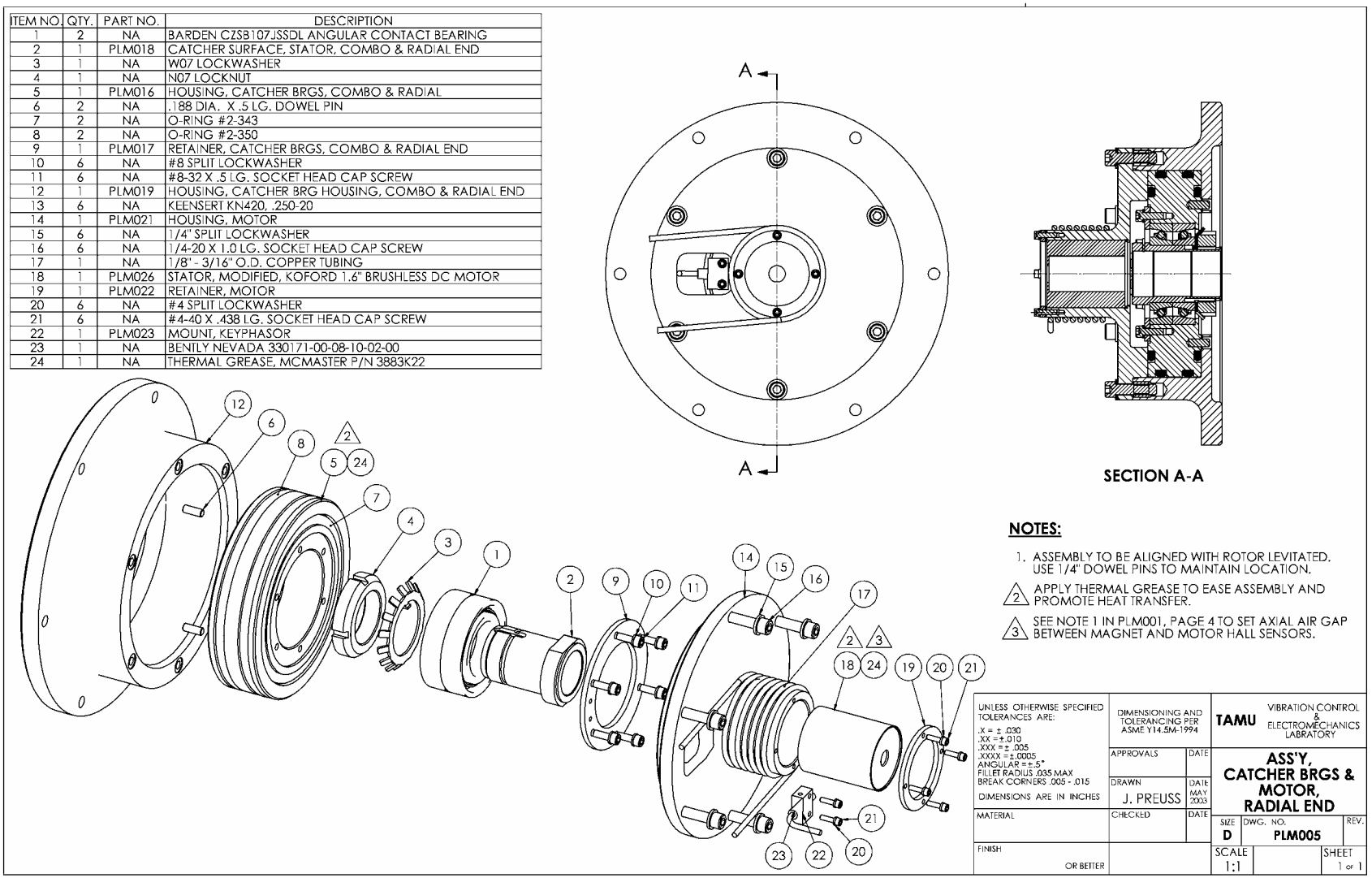

Figure 2.9: Catcher Bearing Assembly For Radial Magnetic Bearing

CHAPTER III

DYNAMIC SIMULATION OF ROTOR-BEARING SYSTEM

A numerical simulation of the rotor-bearing system is conducted to investigate steady state response. In this manner, the detection of the flywheel mass eccentricity is determined to be feasible. A system model of the overall rotor-bearing system is presented followed by a detailed derivation of each component model. Residual unbalance, change in mass eccentricity due to the preload loss event, the use of notch filters, and position sensor runout error are the primary parameters investigated and presented in the results.

3.1 System Model

The rotor-bearing system model depicted in figure 3.1 is comprised of a rigid rotor supported by two magnetic bearings, a magnetic bearing controller, power amplifiers to drive currents in the bearing coils, and feedback sensors. The rigid rotor assumption will be addressed in chapter 4. Both magnetic bearings provide two radial axes along which forces can be applied to the rotor. In addition, the combination bearing incorporates a thrust axis whose contribution is negligible for the radial response investigated here. Each axis of the bearings is associated with controller PD gains, notch filters, a power amplifier, and a shaft position sensor. In order to model the system, first order differential equations are used to describe the dynamic behavior of each component. These equations are derived in the following sections and assembled into a standard form known as state space. The state space representation is given by the equations:

$$\{\dot{X}\} = [A]\{X\} + [B]\{U\} \tag{3.1}$$

$$\{Y\} = [C]\{X\} + [D]\{U\} \tag{3.2}$$

where {X} is a vector of n states used to describe the system behavior, {U} contains the system inputs, {Y} is a vector of the outputs, and [A], [B], [C], and [D] are coefficient matrices. Solution of the system state space equations will be carried out with a numerical solver for ordinary differential equations with initial conditions.

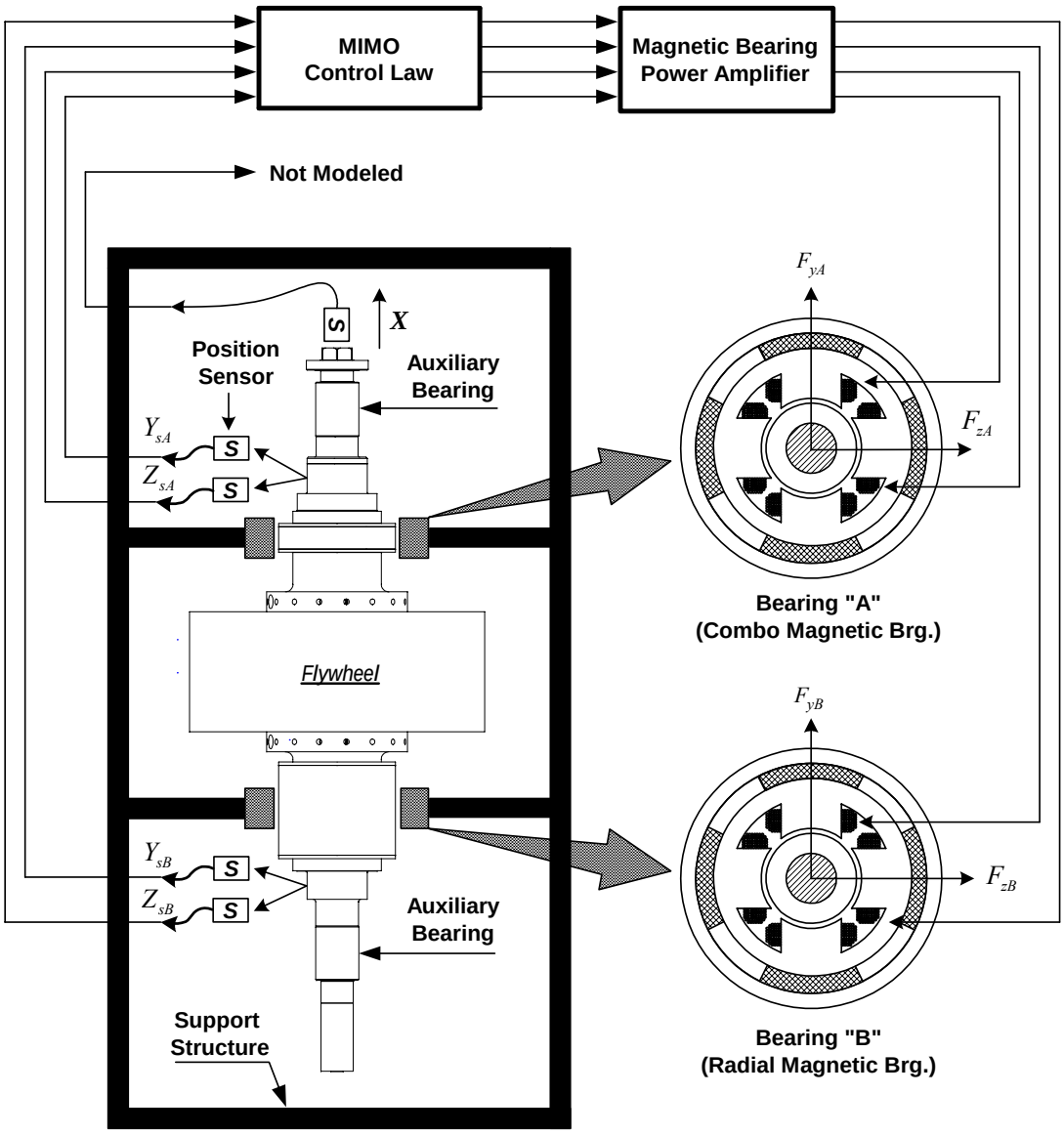

Figure 3.1: Rotor-Bearing System Model

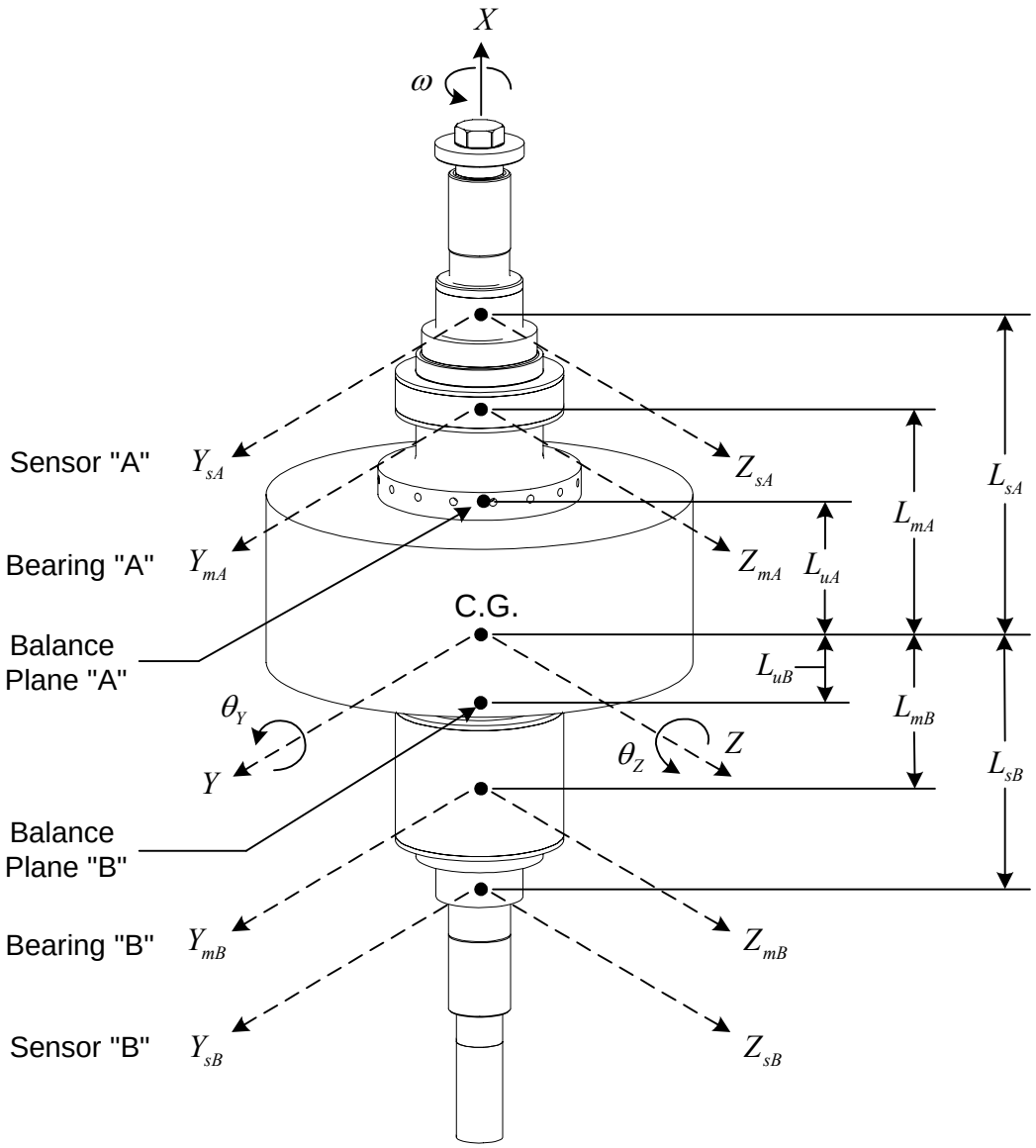

Figure 3.2: Rotor Geometry

3.2 Position Sensor Model

Non-contacting eddy current type sensors are used to measure shaft position. This is an essential measurement since it provides the only feedback used by the controller algorithm. Four sensors are utilized to determine shaft radial position as depicted in figure 3.1. Consider the *Y* axis sensor located next to bearing "A". The sensor is modeled as a first order filter whose input is rotor position at the sensor location, X_{syA}, and output is a corresponding voltage, V_{syA}. Hence, the sensor transfer function is written as:

$$G_{ysA} = \frac{V_{ysA}}{X_{ysA}} = \frac{\zeta_s}{\tau_s s + 1} \tag{3.3}$$

where

$$\tau_s = \frac{1}{2\pi f_s} \tag{3.4}$$

This definition is extended to all four sensors where a cutoff frequency, f_s, and sensitivity, ζ_s, of 3000 Hz and 200 V/in respectively are used based on published sensor data. For the analysis presented here a simulated rotor position measurement is obtained by a coordinate transformation from the rotor c.g. to the sensor locations such that:

$$\begin{Bmatrix} X_{ysA} \\ X_{ysB} \\ X_{zsA} \\ X_{zsB} \end{Bmatrix} = \begin{bmatrix} 1 & 0 & 0 & L_{sA} \\ 1 & 0 & 0 & -L_{sB} \\ 0 & 1 & -L_{sA} & 0 \\ 0 & 1 & L_{sB} & 0 \end{bmatrix} \begin{Bmatrix} Y \\ Z \\ \theta_y \\ \theta_z \end{Bmatrix} \tag{3.5}$$

or more compactly:

$$\{X_s\} = \left[T_{cg/s}\right]\{X_{cg}\} \tag{3.6}$$

Eddy current type sensors measure the position of the rotor surface and therefore are prone to incorporate shaft runout error. For a more realistic model, shaft runout is included and modeled as follows:

$$\{X_{runout}\} = \begin{Bmatrix} r_A \cos(\omega t + \phi_{rA}) \\ r_B \cos(\omega t + \phi_{rB}) \\ r_A \cos(\omega t + \phi_{rA} - \pi/2) \\ r_B \cos(\omega t + \phi_{rB} - \pi/2) \end{Bmatrix} \tag{3.7}$$

were r is the runout magnitude at each location, ω is the shaft angular velocity, and ϕ is the phase of the runout. With this in mind, the measured shaft position is redefined as:

$$\{X_{s+runout}\} = [T_{cg/s}]\{X_{cg}\} + \{X_{runout}\} \tag{3.8}$$

Using equations (3.3), (3.4), (3.8), and introducing the sensor state vector, $\{Q_s\}$, the state space form for the sensor system can be written as:

$$\{\dot{Q}_s\} = [A_s]\{Q_s\} + [B_s]\{X_{s+runout}\} \tag{3.9}$$

Using the identity matrix [I], the coefficient matrices can be written as:

$$[A_s] = (-1/\tau_s)[I]_{(4x4)} \tag{3.10}$$

$$[B_s] = [I]_{(4x4)} \tag{3.11}$$

The output voltages, $\{V_s\}$, are given by

$$\{V_s\} = \{V_{ysA} \quad V_{ysB} \quad V_{zsA} \quad V_{zsB}\}^T = [C_s]\{Q_s\} \tag{3.12}$$

where

$$[C_s] = (\zeta_s/\tau_s)[I]_{(4x4)} \tag{3.13}$$

These voltages will be used as the feedback input for the controller model.

3.3 Controller Model

A PD type control law is applied to each of the four rotor c.g. degrees of freedom. Using the *Y* axis as an example, figure 3.3 depicts the controller model consisting of proportional and derivative (PD) gains, low pass filter, notch filter, and lead compensation.

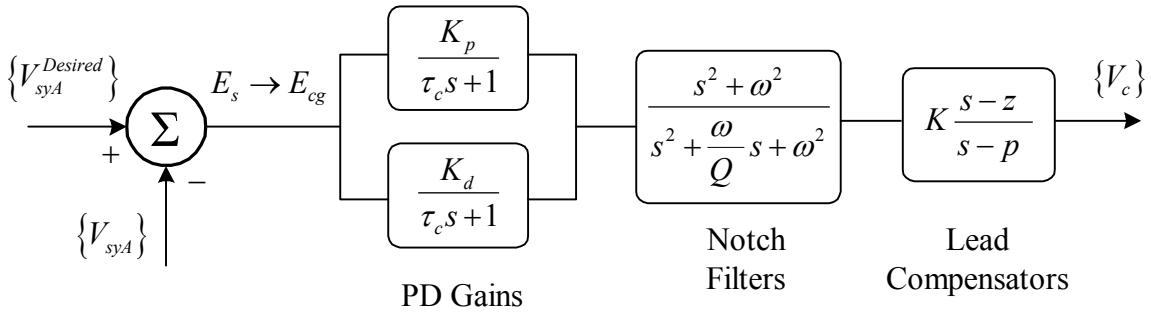

Figure 3.3: Controller Model

For simplicity, the desired value for the sensor voltages will be considered zero and corresponding to a perfectly centered rotor. Hence, all of the sensor output voltages, $\{V_s\}$, are equivalent to sensor error voltages, $\{E_s\}$. The controller algorithms are implemented based on errors in the c.g. position coordinates, $\{E_{cg}\}$. Therefore, the sensor voltages must be transformed to errors in the c.g. position as follows:

$$\left\{E_{cg}\right\} = \left\{E_y \quad E_{\theta y} \quad E_z \quad E_{\theta z}\right\}^T = \left[T_{s/cg}\right]\left\{V_s\right\} \tag{3.14}$$

where

$$T_s = \begin{bmatrix} \frac{L_{sB}}{\xi_s(L_{sA}+L_{sB})} & \frac{L_{sA}}{\xi_s(L_{sA}+L_{sB})} & 0 & 0 \\ 0 & 0 & \frac{-1}{L_{sA}\xi_s}+\frac{L_{sB}}{\xi_s L_{sA}(L_{sA}+L_{sB})} & \frac{1}{\xi_s(L_{sA}+L_{sB})} \\ 0 & 0 & \frac{L_{sB}}{\xi_s(L_{sA}+L_{sB})} & \frac{L_{sA}}{\xi_s(L_{sA}+L_{sB})} \\ \frac{1}{L_{sA}\xi_s}-\frac{L_{sB}}{\xi_s L_{sA}(L_{sA}+L_{sB})} & \frac{-1}{\xi_s(L_{sA}+L_{sB})} & 0 & 0 \end{bmatrix} \tag{3.15}$$

Continuing with the *Y* control axis as an example, the proportional gain stage is described by the transfer function:

$$G_p(s) = \frac{E_{yp}}{E_y} = \frac{K_p}{\tau_c s+1} \tag{3.16}$$

where τ_c is the controller time constant defined as:

$$\tau_c = \frac{1}{2\pi f_c} \tag{3.17}$$

Extending the definitions above to all of the contol axes and introducing the state variable, $\{Q_p\}$, the state space form for all of the proportional gain stages is written as:

$$\left\{\dot{Q}_p\right\} = \left[A_p\right]\left\{Q_p\right\} + \left\{E_{cg}\right\} \tag{3.18}$$

where

$$\left[A_p\right] = (-K_p/\tau_c)\left[I\right]_{(4x4)} \tag{3.19}$$

The resulting output gains, $\{E_{cgp}\}$, are:

$$\left\{E_{cgp}\right\} = \left\{E_{yp} \quad E_{\theta yp} \quad E_{zp} \quad E_{\theta zp}\right\}^T = \left[C_p\right]\left\{Q_p\right\} \tag{3.20}$$

where

$$\left[C_p\right] = (1/\tau_c)\left[I\right]_{(4x4)} \tag{3.21}$$

In a similar manner, the *Y* axis derivative gain stage is described by the transfer function:

$$\frac{E_{yd}}{E_y} = \frac{K_d s}{(\tau_c s + 1)^2} \tag{3.22}$$

The state space represention is as follows:

$$\left\{\dot{Q}_d\right\} = \left[A_d\right]\left\{Q_d\right\} + \left[B_d\right]\left\{E_{cg}\right\} \tag{3.23}$$

where

$$\left[A_d\right] = K_d \begin{bmatrix} \left[a_d\right] & 0 & 0 & 0 \\ 0 & \left[a_d\right] & 0 & 0 \\ 0 & 0 & \left[a_d\right] & 0 \\ 0 & 0 & 0 & \left[a_d\right] \end{bmatrix} \text{ and } \left[a_d\right] = \begin{bmatrix} -2/\tau_c & -(1/\tau_c)^2 \\ 1 & 0 \end{bmatrix} \tag{3.24}$$

$$\left[B_d\right] = \begin{bmatrix} \left[b_d\right] & 0 & 0 & 0 \\ 0 & \left[b_d\right] & 0 & 0 \\ 0 & 0 & \left[b_d\right] & 0 \\ 0 & 0 & 0 & \left[b_d\right] \end{bmatrix} \text{ and } \left[b_d\right] = \begin{bmatrix} 1 \\ 0 \end{bmatrix} \tag{3.25}$$

The output gains of the derivative stage, $\{E_{cgd}\}$, are given by:

$$\left\{E_{cgd}\right\} = \left\{E_{\dot{y}d} \quad E_{\dot{\theta}yd} \quad E_{\dot{z}d} \quad E_{\dot{\theta}zd}\right\}^T = \left[C_d\right]\left\{Q_d\right\} \tag{3.26}$$

where

$$\left[C_d\right]=\begin{bmatrix}(1/\tau_c)^2 & 0 & 0 & 0 & 0 & 0 & 0 & 0\\ 0 & 0 & (1/\tau_c)^2 & 0 & 0 & 0 & 0 & 0\\ 0 & 0 & 0 & 0 & (1/\tau_c)^2 & 0 & 0 & 0\\ 0 & 0 & 0 & 0 & 0 & 0 & (1/\tau_c)^2 & 0\end{bmatrix} \tag{3.27}$$

The proportional error, $\{E_{cgp}\}$, and the derivative error, $\{E_{cgd}\}$, become the inputs for the filter stages. The state space representation of the filter stage is written as:

$$\left\{\dot{Q}_f\right\}=\left[A_f\right]\left\{Q_f\right\}+\left[B_f\right]\left\{\left\{E_{cgp}\right\}+\left\{E_{cgd}\right\}\right\} \tag{3.28}$$

$$\left\{V_f\right\}=\left\{V_{yf} \quad V_{\theta yf} \quad V_{zf} \quad V_{\theta zf}\right\}=\left[C_f\right]\left\{Q_f\right\} \tag{3.29}$$

where the coefficient matrices, $[A_{filt}]$ and $[B_{filt}]$, are determined in the Matlab code using the "tf2ss" function. A coordinate transformation is used such that the output voltages $\{V_f\}$ in c.g. coordinates are converted to corresponding voltages for the magnetic bearing coordinates, $\{V_c\}$. The equation describing the transformation is stated as:

$$\begin{Bmatrix}V_{ycA}\\ V_{ycB}\\ V_{zcA}\\ V_{zcB}\end{Bmatrix}=\left(\frac{1}{L_{mA}+L_{mB}}\right)\begin{bmatrix}L_{mB} & 1 & 0 & 0\\ L_{mA} & -1 & 0 & 0\\ 0 & 0 & L_{mB} & -1\\ 0 & 0 & L_{mA} & 1\end{bmatrix}\begin{Bmatrix}V_{yf}\\ V_{\theta yf}\\ V_{zf}\\ V_{\theta zf}\end{Bmatrix} \tag{3.30}$$

or more compactly as:

$$\{V_c\}=\left[T_{cg/mag}\right]\left\{V_f\right\}=\left[T_{cg/mag}\right]\left[C_f\right]\left\{Q_f\right\} \tag{3.31}$$

The voltages $\{V_c\}$ are the inputs to the power amplifiers corresponding to each bearing axis.

3.4 Power Amplifier Model

Power amplifiers are used to drive current in the coils of the magnetic bearings. A power amplifier is dedicated to each of the four radial control axes. The coil circuit load on an individual power amplifier, depicted in figure 3.4, consists of a nominal resistance, *R*, and inductance, *L*.

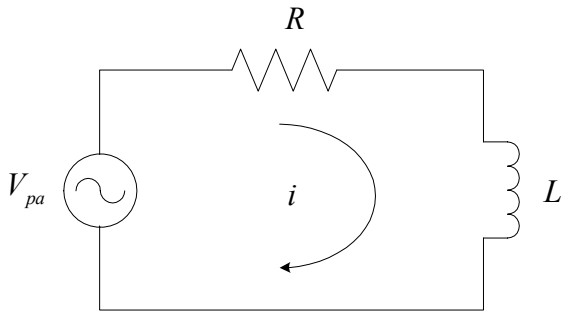

Figure 3.4: Power Amplifier and Magnetic Bearing Coil Circuit

Applying Kirchoff's Voltage Law yields the differential equation:

$$\frac{di}{dt} = \frac{1}{L}(V_{pa} - iR) \tag{3.32}$$

or in the frequency domain:

$$\frac{i}{V_{pa}} = \frac{1}{Ls + R} \tag{3.33}$$

The voltage of the power amplifier, V_{pa}, is determined by the controller input voltage and characteristics of the power amplifier. Typically, amplifiers utilizing pulse width modulation (PWM) are used in lieu of linear amplifiers due to their higher efficiency. The PWM amplifier model using current feedback is shown in figure 3.5:

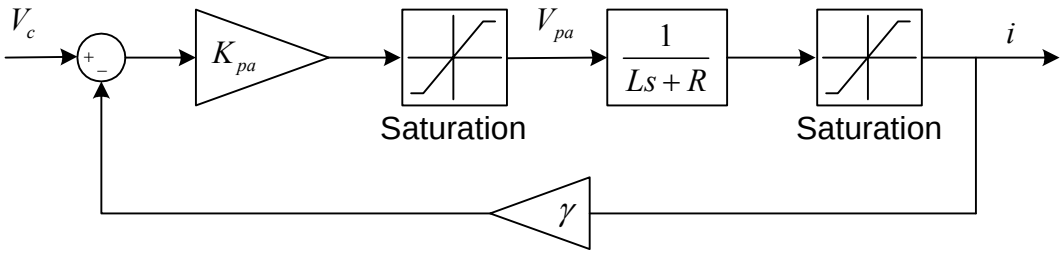

Figure 3.5: Power Amplifier Model

With reference to figure 3.4, V_{pa} can be stated as:

$$V_{pa} = K_{pa}(V_c - i\gamma) \tag{3.34}$$

where V_c is the desired voltage, K_{pa} is the amplifier reference gain, and γ is the current feedback sensitivity. Substituting equation (3.34) into (3.32) yields the final form for the current state as:

$$\frac{di}{dt} = \frac{1}{L}\left[K_{pa}(V_c - i\gamma) - iR\right] \tag{3.35}$$

The values of K_{pa} and γ are unknown but can be calculated based on measurements or published values for the controller bandwidth and DC gain. For example, consider the transfer function of the power amplifier system which can be stated as:

$$G_{pa}(s) = \frac{i}{V_c} = \frac{K_{pa}}{Ls + R + K_{pa}\gamma} \tag{3.36}$$

Rearranging yields the form:

$$G_{pa}(s) = \frac{i}{V_{pa}} = \frac{\dfrac{K_{pa}}{R + K_{pa}\gamma}}{\dfrac{L}{R + K_{pa}\gamma}s + 1} \tag{3.37}$$

From inspection of equation (3.37), the time constant of the first order filter can be defined as:

$$\tau = \frac{L}{R + K_{pa}\gamma} \tag{3.38}$$

The amplifier cutoff frequency in rad/sec is defined as:

$$f_{pa} = \frac{1}{2\pi\tau} \tag{3.39}$$

Substituting equation (3.38) into equation (3.39) yields:

$$f_{pa} = \frac{R + K_{pa}\gamma}{2\pi L} \tag{3.40}$$

A relation for the DC gain of the system, K_{pa}^{DC}, is obtained by letting s go to zero in equation (3.37) yielding:

$$K_{pa}^{DC} = \lim_{s \to 0} G_{pa}(s) = \frac{K_{pa}}{R + K_{pa}\gamma} \tag{3.41}$$

Solving equations (3.40) and (3.41) for K_{pa} and γ results in the following expressions:

$$K_{pa} = 2\pi L f_{pa} K_{pa}^{DC} \tag{3.42}$$

$$\gamma = \frac{2\pi L f_{pa} - R}{2\pi L f_{pa} K_{pa}^{DC}} \tag{3.43}$$

where K_{pa}^{DC} and f_c are determined from experimental measurement. With reference to equation (3.35) and the above definitions for an individual amplifier circuit, the state space form for all of the power amplifier circuits is written as:

$$\{\dot{Q}_i\} = [A_i]\{Q_i\} + [B_i]\{V_c\} \tag{3.44}$$

where

$$\{Q_i\} = \{i_{yA} \quad i_{yB} \quad i_{zA} \quad i_{zB}\}^T \tag{3.45}$$

$$[A_i] = -\frac{(K_{pa}\gamma + R)}{L}[I]_{(4x4)} \tag{3.46}$$

$$[B_i] = (K_{pa}/L)[I]_{(4x4)} \tag{3.47}$$

The outputs of these states are the magnetic bearing forces as described in the next section.

3.5 Magnetic Bearing Model

The magnetic bearing is an actuator that provides non-contacting forces to support the rotor. A linear relation between the magnetic bearing forces, coil currents, and rotor position are required for the bearing analytical model. These expressions are derived for the combination bearing and applicable to the radial bearing which is of similar construction. Since the radial response of the rotor is of primary interest the thrust axis is not considered.

The configuration of the combination bearing is of the homopolar, permanent magnet bias type as shown in figure 3.6. This design can be viewed as six electromagnets (EM), four radial and two axial, working in conjunction with four arch shaped permanent

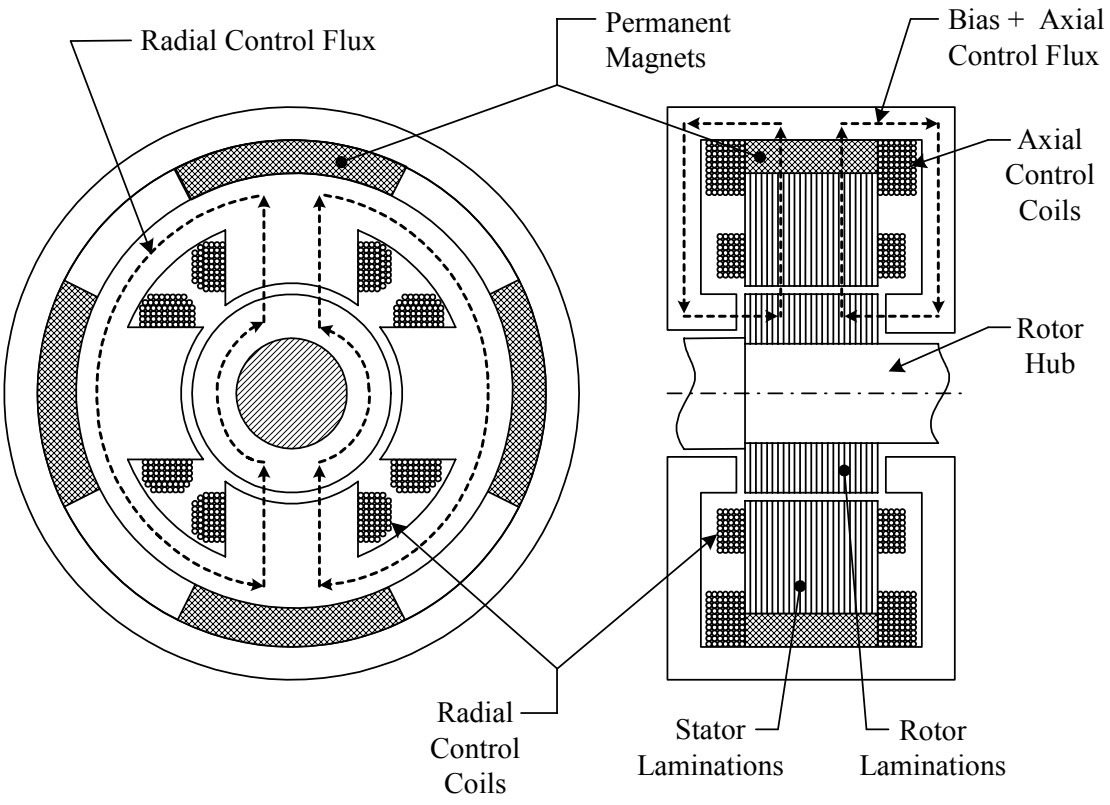

Figure 3.6: Combination Magnetic Bearing Schematic

magnets (PM) to drive magnetic flux in the bearing air gaps. The magnetic flux, ϕ, in each air gap generates a force on the rotor given by the expression:

$$F = \frac{\phi^2}{2\mu_o A_g} \tag{3.48}$$

where u_o is the relative permeability of free space and A_g is the projected area of the air gap on the rotor. With reference to the radial plane, homopolar refers to the flux driven by the PM that trace paths parallel to the rotor axis and uniformly into or out of the radial poles. If the rotor deviates from the centered position by a small amount the PM flux results in a net force in the direction of deviation. To overcome this instability, the current in the EM coils are driven by the power amplifiers in proportion to the amount of deviation. A significant simplification occurs by noting the large reluctance of the permanent magnets restricts the flux of the radial EMs from flowing axially and thereby uncouples the radial and axial EMs. Hence, the radial forces are due to the radial EM flux, ϕ_{em} , and the PM flux, ϕ_{pm} , in the four radial air gaps, #1 through #4. Consider air gaps #1 and #3 which comprise the forces along the *Y* axis. For a rotor displacement in the positive *Y* direction, the total magnetic force is given as:

$$F_y = \frac{(\phi_{pm1} + \phi_{em1})^2}{2\mu_o A_g} - \frac{(\phi_{pm3} - \phi_{em3})^2}{2\mu_o A_g} \tag{3.49}$$

Lee [7] derives expressions for the flux terms in equation (3.49) which are stated here for reference as:

$$\phi_{pm1} = \frac{\mu_o A_g A_p bBB_o}{2(G-y)\mu A_p + b\mu_o A_g} \qquad \phi_{pm3} = \frac{\mu_o A_g A_p bBB_o}{2(G+y)\mu A_p + b\mu_o A_g} \tag{3.50}$$

$$\phi_{em1} = \mu_o A_g N i_{13} \frac{2G+y}{2G^2 - y^2} \qquad \phi_{em2} = \mu_o A_g N i_{13} \frac{2G-y}{2G^2 - y^2} \tag{3.51}$$

where

μ : slope of the demagnetization curve of a PM

A_p: pole face area of each PM

b : radial thickness of a PM

B : PM magnetic flux density

B_o: PM residual magnet flux density

G : nominal air gap

i_{13}: coil currents for poles #1 and #3

Substituting equations (3.50) and (3.51) into equation (3.49) yields a nonlinear force with respect to coil currents and rotor position. Typically, this force is linearized about an operating point corresponding to a static rotor in the centered position. The Taylor series expansion used to do this is written as:

$$F_y(i_{13}, y) = F_y(0,0) + \left.\frac{\partial F_y}{\partial i_{13}}\right|_{\substack{i=0\\y=0}} i_1 + \left.\frac{\partial F_y}{\partial y}\right|_{\substack{i=0\\y=0}} y \tag{3.52}$$

The first term goes to zero, as expected for a perfectly centered rotor and zero control flux, while the remaining terms can be rewritten as:

$$F_y(i_{13,}y) = K_i i_{13} + K_d y \tag{3.53}$$

The terms K_i and K_d are known as the current and position stiffness, respectively, and are given by Lee [7] as:

$$K_i = \frac{4NA_gB_g}{G} \tag{3.54}$$

$$K_D = \frac{8\mu A_g A_p B_g^2}{\mu_o(2G\mu A_p + b\mu_o A_g)} \tag{3.55}$$

These definitions are extended to all four radial bearing axes such that forces related to the control currents are given by:

$$\begin{Bmatrix} F_{cyA} \\ F_{cyB} \\ F_{czA} \\ F_{czB} \end{Bmatrix} = \begin{bmatrix} K_{iA} & 0 & 0 & 0 \\ 0 & K_{iB} & 0 & 0 \\ 0 & 0 & K_{iA} & 0 \\ 0 & 0 & 0 & K_{iB} \end{bmatrix} \begin{Bmatrix} i_{yA} \\ i_{yB} \\ i_{zA} \\ i_{zB} \end{Bmatrix} \tag{3.56}$$

The forces due to position stiffness will be accounted for separately in the derivation of the rotor equations of motion.

3.6 Rotor Unbalance Modeling

The inherent nature of bearings is to constrain the rotation of a shaft about some geometric axis. Rotor unbalance occurs when this geometric axis of rotation is not

coincident with the principle axis of inertia nearest the axis of rotation. The error in making these axes coincident is initially due to manufacturing errors in geometric dimensions or non-homogeneity of materials. Therefore, balancing machines are employed to realign the inertial and geometric axes. However, the limitation on the precision of balancing machines ultimately requires some error or residual unbalance to be present. In this case, the unbalance of the rotor is comprised of two parts: the residual unbalance left over after balancing the rotor and the unbalance generated by the asymmetric growth (preload loss) of the PLM flywheel during operation.

The residual unbalance is modeled such that it creates a disturbance force in the rotor equations of motion. The force is derived by considering the rotor lumped mass, *m*, to be accelerating due to shaft rotation at a distance *e* from the axis of rotation. The equation is stated as:

$$F = me\omega^2 \cos(\omega t + \phi) \tag{3.57}$$

where *e* is referred to as the mass eccentricity, ω is the rotor angular velocity, and ϕ is the phase of the unbalance force relative to the Y axis. The value of the eccentricity is essentially what determines the amount of unbalance. To obtain some meaningful values for the simulation the ISO 1940-1:2003 standard [8] for balancing of rigid rotors is consulted. Based on the mass of the PLM rotor, the maximum allowed rotor mass eccentricity for various tolerance grades are listed in table 3.1. Two balancing planes are required to balance the rotor. Therefore, the ISO standard recommends the maximum allowed eccentricities in table 3.1 be divided between the two planes. With this in mind, the residual unbalance forces along the *Y* and *Z* axis at balance plane "A", as depicted in figure 3.2, are given by:

$$F_{yrA} = \frac{1}{2} me_r \omega^2 \cos(\omega t + \phi_{rA}) \tag{3.58}$$

$$F_{zrA} = \frac{1}{2} me_r \omega^2 \cos(\omega t + \phi_{rA} - \pi/2) \tag{3.59}$$

In addition, the forces at balance plane "B" are given by:

$$F_{yrB} = \frac{1}{2} me_r \omega^2 \cos(\omega t + \phi_{rB}) \tag{3.60}$$

$$F_{zrB} = \frac{1}{2} m e_r \omega^2 \cos(\omega t + \phi_{rB} - \pi/2) \tag{3.61}$$

Table 3.1: PLM Maximum Rotor Mass Eccentricity vs. ISO Tolerance Grades

ISO Tolerance Grade	Maximum Allowed Eccentricity of PLM Rotor (in.)
G1	.000008
G2.5	.000019
G6.3	.000047
G16	.000120

The change in mass eccentricity due to the preload loss event is distributed between the two balance planes and modeled in a similar manner as the residual unbalance. Hence, the unbalance forces along the Y and Z axis are stated as:

$$F_{yPLM} = \frac{1}{2} m e_{PLM} \omega^2 \cos(\omega t + \phi_{PLM}) \tag{3.62}$$

$$F_{zPLM} = \frac{1}{2} m e_{PLM} \omega^2 \cos(\omega t + \phi_{PLM} - \pi/2) \tag{3.63}$$

The UT-CEM predicted mass eccentricity vs. angular velocity for the PLM rotor is depicted in figure 3.7. The eccentricity, e_{plm}, is speed dependent since centripetal acceleration drives the asymmetric outer ring growth. At this point, the equations for unbalance defined above can be incorporated into the derivation of the rotor equations of motion. To summarize, the total unbalance forces at the balance planes due to residual and the PLM unbalance are summarized below.

$$F_{yuA} = F_{yrA} + F_{yPLMA} \qquad F_{zuA} = F_{zrA} + F_{zPLMA} \tag{3.64}$$

$$F_{yuB} = F_{yrB} + F_{yPLMB} \qquad F_{zuB} = F_{zrB} + F_{zPLMB} \tag{3.65}$$

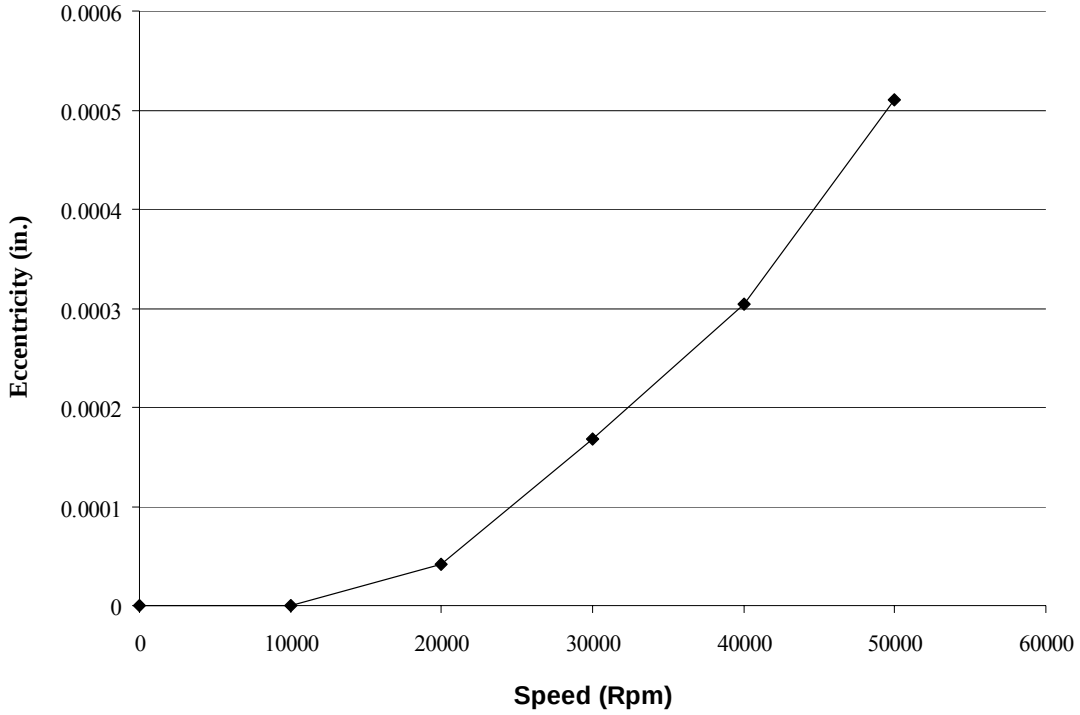

Figure 3.7: UT-CEM Predicted PLM Rotor Mass Eccentricity vs. Speed

3.7 Rigid Body Rotor Model

The levitated PLM rotor is modeled as a rigid body with four degrees of freedom at the c.g. defined as:

$$\{X\} = \begin{Bmatrix} Y \\ Z \\ \theta_y \\ \theta_z \end{Bmatrix} \tag{3.66}$$

The control forces and negative position stiffness of the radial and combo magnetic bearings are the only external forces considered. Radial and axial dynamic components are assumed to be uncoupled and since the radial response is of primary interest, an axial degree of freedom is not considered. Figure 3.8 depicts the free body diagram of the rotor.

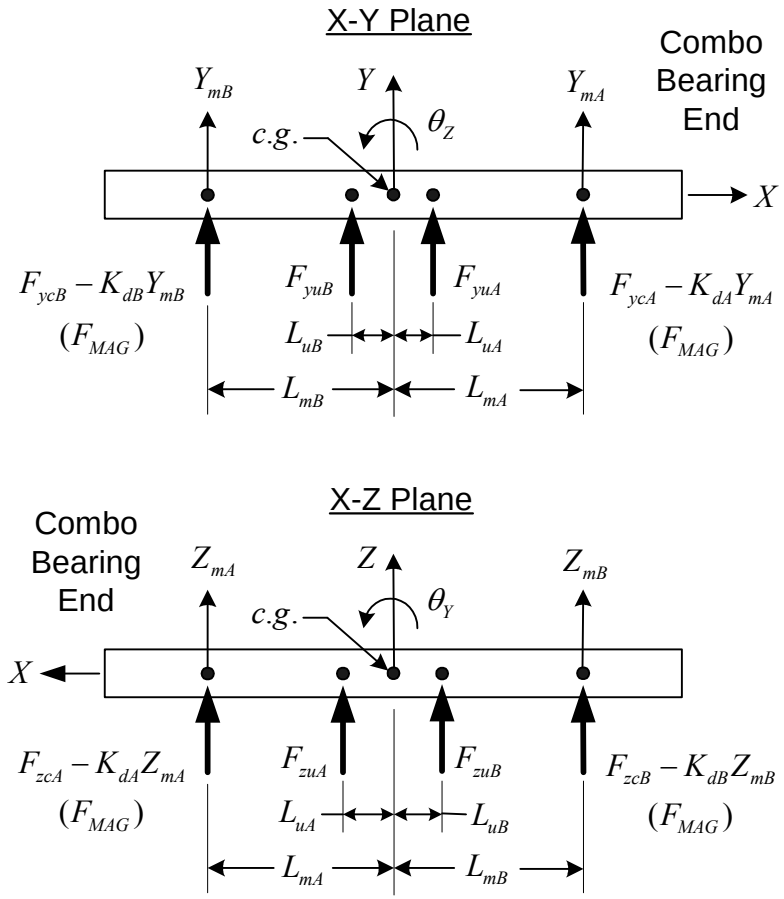

Figure 3.8: Free Body Diagrams of Rigid Rotor

Applying Newton's law at the c.g. of the rotor yields the equations of motion:

$$M\ddot{Y} = F_{ycA} + F_{ycB} - K_{dA}Y_{mA} - K_{dB}Y_{mB} + F_{yuA} + F_{yuB} \tag{3.67}$$

$$M\ddot{Z} = F_{zA}^{c} + F_{zB}^{c} - K_{dA}Z_{mA} - K_{dB}Z_{mB} + F_{zuA} + F_{zuB} \tag{3.68}$$

$$I_T\ddot{\theta}_Y = -F_{zcA}L_{mA} + F_{zcB}L_{mB} + K_{dA}Z_{mA}L_{mA} - K_{dB}Z_{mB}L_{mB} - I_p\omega\dot{\theta}_Z - F_{zuA}L_{uA} + F_{zuB}L_{uB} \tag{3.69}$$

$$I_T\ddot{\theta}_Z = F_{ycA}L_{mA} - F_{ycB}L_{mB} - K_{dA}Y_{mA}L_{mA} + K_{dB}Y_{mB}L_{mB} + I_p\omega\dot{\theta}_Z + F_{yuA}L_{uA} - F_{yuB}L_{uB} \tag{3.70}$$

Assuming small motions the transformation from the magnetic bearing coordinates to the c.g. coordinates is:

$$Y_{mA} = Y + L_{mA}\theta_Z \tag{3.71}$$

$$Y_{mB} = Y - L_{mB}\theta_Z \tag{3.72}$$

$$Z_{mA} = Z - L_{mA}\theta_Y \tag{3.73}$$

$$Z_{mB} = Z + L_{mB}\theta_Y \tag{3.74}$$

Substituting equations (3.71)-(3.74) into equations (3.67)-(3.70), the equations of motion can be written in matrix form as:

$$[M]\{\ddot{X}\} + [C]\{\dot{X}\} + [K]\{X\} = \{F(t)\} \tag{3.75}$$

where

$$\{X\} = \{Y \quad Z \quad \theta_Y \quad \theta_Z\}^T \tag{3.76}$$

$$[M] = \begin{bmatrix} m & 0 & 0 & 0 \\ 0 & m & 0 & 0 \\ 0 & 0 & I_T & 0 \\ 0 & 0 & 0 & I_T \end{bmatrix} \tag{3.77}$$

$$[C] = \begin{bmatrix} 0 & 0 & 0 & 0 \\ 0 & 0 & 0 & 0 \\ 0 & 0 & 0 & -I_p\omega \\ 0 & 0 & I_p\omega & 0 \end{bmatrix} \tag{3.78}$$

$$[K] = \begin{bmatrix} -K_{dA} - K_{dB} & 0 & 0 & -K_{dA}L_{mA} + K_{dB}L_{mB} \\ 0 & -K_{dA} - K_{dB} & K_{dA}L_{mA} - K_{dB}L_{mB} & 0 \\ 0 & K^A_{ps}L_{mA} - K^B_{ps}L_{mB} & -K_{dA}(L_{mA})^2 - K_{dB}(L_{mB})^2 & 0 \\ -K_{dA}L_{mA} + K_{dB}L_{mB} & 0 & 0 & -K_{dA}(L_{mA})^2 - K_{dB}(L_{mB})^2 \end{bmatrix} \tag{3.79}$$

$$\{F(t)\} = \begin{Bmatrix} F_{ycA} + F_{ycB} + F_{yuA} + F_{yuB} \\ F_{zcA} + F_{zcB} + F_{zuA} + F_{zuB} \\ -F_{zcA}L_{AM} + F_{zcB}L_{BM} - F_{zuA}L_{uA} + F_{zuB}L_{uB} \\ -F_{ycA}L_{AM} - F_{ycB}L_{BM} + F_{yuA}L_{uA} - F_{yuB}L_{uB} \end{Bmatrix} \tag{3.80}$$

To implement these equations in the simulation code we must obtain an equivalent set of first order equations. Consider equation (3.75) rewritten as:

$$\begin{bmatrix} [M] & [0] \\ [0] & [I] \end{bmatrix} \begin{Bmatrix} \{\ddot{X}\} \\ \{\dot{X}\} \end{Bmatrix} + \begin{bmatrix} [C] & [K] \\ [-I] & [0] \end{bmatrix} \begin{Bmatrix} \{\dot{X}\} \\ \{X\} \end{Bmatrix} = \begin{Bmatrix} \{F(t)\} \\ \{0\} \end{Bmatrix} \tag{3.81}$$

To obtain a set of first order equations a state variable is defined as:

$$\{Q_{dyn}\} = \begin{Bmatrix} \{\dot{X}\} \\ \{X\} \end{Bmatrix} \tag{3.82}$$

Rearranging and combining equations (3.81) and (3.82) the first order form is:

$$\{\dot{Q}_{dyn}\} = [A_{dyn}]\{Q\} + [B_{dyn}]\{U\} \tag{3.83}$$

where

$$[A_{dyn}] = \begin{bmatrix} -[M]^{-1}[C] & -[M]^{-1}[K] \\ [I] & [0] \end{bmatrix} \tag{3.84}$$

$$\{F(t)\} = \begin{Bmatrix} [M]^{-1}\{F(t)\} \\ \{0\} \end{Bmatrix} \tag{3.85}$$

3.8 Simulation Results

A program was created using Matlab software to investigate the steady state response of the rotor-bearing system. The state space models developed previously for each component are assembled such that the entire system can be written in standard form described by equation (3.1). The total "A" coefficient matrix of the system is constructed from the component coefficient matrices as:

$$[A_T] = \begin{bmatrix} [A_s] & 0 & 0 & 0 & 0 & [B_s][T_{cg/s}] \\ [B_p][T_{s/cg}][C_s] & [A_p] & 0 & 0 & 0 & 0 \\ [B_d][T_{s/cg}][C_s] \rightarrow & \cdots\cdots\cdots & [A_d] & 0 & 0 & 0 \\ 0 & [B_f][C_p] & [B_f][C_d] & [A_f] & 0 & 0 \\ 0 & 0 & 0 & [B_i][T_{cg/mcg}][C_f] & [A_i] & 0 \\ 0 & 0 & 0 & 0 & [B_{dyn}][C_i] & [A_{dyn}] \end{bmatrix} \tag{3.86}$$

The disturbance inputs simply consist of the residual unbalance, runout, and unbalance due to the PLM mass eccentricity. The set of first order differential equations is solved using the Matlab ODE45 solver. Also, initial conditions for all states are set to zero at time equal to zero. In each of the results to be presented the solution is carried out to

steady state and the response amplitudes captured. The input parameters for the simulation are depicted in table 3.2.

Table 3.2: Simulation Input Parameters

Description	Value
Rotor Mass, M	19.6 lbs
Rotor Polar Inertia, Ip	64.8 lb-in2
Rotor Transverse Inertia, It	189.9 lb-in2
Distance, c.g. to Bearing "A", L_{mA}	3.644 in.
Distance, c.g. to Bearing "B", L_{mB}	3.166 in.
Distance, c.g. to Sensor "A", L_{sA}	5.274 in.
Distance, c.g. to Sensor "B", L_{sB}	5.086 in.
Distance, c.g. to Balance Plane "A", L_{uA}	2.375 in.
Distance, c.g. to Balance Plane "B", L_{uB}	1.625 in.
Bearing "A" Current Stiffness, K_{iA}	9.3 lb/A
Bearing "B" Current Stiffness, K_{iB}	8.8 lb/ A
Bearing "A" Position Stiffness, K_{iA}	6900 lb/in.
Bearing "B" Position Stiffness, K_{iB}	6160 lb/in.
Sensor Gain, ζ_s	200 V/in.
Sensor Cutoff Frequency	3000 Hz
Power Amplifier Cutoff Frequency, f_{pa}	2000 Hz
Controller Cutoff Frequency	3000 Hz

Figures 3.9 through 3.15 depict the simulation results. Each figure provides displacement magnitudes at the two sensor locations "A" and "B" as well as the current magnitudes of bearings "A" and "B". These displacement and current magnitudes are used as a means to identify changes in response due to PLM change in mass eccentricity.

The displacement and bearing current response are investigated as shaft runout, use of notch filters, and phase of the unbalance vectors is varied.

Figures 3.9 through 3.11 depict steady state operation without the use of a notch filter. In each of the three plots, the response due only to the residual unbalance slowly approaches the residual mass eccentricity at higher speeds as expected. The addition of the PLM eccentricity and runout yields several notable trends. First, the changes in current magnitudes are on the order of several amps which are readily detectable. However, in figure 3.9 it is evident that the addition of the PLM mass eccentricity can initially improve the balance state thus requiring speeds as high as 40,000 Rpm to see significant changes in response. Figures 3.10 and 3.11 depict the results when .0005 and .001 inches of total indicated runout are added. In this case, all of the response curves shift upward with similar changes in magnitude when compared to cases without runout. However, an important difference is that depending on the relative phase, the unbalance and runout vectors can add to produce a continuous decline in response as seen in figure 3.11. Therefore, a sharp decrease in current response would also be an indicator of an increase in the PLM mass eccentricity. Keeping the total indicated runout levels below .0005 inches is an attainable tolerance and would ensure a more consistent positive response.

Figures 3.12 through 3.15 incorporate the same combinations of residual unbalance, PLM mass eccentricity, and runout as figures 3.9 to 3.11. However, a notch filter is incorporated at the spin speed. This is sometimes used in magnetic bearing systems to reduce unnecessary bearing response to unbalance or reduce excitation of certain modes of vibration. As evidenced in figures 3.9 to 3.11, the magnetic bearing currents approach zero depending on the magnitude of the notch filter. As a result, the sensor displacements must be used for detection of the PLM mass eccentricity change. The changes in displacements at the sensors are of similar magnitude for all cases with and without the notch. The magnitude is reported in the plots as an orbit radius which is doubled to yield a peak to peak displacement value. Based on experience in the VCEL, peak to peak noise levels can be as high as 50 mV due to the brushless motors and magnetic bearing power amplifiers present in the PLM test rig. This voltage level

corresponds to about .00025 inches of measured displacement. With this in mind, sufficient changes in displacement magnitude at the sensors occur at speeds as low as 30,000 Rpm for cases in which the PLM eccentricity phase is favorable. However, as depicted in figure 3.12, the PLM eccentricity can initially improve the balance state and lower the response before eventually providing a significant change in amplitude at approximately 40,000 Rpm. The addition of runout above .0005 inches can lead to a decline in measured response over much of the speed range as seen in figure 3.14. Therefore, the absolute value of the change in response magnitude must be used as an indication of the preload loss event.

In conclusion, it is expected that for all cases a sufficient change in measurements for position or current will occur for speeds above 40,000 Rpm. Detection of the eccentricity change would be accomplished via measurements of the magnetic bearing currents when the controller does not utilize a notch filter. Position sensor measurements would have to be utilized during operation with a notch filter at the running speed. However, the signal to noise ratio is expected to be more favorable when currents are monitored.

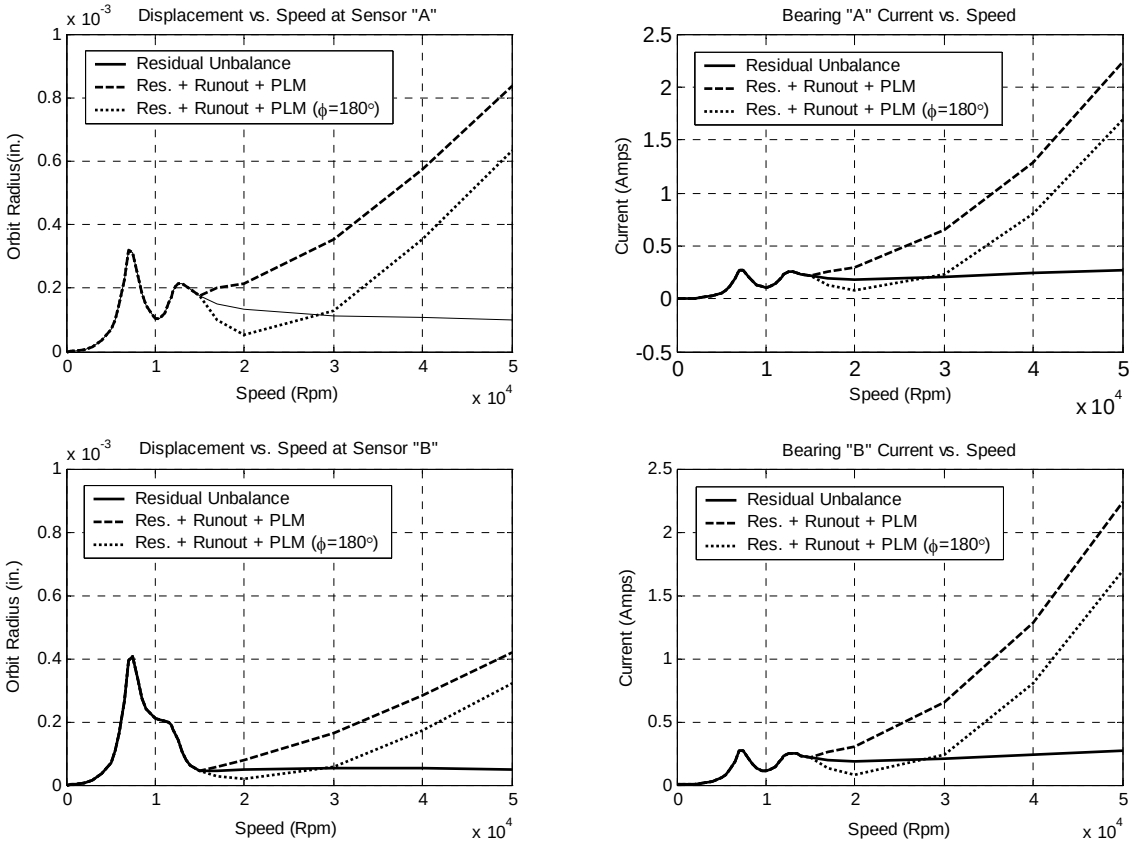

Figure 3.9: Steady State Response with Residual and PLM Unbalance

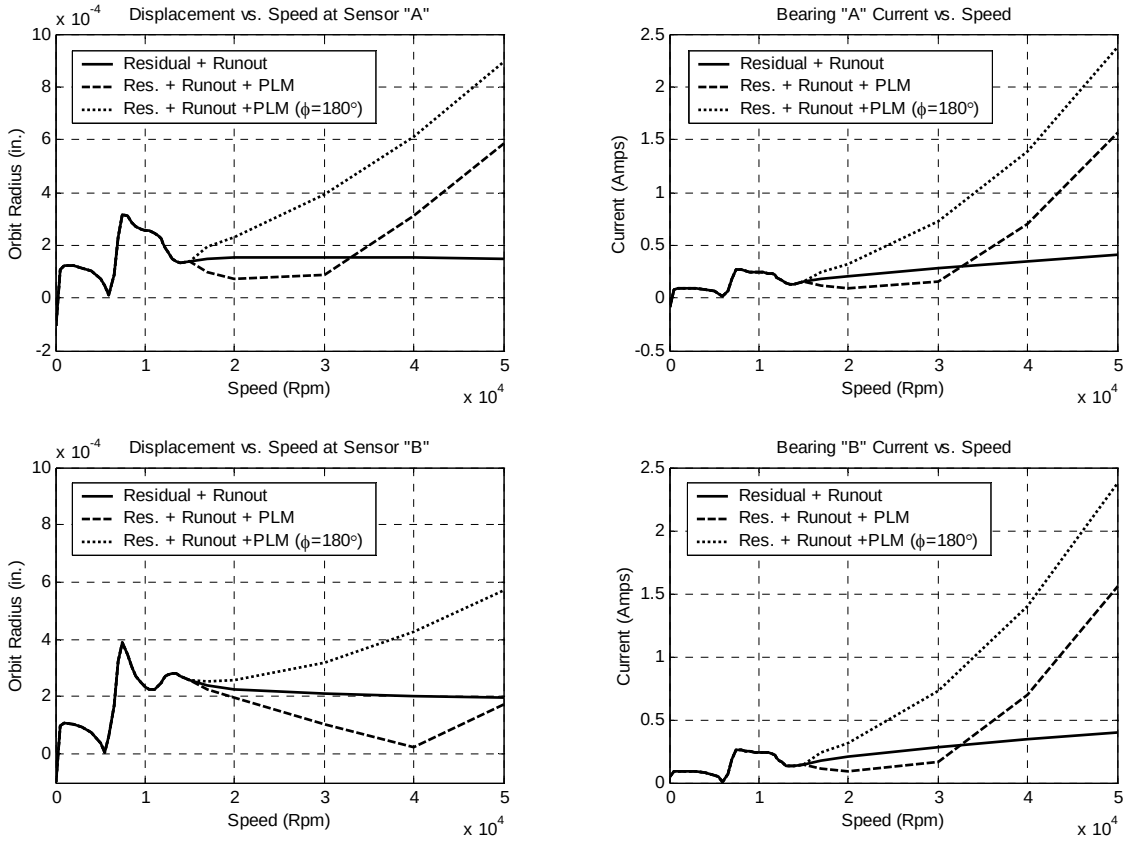

Figure 3.10: Steady State Response with Residual + PLM + .0005 TIR

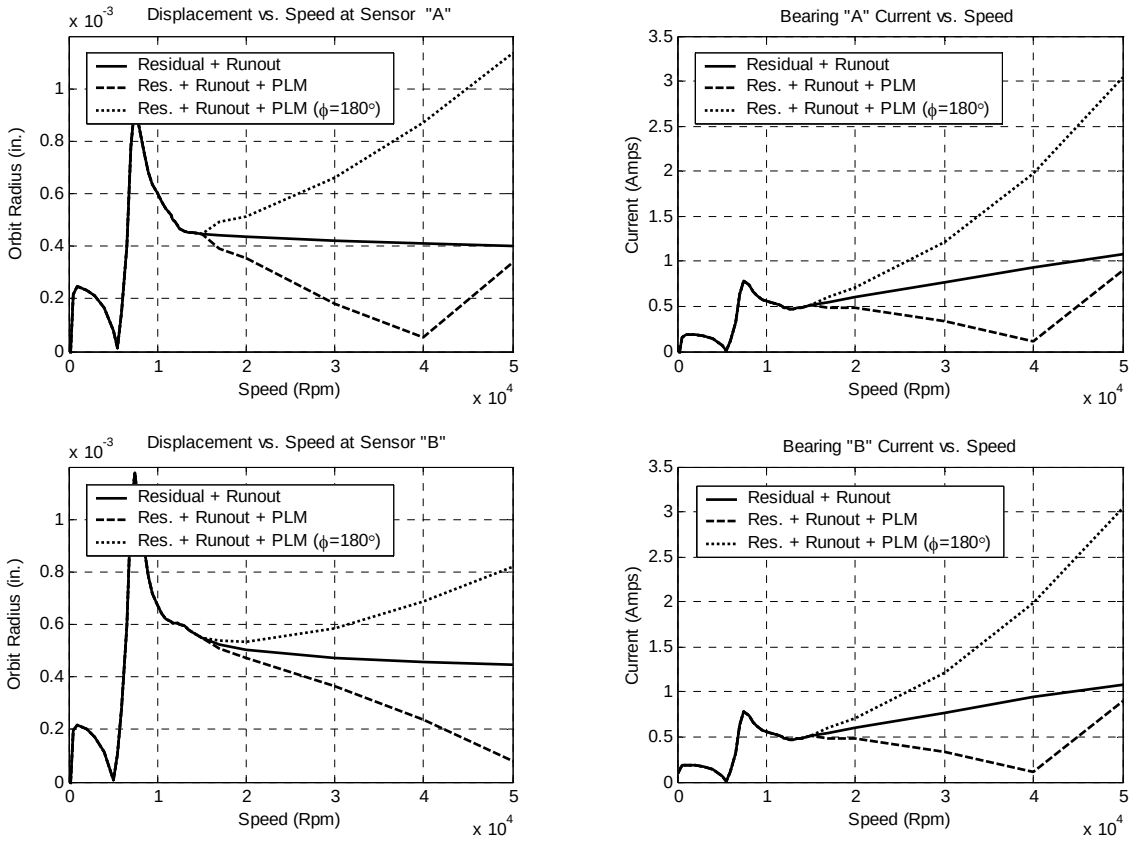

Figure 3.11: Steady State Response with Residual + PLM + .001 TIR

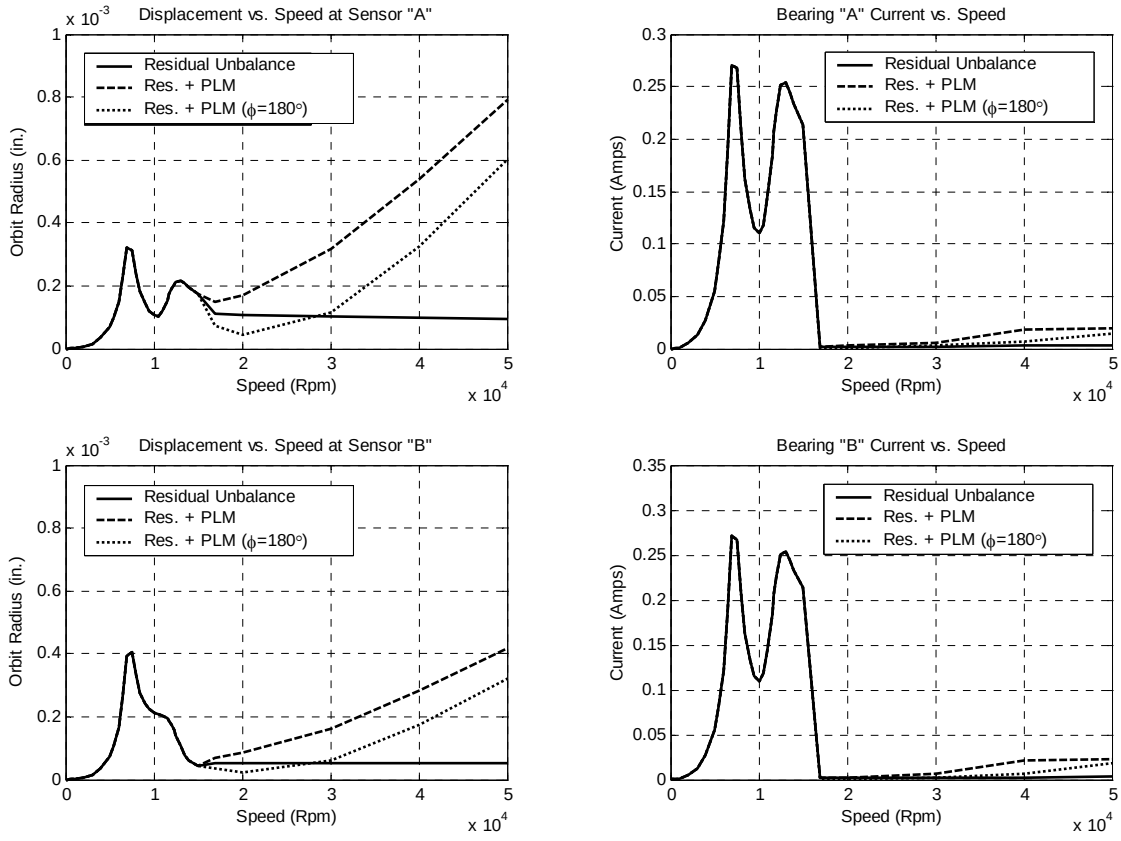

Figure 3.12: Steady State Response with Residual + PLM + Notch

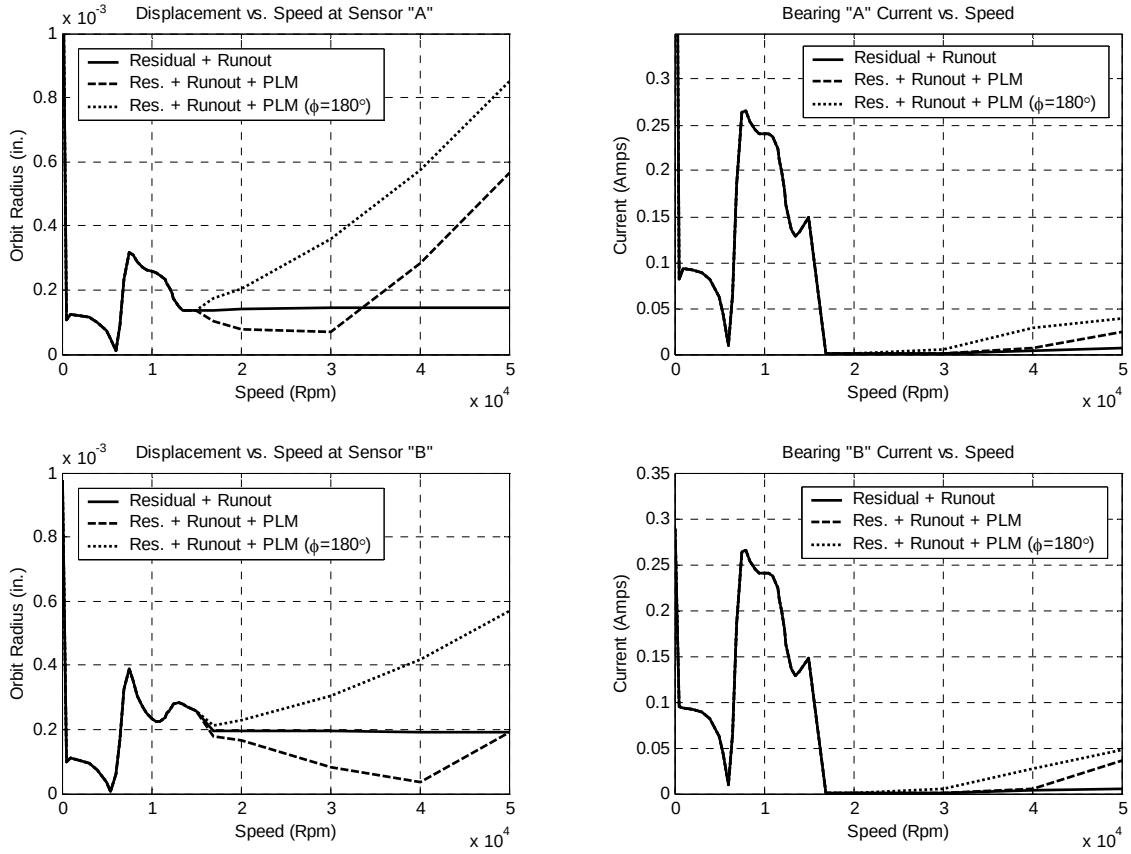

Figure 3.13: Steady State Response with Residual + PLM + Notch + .0005 TIR

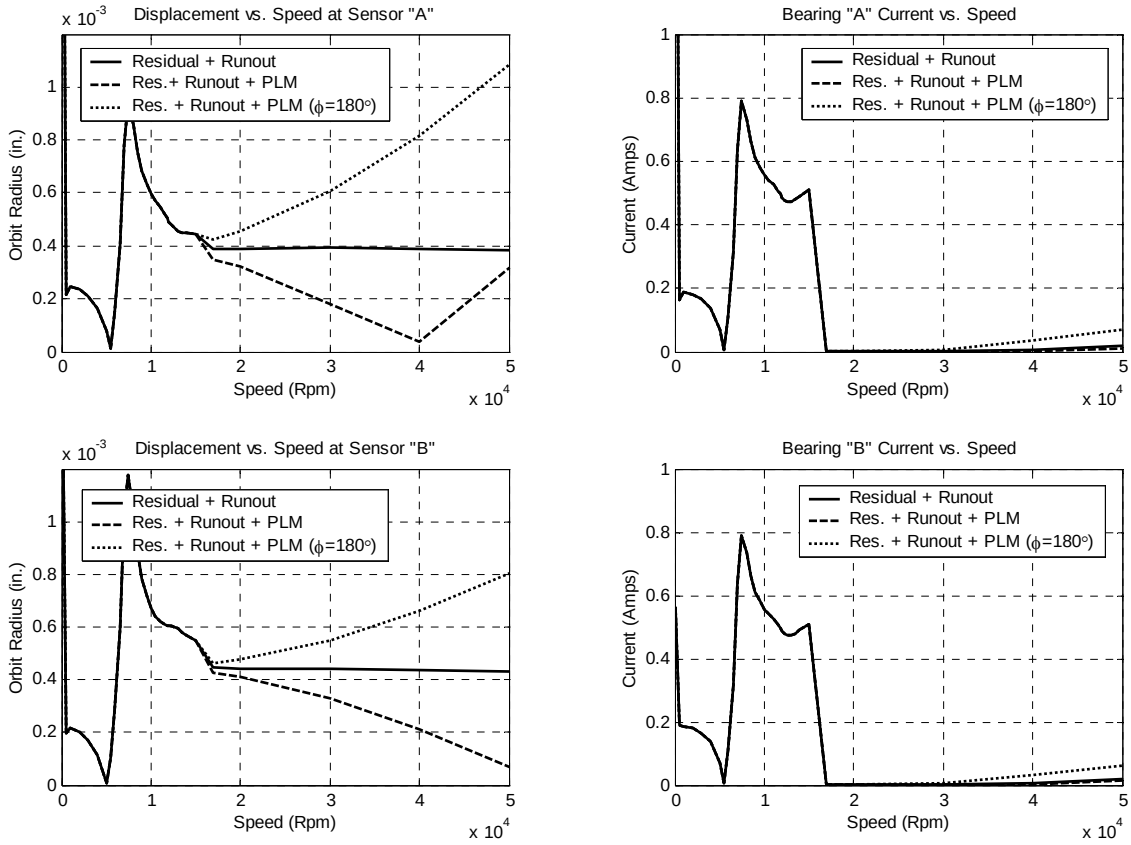

Figure 3.14: Steady State Response with Residual + PLM + Notch + .001 TIR

CHAPTER IV

CRITICAL SPEED ANALYSIS

The basic objectives of a rotordynamic analysis include predictions of critical speeds, synchronous or non-synchronous rotor response with respect to shaft speed, and stability of the system. Critical speed predictions are addressed in this chapter while the later two objectives are explored in chapter III. A critical speed occurs when the shaft unbalance excites a particular natural frequency of the system to its maximum response [9]. Mathematically, this corresponds to the damped eigenvalue of the rotor system whose eigenvector is called the rotor mode shape. The critical speeds of the PLM test rig will be calculated utilizing the transfer matrix method for critical speeds due to rotor flexibility and the state space equations developed in chapter III for the rigid body critical speeds. As will be shown, the rigid rotor and flexible rotor critical speeds are approximately independent due to the low rotor support stiffness of the magnetic suspension.

4.1 Rigid Body Critical Speeds

The state space equations used to describe the control and dynamics of the PLM rotor bearing system in chapter III are used here to predict the rigid rotor critical speeds. Rotor flexibility is considered negligible since the magnetic bearings provide relatively low support stiffness. Hence, the rigid body critical speeds depend on the stiffness of the actively controlled magnetic bearings. This support stiffness is a combination of the active stiffness, characterized by proportional control, and position stiffness due to the permanent magnets. A critical speed occurs when the rotor speed coincides with a damped eigenvalue derived from the system state space matrix, $[A_T]$. These speeds are identified using a Campbell diagram depicted in figure 4.1. The first critical speed at 7,127 Rpm corresponds to what is termed the cylindrical mode while the second critical speed at 12,056 Rpm corresponds to the conical mode. These speeds are well below the speed range of interest ranging from 20,000-50,000 rpm. Typically, the rigid body critical speeds are traversed with the aid of damping provided by the magnetic bearings.

This damping is associated with the controller derivative gain and is adjusted to obtain sufficient response at the critical speeds as well as stability throughout the speed range.

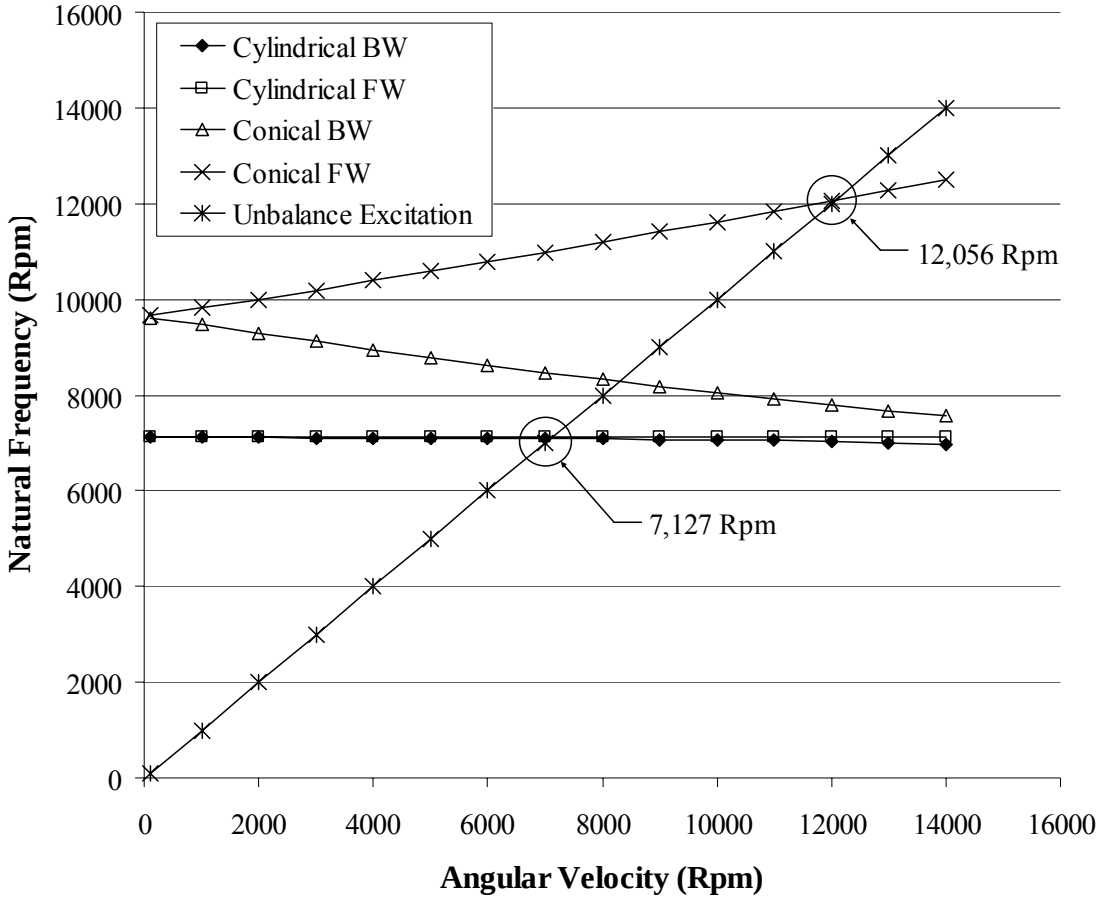

Figure 4.1: Rigid Body Critical Speeds

4.2 Transfer Matrix Method

The transfer matrix method described here can be used to predict critical speeds and mode shapes of a flexible rotor on undamped flexible supports [10]. The first step in modeling a rotor is to divide the length into n segments or stations. The number and individual length of stations is chosen such that the significant features of the shaft are accurately represented. Each station is then modeled by a spinning rigid disk or inertia

element connected to a massless elastic beam element. The resulting model of the rotor is n discs connected by n-1 beam elements as depicted in figure 4.2. The transfer matrices implied by the name of the procedure provide expressions for the boundary conditions on, for example, the right side of an inertia or beam element in terms of the left side. Ultimately, all of the transfer matrices are multiplied together such that the boundary conditions on the right side of the rotor are expressed in terms of the boundary conditions on the left. To obtain this total transfer matrix we begin by developing the transfer matrix for the individual shaft and inertia elements.

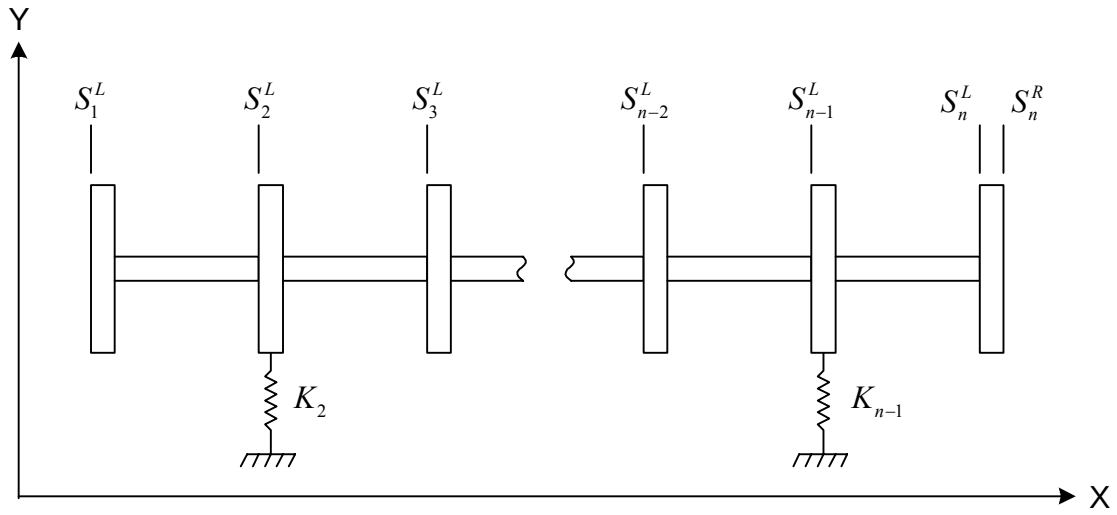

Figure 4.2: Typical Transfer Matrix Rotor Model

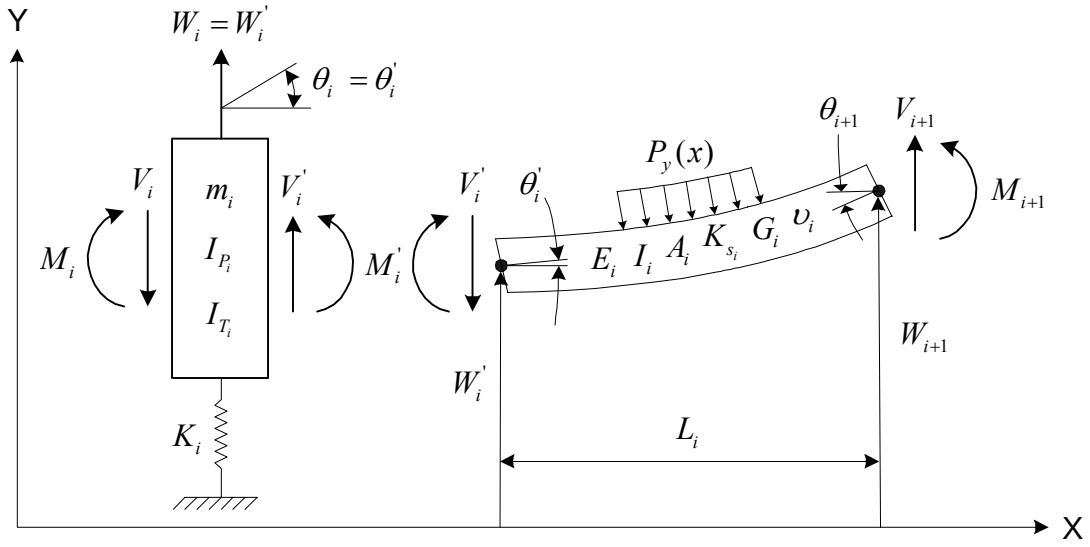

Figure 4.3: Inertia Element (Left) and Beam Element (Right) Free Body Diagram

Figure 4.3 depicts a free body diagram of the inertia and beam elements of the i^{th} station where:

W_i is defined as the lateral deflection.
θ_i is the slope due to bending.
M_i is the moment.
V_i is the shear force.
G_i is the shear modulus of elasticity.
A_i is the cross sectional area.
P_y is applied load per unit length.
m_i is the mass
Ip_i and It_i are the polar and transverse moments of inertia, respectively.
K_i is support or bearing stiffness.
L_i is the length

The disc is modeled as a rigid body with compliant support if a bearing is present at the station of interest. Gyroscopic effects are also to be included in the model. With this

in mind, the rigid body assumption requires that deflections on both sides of the disc be identical yielding:

$$W_i^R = W_i^L \tag{4.1}$$

$$\theta_i^R = \theta_i^L \tag{4.2}$$

With the assumption of forward synchronous whirl, rigid body kinematics provides the transformations for shear and moments as:

$$V_i^R = V_i^L + (K_i - m_i\omega^2)W_i^L \tag{4.3}$$

$$M_i^R = M_i^L + \omega^2(I_{pi} - I_{Ti})\theta_i^L \tag{4.4}$$

Equations (4.1)-(4.4) can be stated in matrix form as:

$$\begin{Bmatrix} W_i^R \\ \theta_i^R \\ V_i^R \\ M_i^R \end{Bmatrix} = \begin{bmatrix} 1 & 0 & 0 & 0 \\ 0 & 1 & 0 & 0 \\ \left(K_i - m_i\omega^2\right) & 0 & 1 & 0 \\ 0 & \omega^2(I_{Pi} - I_{Ti}) & 0 & 1 \end{bmatrix} \begin{Bmatrix} W_i^L \\ \theta_i^L \\ V_i^L \\ M_i^L \end{Bmatrix} \tag{4.5}$$

or

$$\left\{S_i^{'}\right\} = \left[T_i^{'}\right]\left\{S_i^L\right\} \tag{4.6}$$

The matrix $[T_i^{'}]$ is the transfer matrix of the disc for the i^{th} station. As depicted in figure 4.3, the boundary conditions on the right side of the disc given by equation (4.5) will now be used for the left side of the beam element.

The governing differential equations for the massless elastic beam element depicted in figure 4.3 can be stated as:

$$\frac{dW}{dx} = \theta + \frac{V}{GAK_s} \tag{4.7}$$

$$\frac{d\theta}{dx} = \frac{M}{EI} \tag{4.8}$$

$$\frac{dM}{dx} = -V \tag{4.9}$$

$$\frac{dV}{dx} = -P_y \tag{4.10}$$

Equations (4.9) and (4.10) are derived using the requirement for equilibrium, and equations (4.7) and (4.8) are attributed to Timoshenko beam theory where bending and shear deformation are accounted for. The shear coefficient K_s in equation (4.7) accounts for the non-uniform distribution of shearing stress in the beam cross section. For a cylindrical cross section, with an outer diameter *a* and inner diameter *b*, the most widely accepted equation is given as:

$$K_s = \frac{6(1+\upsilon)\left(1+\frac{b}{a}\right)^2}{(7+6\upsilon)\left(1+\frac{b}{a}\right)^2 + (20+12\upsilon)\left(\frac{b}{a}\right)^2} \tag{4.11}$$

Equations (4.7)-(4.10) are solved for the homogeneous case (free vibration), in which all external force terms are set to zero, yielding:

$$\begin{Bmatrix} W_{i+1}^L \\ \theta_{i+1}^L \\ V_{i+1}^L \\ M_i^L \end{Bmatrix} = \begin{bmatrix} 1 & L_i & \frac{L_i}{G_i A_i K_{s_i}} - \frac{L_i^3}{6E_i I_i} & \frac{L_i^2}{2E_i I_i} \\ 0 & 1 & \frac{-L^2}{2E_i I_i} & \frac{L_i}{E_i I_i} \\ 0 & 0 & 1 & 0 \\ 0 & 0 & -L_i & 1 \end{bmatrix} \begin{Bmatrix} W_i' \\ \theta_i' \\ V_i' \\ M_i' \end{Bmatrix} \tag{4.12}$$

or

$$\left\{S_{i+1}^L\right\} = \left[T_i''\right]\left\{S_i'\right\} \tag{4.13}$$

where the matrix, [T_i"], is the transfer matrix for the beam element of the ith station. To obtain the transfer matrix [T_i] for the entire station, equations (4.6) and (4.13) are combined such that:

$$S_{i+1}^L = \left[T_i''\right]\left[T_i'\right]\left\{S_i^L\right\} = [T_i]\left\{S_i^L\right\} \tag{4.14}$$

where

$$[T_i]=\begin{bmatrix} 1+\left(\frac{L_i}{G_iA_iK_{si}}-\frac{L_i^3}{6E_iI_i}\right)\left(K_i-m_i\omega^2\right) & L_i+\frac{L_i^2\omega^2}{2E_iI_i}\left(I_{pi}-I_{ti}\right) & \frac{L_i}{G_iA_iK_{si}}-\frac{L_i^3}{6E_iI_i} & \frac{L_i^2}{2E_iI_i} \\ \frac{-L_i^2}{2E_iI_i}\left(K_i-m_i\omega^2\right) & 1+\frac{L_i\omega^2}{E_iI_i}\left(I_{pi}-I_{ti}\right) & \frac{-L_i^2}{2E_iI_i} & \frac{L_i}{E_iI_i} \\ K_i-m_i\omega_i^2 & 0 & 1 & 0 \\ -L_i\left(K_i-m_i\omega_i^2\right) & \omega^2\left(I_{pi}-I_{ti}\right) & -L_i & 1 \end{bmatrix} \tag{4.15}$$

If the rotor is divided into n stations, a single transfer matrix [T] that maps the left-hand side state of the rotor onto its right-hand side is obtained by noting:

$$\begin{Bmatrix} W_n^R \\ \theta_n^R \\ V_n^R \\ M_n^R \end{Bmatrix}=\begin{bmatrix} T_{11}(\omega) & T_{12}(\omega) & T_{13}(\omega) & T_{14}(\omega) \\ T_{21}(\omega) & T_{22}(\omega) & T_{23}(\omega) & T_{24}(\omega) \\ T_{31}(\omega) & T_{32}(\omega) & T_{33}(\omega) & T_{34}(\omega) \\ T_{41}(\omega) & T_{42}(\omega) & T_{43}(\omega) & T_{44}(\omega) \end{bmatrix}\begin{Bmatrix} W_1^L \\ \theta_1^L \\ V_1^L \\ M_1^L \end{Bmatrix} \tag{4.16}$$

or

$$\left\{S_n^R\right\}=[T]\left\{S_1^L\right\} \tag{4.17}$$

where

$$[T]=\left[T_n^{'}\right][T_{n-1}][T_{n-1}]\cdots[T_2][T_1] \tag{4.18}$$

The natural frequencies of the system are those frequencies that make the boundary conditions imposed on equation (4.16) true. The rotor to be modeled is free at both ends which yields the boundary conditions as:

$$V_n^R=V_1^L=0 \tag{4.19}$$

$$M_n^R=M_1^L=0 \tag{4.20}$$

Substitution of equations (4.19) and (4.20) into (4.16) yields:

$$\begin{Bmatrix} 0 \\ 0 \end{Bmatrix}=\begin{bmatrix} T_{31}(\omega) & T_{32}(\omega) \\ T_{41}(\omega) & T_{42}(\omega) \end{bmatrix}\begin{Bmatrix} W_1^L \\ \theta_1^L \end{Bmatrix} \tag{4.21}$$

where nontrivial solutions for W_1^L and θ_1^L exist only if the determinant of the coefficient matrix in equation (4.21) is zero. The frequencies that yield solutions to equation (4.21) are natural frequencies of the rotor and can be substituted back into equations (4.14) and (4.21) to obtain the mode shapes of the rotor. The algorithm for implementing the transfer matrix using a computer program is depicted in figure 4.4.

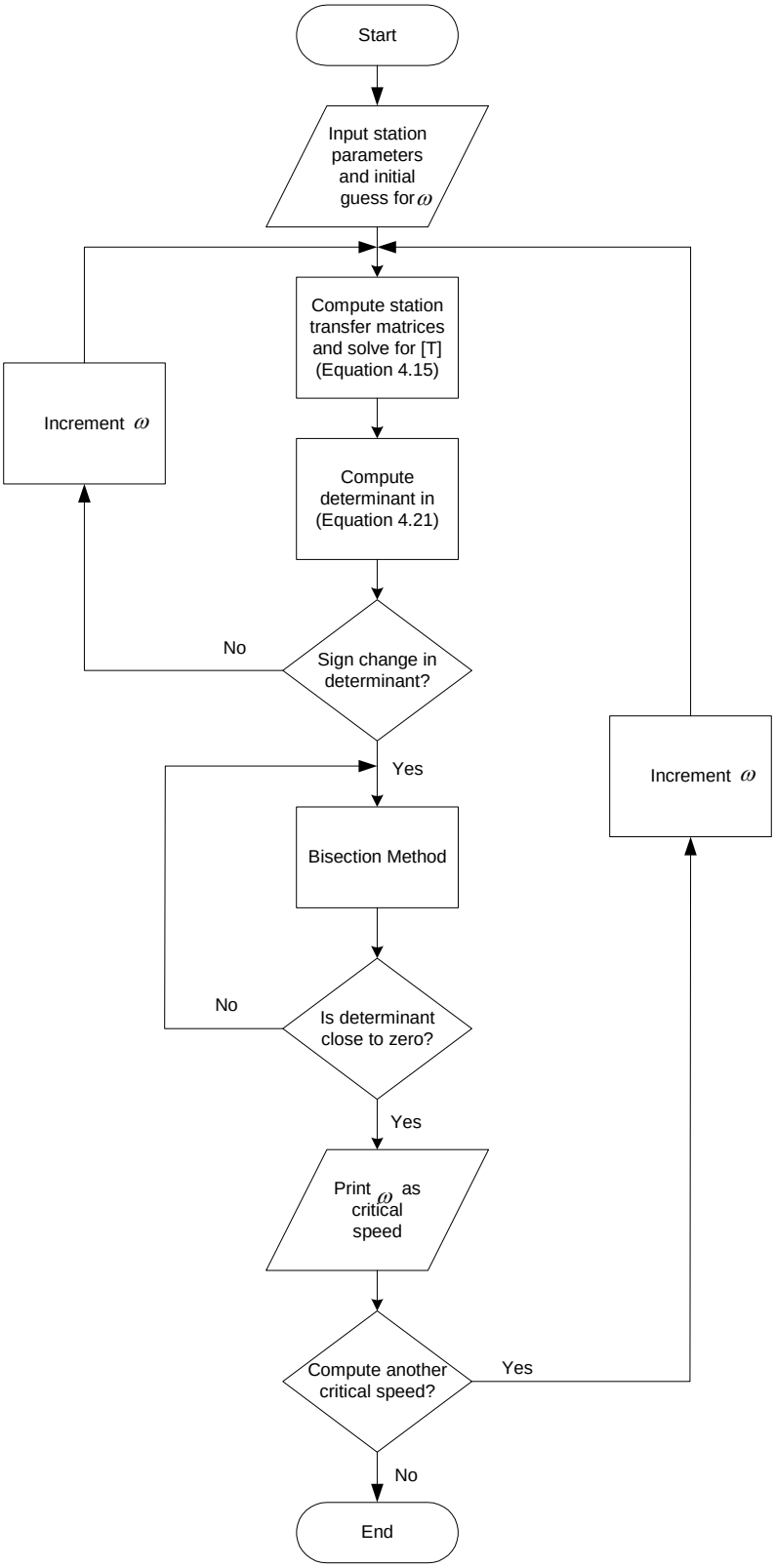

Figure 4.4: Transfer Matrix Program Flowchart

4.3 Transfer Matrix Modeling Assumptions

The transfer matrix method described in the previous section will be used to calculate the free-free modes of the PLM rotor depicted in figure 2.5. The rotor consists of a composite flywheel, catcher bearing surfaces, magnetic bearing rotor laminations, and motor magnet that are all assembled onto a one piece machined rotor hub. The items assembled onto the rotor hub contribute appreciable mass and stiffness that affect the bending modes to be calculated. While the mass of the assembled components is easily incorporated in the analysis, the additional stiffness can be difficult to predict or unknown at the present. The following set of conservative assumptions will be used for the transfer matrix rotor model:

1) The composite flywheel is pressed onto the rotor hub which contributes a stiffness that is unknown and will be neglected to provide a conservative analysis.
2) The rotor laminations are assembled using Loctite 620 retaining compound and will be considered only as an added mass in the analysis.
3) The catcher bearing surfaces are assembled via shrink fit and will be considered integral with the rotor hub.

The motor magnet is assembled using 3M DP-460 epoxy compound. Initial calculations neglecting any stiffness contributed by the magnet yielded bending modes far too low. An inquiry to the motor manufacturer suggested significant contributions to stiffness of a rotor when the magnet is assembled with the epoxy compound. However, no data was available so an experiment was setup.

4.4 Experimental Stiffness Measurements

Figure 4.5 depicts the experimental setup to determine stiffness contributed to the PLM rotor by assembly of the motor magnet. A calibrated force gauge is used to deflect the cantilevered rod while a dial indicator allows measurement of the resulting deflection. The goal of the testing is to obtain an equivalent shaft diameter based on the improved stiffness provided by the assembly of the magnet. Stiffness measurements are conducted for three cases: Rod, rod + magnet, rod + magnet + glue. The collected data is depicted

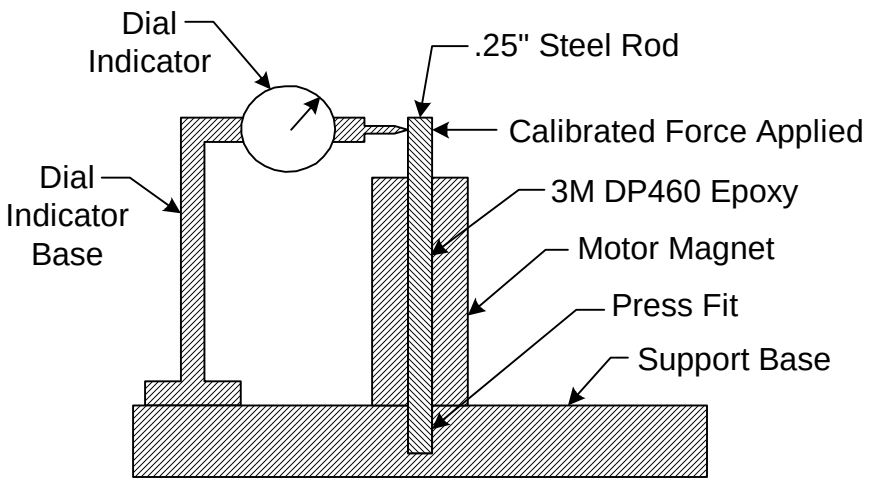

Figure 4.5: Experimental Setup for Motor Magnet Stiffness Measurement

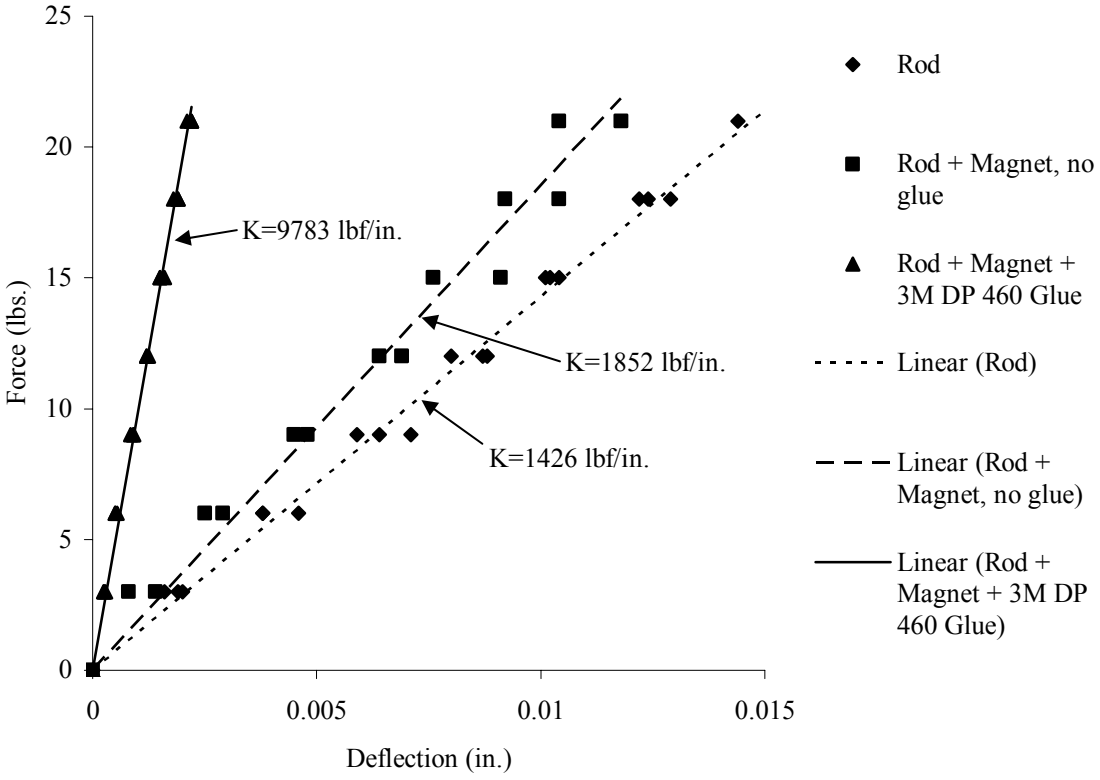

Figure 4.6: Force vs. Displacement Measurement for Motor Magnet Assembly

in figure 4.6 where the stiffness for each case is calculated as the slope of the linear regression curve fit.

As suggested by the manufacturer, the assembly of the magnet and rod with epoxy provided a very significant 686% increase in the measured stiffness. With this in mind, an equivalent shaft diameter can be calculated based on the improved stiffness and input into the transfer matrix program. This is done by noting the formula for the deflection of the cantilevered rod in the experimental setup and solving for stiffness as [11]:

$$K = \frac{F}{y_a} = \frac{6E\pi r^4}{(8l^3 - 12l^2a + 4a^3)} \tag{4.22}$$

where the variable a describes the location of the applied force, E is Youngs modulus, y_a is the measured deflection, r is the rod diameter, and l is the cantilevered length of the rod. Titanium was later selected as the rotor material which, although known for its strength and durability, only has half the stiffness of steel. To account for this using the present data, the contribution to stiffness by the epoxied magnet is added to a theoretical stiffness of a titanium rod. Assuming a superposition of stiffness contributions, the stiffness contributed by the epoxied magnet is given as:

$$K_{magnet+glue} = K_{total} - K_{steel\ rod} \tag{4.23}$$

where $K_{steel\ rod}$ is the experimentally measured stiffness for the .25" steel rod and K_{total} is the experimental stiffness for the total assembly of the epoxied magnet and rod. Rearranging equation (4.22) we can solve for an equivalent titanium shaft diameter as:

$$d_{eq} = 2\left[\left(K_{Ti\ rod} + K_{magnet+glue}\right)\frac{(8l^3 - 12l^2a + 4a^3)}{6E_{Ti}\pi}\right]^{\frac{1}{4}} \tag{4.24}$$

where the stiffness of a titanium rod, K_{Ti}, is calculated from equation (4.22) using published values of Young's modulus for titanium, E_{Ti}. The result shows that the stiffness of a titanium shaft .44 inches in diameter is equivalent to the physical assembly of the .25 inch titanium rod and magnet. Table 4.1 provides a summary of all the experimental and theoretical stiffness values. The magnet will still be modeled as an added mass in the transfer matrix code. However, the shaft elements will be modeled with a .44 vs. .25 inch diameter to account for the added stiffness.

Table 4.1: Stiffness Values for Motor Magnet Assembly

Description	K, Experimental (lbf/in.)	K, Theoretical (lbf/in.)
.25” Steel Rod	1426 ($K_{steel\ rod}$)	1593
.25” Steel Rod + Magnet + Glue	9783 (K_{total})	-
.394” Steel Rod	-	9783
.25” Titanium Rod	-	939 (K_{Ti})
.25” Titanium Rod +Magnet +Glue	-	9296
.44” (d_{eq}) Titanium Rod	-	9296

4.5 Flexible Rotor Critical Speeds

The transfer matrix described in section 4.2 is implemented using Matlab software. Figure 4.7 depicts the transfer matrix rotor model based on the rotor geometry and modeling assumptions stated in sections 4.3 and 4.4. The shaft elements are modeled using the published properties for Titanium 6AL-4V. The flywheel, rotor laminations, and motor magnet are modeled as added masses with densities of .06, .293, and .275 lb/in^3 respectively.

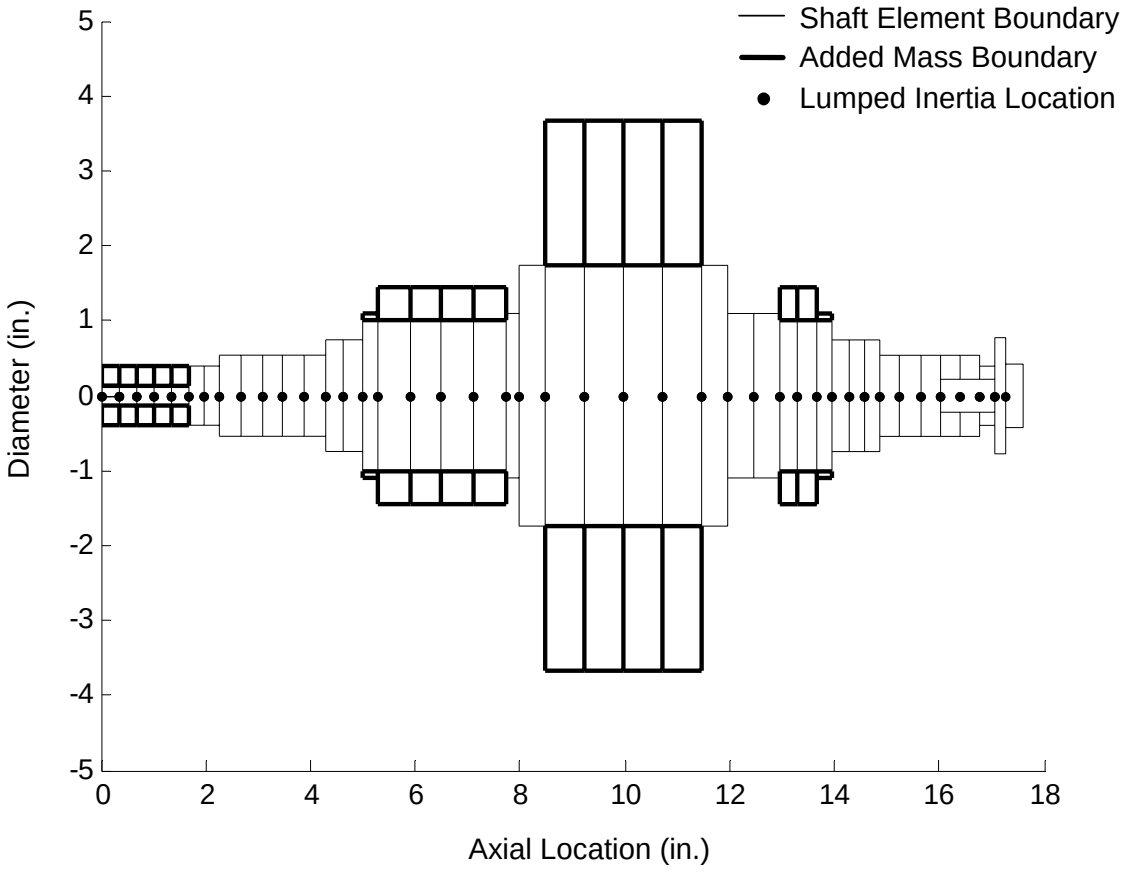

Figure 4.7: Transfer Matrix Model of PLM Rotor

Prediction of the PLM rotor bending modes is important to ensure that the rotor response due to these modes does not prevent operation to 50,000 Rpm or mask the unbalance response due to the PLM change in mass eccentricity. Typically, bending modes above 120% of the maximum operating speed are expected to contribute little to the rotor response during operation. The first two bending modes of the PLM rotor are depicted in figure 4.8. The first bending mode at 60,679 Rpm is driven primarily by the rotor flexibility in the motor magnet location. Damping this mode would be difficult since there is very little motion at the bearings. However, the mode is at a sufficiently high speed corresponding to 121% of the maximum operating speed. The second mode at 131,040 Rpm is well above the operating speed range and expected to provide little contribution to the rotor response.

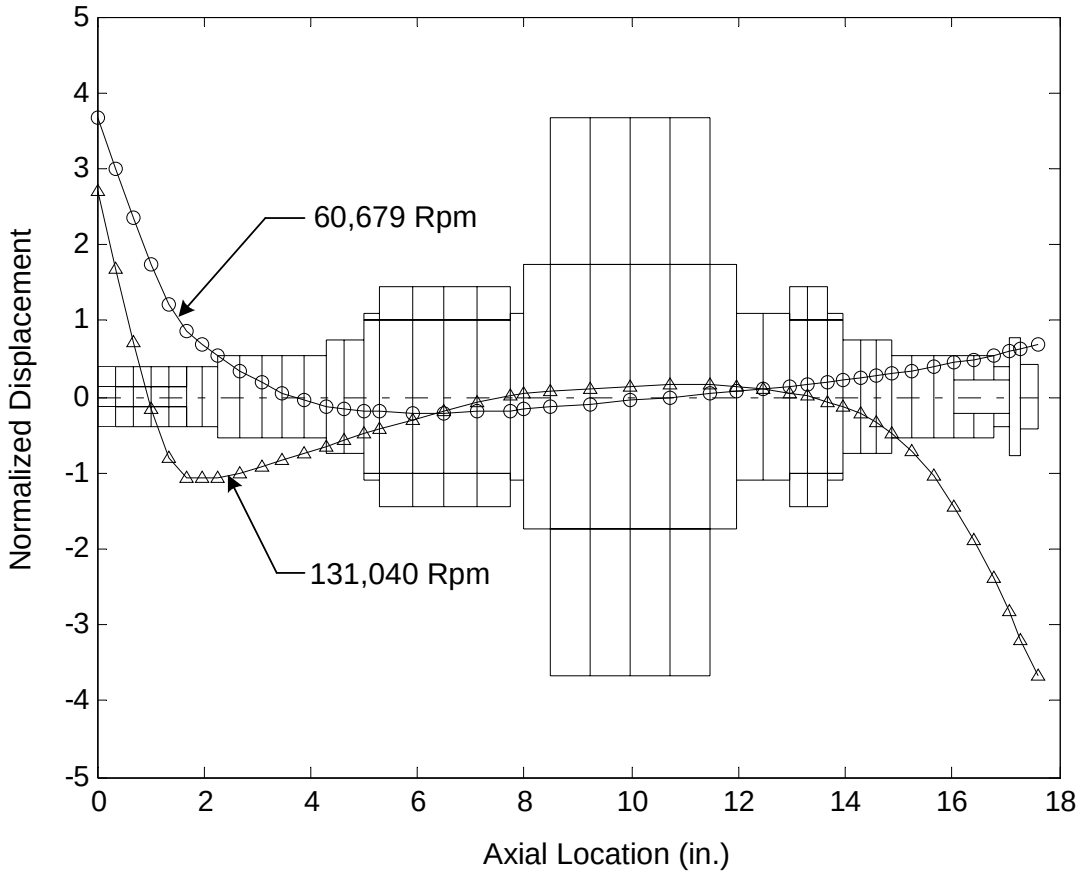

Figure 4.8: PLM Rotor Bending Modes

CHAPTER V

CONCLUSIONS AND RECOMMENDATIONS

The objectives set forth in chapter I included developing a test rig concept, a numerical simulation of the rotor-bearing system to ensure feasible detection of the PLM flywheel change in mass eccentricity, and finally a rotordynamics analysis to ensure operation to the maximum operating speed of 50,000 Rpm. This section will discuss each objective and the conclusions of this research. A summary of the conclusions are as follows:

- The final PLM test rig design presented meets all performance requirements and feasible detection of the PLM flywheel change in mass eccentricity is confirmed via analytical study.
- Detection of the PLM flywheel change in mass eccentricity is feasible with and without a notch filter utilizing the magnetic suspension feedback sensors (Rotor position measurement).
- Measurement of magnetic bearing currents is desired for detection when operating without a notch filter due to a higher signal to noise ratio.
- PLM rotor rigid body modes at 7,127 and 12,056 Rpm can be traversed with the aid of damping from the magnetic bearings.
- PLM rotor first bending mode will not provide a significant contribution to the rotor response in the operating speed range of 20,000 to 50,000 Rpm.

A top-down systems engineering approach was used to develop the final test rig design presented in chapter II. The rotor mass and interfaces with the motor were identified as critical parameters to consider in the conceptual design phase. Consideration of these parameters and successful fulfillment of the identified requirements resulted in the final design. This design consists of a titanium rotor hub, a pair of magnetic bearings for rotor support, a brushless DC motor to provide torque, and angular contact bearings that provide an auxiliary suspension. This design was carried out to a high level of detail described by fabrication drawings included in Appendix A.

A state space model of the rotor bearing system was created and solved numerically to determine whether detection of the PLM flywheel change in mass eccentricity was feasible. Results are discussed for operation with and without a notch filter. For the case without a notch, the magnetic bearing currents increase several amps in magnitude when comparing response with and without the PLM mass eccentricity. These currents are expected to provide a better signal to noise ratio than the position sensors. However, it is recommended to use the feedback displacement sensors for detection when operating with a notch since the magnetic bearing currents are attenuated. In all cases it is recommended that the shaft runout be kept below .0005 inches to ensure a positive increase in amplitude vs. the PLM mass eccentricity change.

Finally, rotordyamic considerations are addressed in chapter IV to ensure operation up to the maximum operating speed of 50,000 Rpm. Stable levitation of the rotor is accomplished throughout the rpm range as evidenced by the steady state response plots in chapter III. Two rigid body critical speeds are identified at 7,127 and 12,056 Rpm. The magnetic bearings are able to provide sufficient damping to traverse these speeds while staying within operating limits that are set by current saturation in the power amplifier model. In addition, a transfer matrix analysis was conducted that revealed the first rotor bending mode was 121% above the maximum operating speed. This prediction was based on experimental measurements made to better model rotor stiffness properties. The bending modes are expected to provide neglible contributions to the rotor response since they are well above the operating speed range.

Future work will include fabrication of the test rig based on the drawings in Appendix A. An accurate correlation between experimental and predicted mass eccentricities will be important. In actual applications the preload loss should initially occur just above the maximum operating speed such as 60,000 Rpm. In addition, extensive test runs could be completed to show that the preload loss will occur at lower speeds as the flywheel material degrades. Ultimately, the information regarding the preload loss characteristics will be programmed into the motor / generator controller of a flywheel energy storage unit. This will allow a “virtual containment” scheme in which the flywheel maximum operating speed is de-rated or shut down when a preload loss event is detected.

REFERENCES

1. C. Fisher and G. Lesieutre 1999 *International SAMPE Symposium and Exhibition,* 2145-2154. Health Monitoring of High Energy Density Rotor for Use in Spacecraft Applications.

2. F. Shiue, G. Lesieute, and C. Bakis 2001 *AIAA/ASME/ASCE/AHS/ASC Structures Structural Dynamics and Materials Conference*, 1927-1936. Condition Monitoring and Virtual Containment for Composite Flywheels.

3. F. Shiue, G. Lesieute, and C. Bakis 2002 *Journal of Composite Materials* **36**, 1103-1120. A Virtual Containment Strategy for Filament-Wound Composite Flywheel Rotors with Damage Growth.

4. T. Lalk 2000 *Class Notes for MEEN 446*. College Station: Texas A&M University, Department of Mechanical Engineering.

5. H. Sonnichsen 1993 *Mechanical Engineering* **115**, 72-77. Ensuring Spin Test Safety.

6. G. Sun 2003 *Ph.D. Dissertation*. A High Fidelity Ball Bearing and Damper Model Including Thermal Effects for Magnetic Suspension Auxiliary Service and Blade Loss Simulation. College Station: Texas A&M University

7. A. Lee, F. Hsiao, and D. Ko 1994 *JSME International Journal* **37**, 774-782. Analysis and Testing of Magnetic Bearings with Permanent Magnets for Bias.

8. 1986 *International Standard 1940/1*. Mechanical Vibration-Balance Quality Requirements of Rigid Rotors – Part 1: Determination of Permissible Residual Unbalance.

9. J. M. Vance 1988 *Rotordynamics of Turbomachinery*. New York: John Wiley and Sons.

10. A. Palazzolo 1989 *Class Notes for MEEN 639*. College Station: Texas A&M University, Department of Mechanical Engineering

11. W. C. Young 1989 *Roark's Formulas for Stress and Strain*. New York: McGraw-Hill.

APPENDIX A

FABRICATION DRAWINGS

ITEM NO.	QTY.	PART NO.	DESCRIPTION
1	1	PLM002	ASS'Y, ROTOR, COMPLETE
2	1	CB001	ASS'Y, Mag Brg, Combo
3	1	RB001	ASS'Y, Mag Brg, Radial
4	1	PLM012	HOUSING, MAIN
5	1	PLM013	HOUSING, COMBO BRG
6	1	PLM014	HOUSING, RADIAL BRG
7	2	PLM003	ASS'Y, RADIAL SENSORS, COMBO & RADIAL
8	1	PLM005	ASS'Y, CATCHER BRGS & MOTOR, RADIAL END
9	1	PLM004	ASS'Y, CATCHER BRGS, COMBO END
10	1	NA	SHIM, 0.010 - 0.030 THICK
11	38	NA	1/4" SPLIT LOCKWASHER
12	26	NA	1/4-20 X 1.0 LG. SOCKET HEAD CAP SCREW
13	12	NA	1/4-20 X 2.25 LG. SOCKET HEAD CAP SCREW
15	8	NA	#8-32 X .5 LG. SOCKET HEAD CAP SCREW
16	8	NA	#8 SPLIT LOCKWASHER
17	1	PLM024	MOUNT, AXIAL SENSOR
18	1	NA	BENTLY NEVADA 330171-00-08-10-02-00
19	1	NA	1/4-28 HEX NUT

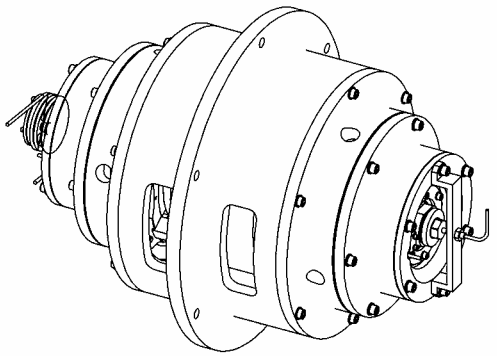

COLLAPSED VIEW
SCALE 1:2

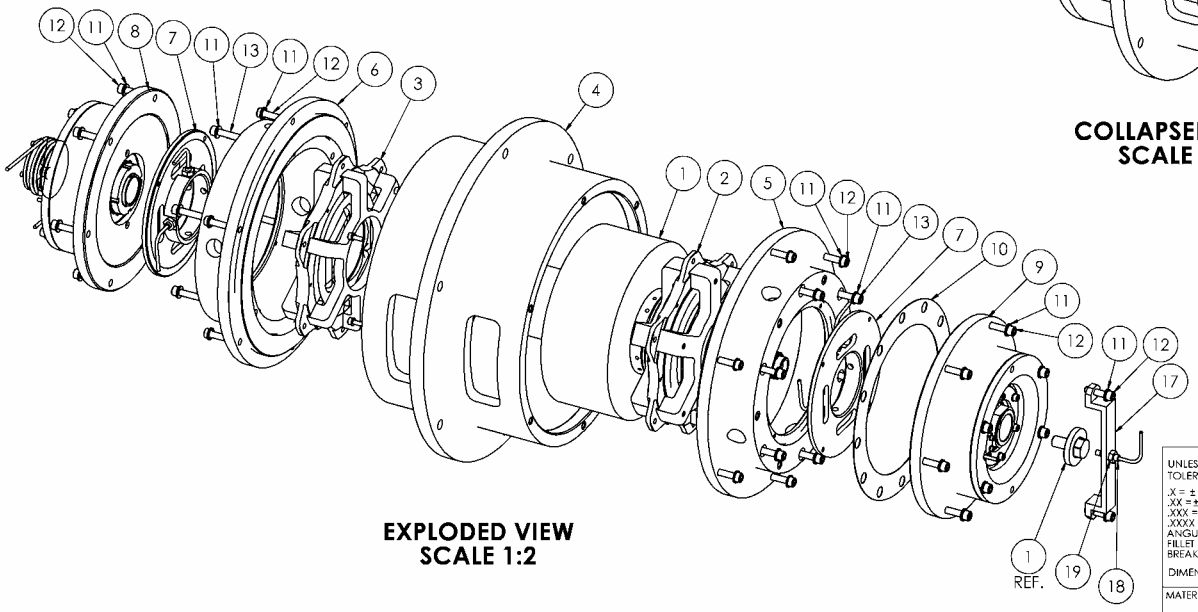

EXPLODED VIEW
SCALE 1:2

UNLESS OTHERWISE SPECIFIED TOLERANCES ARE: .X = ± .030 .XX = ± .010 .XXX = ± .005 .XXXX = ± .0005 ANGULAR = ± .5° FILLET RADIUS .035 MAX BREAK CORNERS .005 - .015 DIMENSIONS ARE IN INCHES	DIMENSIONING AND TOLERANCING PER ASME Y14.5M-1994	TAMU VIBRATION CONTROL & ELECTROMECHANICS LABRATORY
	APPROVALS / DATE	ASS'Y, PLM TEST RIG
	DRAWN J. PREUSS / DATE MAY 2003	
MATERIAL	CHECKED / DATE	SIZE D · DWG. NO. PLM001 · REV.
FINISH OR BETTER		SCALE 1:1 · CAD FILE: · SHEET 1 OF 3

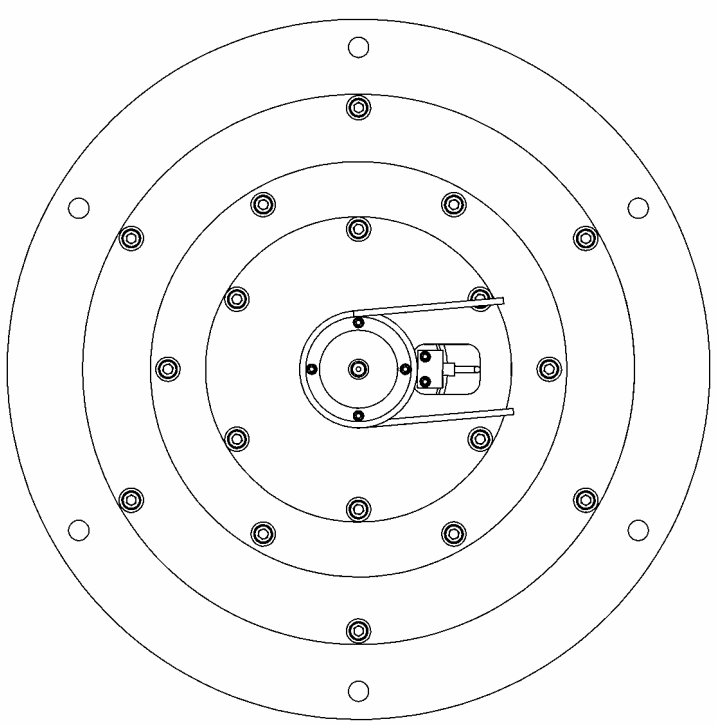

VIEW FROM RADIAL END

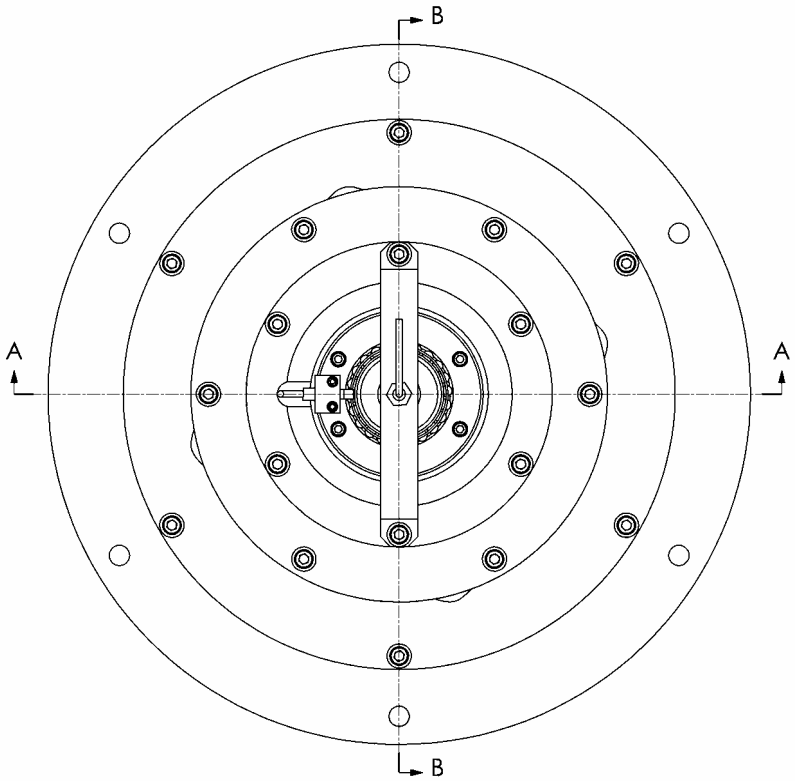

VIEW FROM COMBO END

UNLESS OTHERWISE SPECIFIED TOLERANCES ARE: .X = ± .030 .XX = ± .010 .XXX = ± .005 .XXXX = ± .0005 ANGULAR = ± .5° FILLET RADIUS .035 MAX BREAK CORNERS .005 - .015 DIMENSIONS ARE IN INCHES	DIMENSIONING AND TOLERANCING PER ASME Y14.5M-1994	TAMU	VIBRATION CONTROL & ELECTROMECHANICS LABRATORY
	APPROVALS / DATE		ASS'Y, PLM TEST RIG
	DRAWN: J. PREUSS / DATE: MAY 2003		
MATERIAL	CHECKED / DATE	SIZE: D	DWG. NO.: PLM001 / REV.
FINISH OR BETTER		SCALE: 1:1	CAD FILE: / SHEET: 2 OF 3

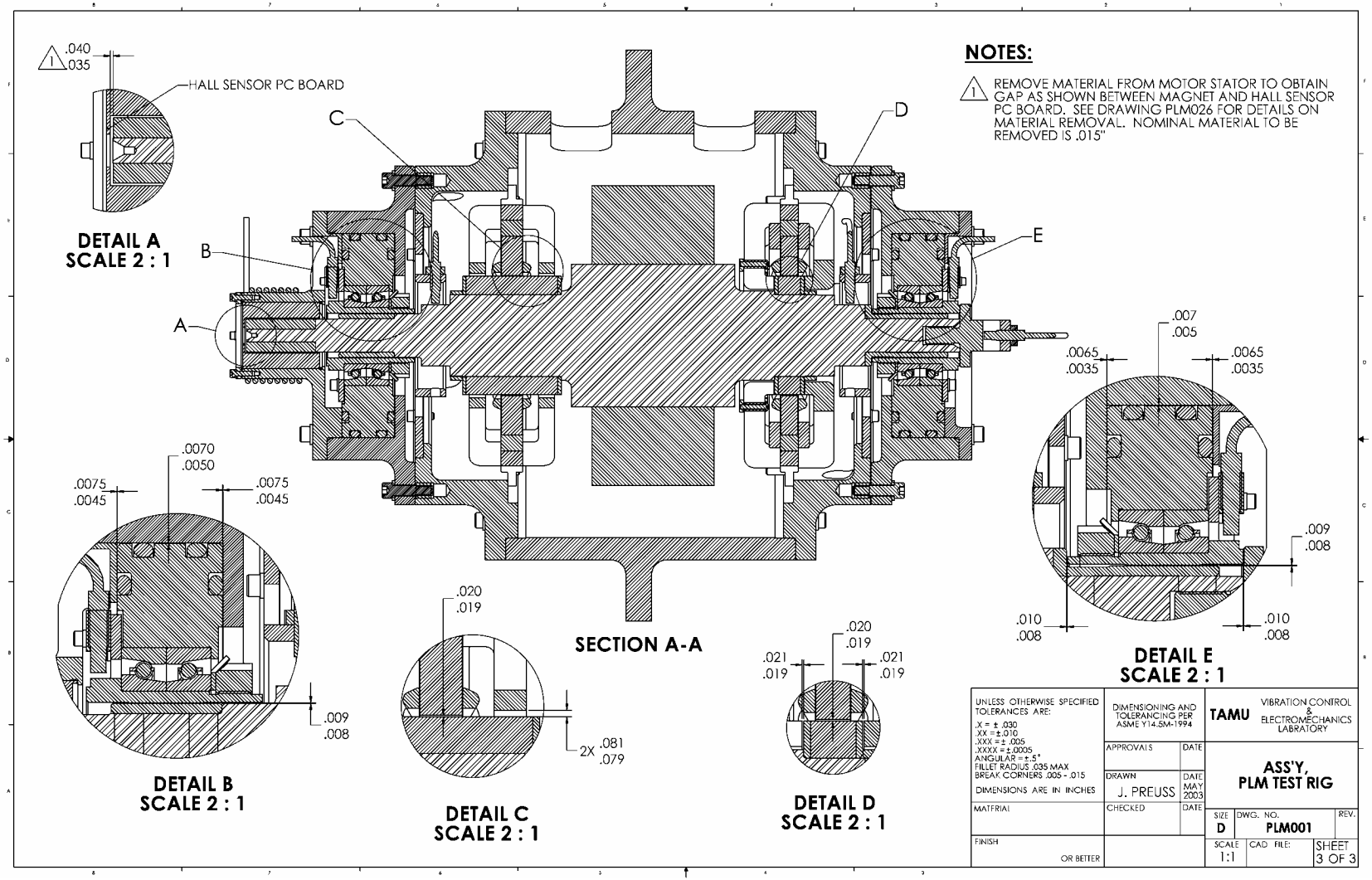
NOTES:
1 REMOVE MATERIAL FROM MOTOR STATOR TO OBTAIN GAP AS SHOWN BETWEEN MAGNET AND HALL SENSOR PC BOARD. SEE DRAWING PLM026 FOR DETAILS ON MATERIAL REMOVAL. NOMINAL MATERIAL TO BE REMOVED IS .015"
1 .040 .035
HALL SENSOR PC BOARD
DETAIL A SCALE 2 : 1
A
B
C
D
E
SECTION A-A
.0070 .0050
.0075 .0045
.0075 .0045
.009 .008
DETAIL B SCALE 2 : 1
.020 .019
2X .081 .079
DETAIL C SCALE 2 : 1
.020 .019
.021 .019
.021 .019
DETAIL D SCALE 2 : 1
.007 .005
.0065 .0035
.0065 .0035
.009 .008
.010 .008
.010 .008
DETAIL E SCALE 2 : 1
UNLESS OTHERWISE SPECIFIED TOLERANCES ARE:
.X = ± .030
.XX = ±.010
.XXX = ± .005
.XXXX = ±.0005
ANGULAR = ± .5°
FILLET RADIUS .035 MAX
BREAK CORNERS .005 - .015
DIMENSIONS ARE IN INCHES
MATERIAL
FINISH
OR BETTER
DIMENSIONING AND TOLERANCING PER ASME Y14.5M-1994
APPROVALS
DATE
DRAWN
J. PREUSS
DATE MAY 2003
CHECKED
DATE
TAMU
VIBRATION CONTROL & ELECTROMECHANICS LABRATORY
ASS'Y, PLM TEST RIG
SIZE D
DWG. NO. PLM001
REV.
SCALE 1:1
CAD FILE:
SHEET 3 OF 3

ITEM NO.	QTY.	PART NO.	DESCRIPTION
1	1	PLM011	ASS'Y, ROTOR, GRIND
	1	PLM006	ROTOR HUB
	1	PLM007	CATCHER SURFACE, ROTOR, COMBO BRG END
	1	PLM008	CATCHER SURFACE, ROTOR, RADIAL BRG END
	1	CB006	ASS'Y, ROTOR LAMINATIONS, COMBO BRG
	1	CB004	ROTOR LAMINATION, COMBO BRG
	2	CB005	END PLATE, ROTOR LAM STACK, COMBO BRG
	1	RB006	ASS'Y, Rotor Laminations, Radial Brg
	1	RB004	Rotor Lamination, Radial Brg
	2	RB005	End Plate, Rotor Lam Stack, Radial Brg
	1	PLM009	CATCHER SURFACE, AXIAL, ROTOR
	2	PLM010	RETAINER, ROTOR LAM ASS'Y, COMBO & RADIAL
	1	NA	LOCTITE 609
2	1	PLM025	PLM025 MAGNET, MODIFIED, KOFORD 1.6" BRUSHLESS DC MOTOR
3	1	NA	UTCEM PLM COMPOSITE FLYWHEEL
4	1	NA	3M DP460 EPOXY

NOTES:

1. GLUE MAGNET TO ROTOR WITH 3M SCOTCHWELD DP460. PREPARE SURFACE USING THE FOLLOWING STEPS:
   - WIPE SURFACE WITH ISOPROPYL ALCOHOL SOAKED SWAB.
   - ABRADE WITH 3M SCOTCH-BRITE SCOURING PAD.
   - REPEAT WIPE WITH ISOPROPYL ALCOHOL SOAKED SWAB.
2. FLYWHEEL TO BE INSTALLED BY UTCEM.

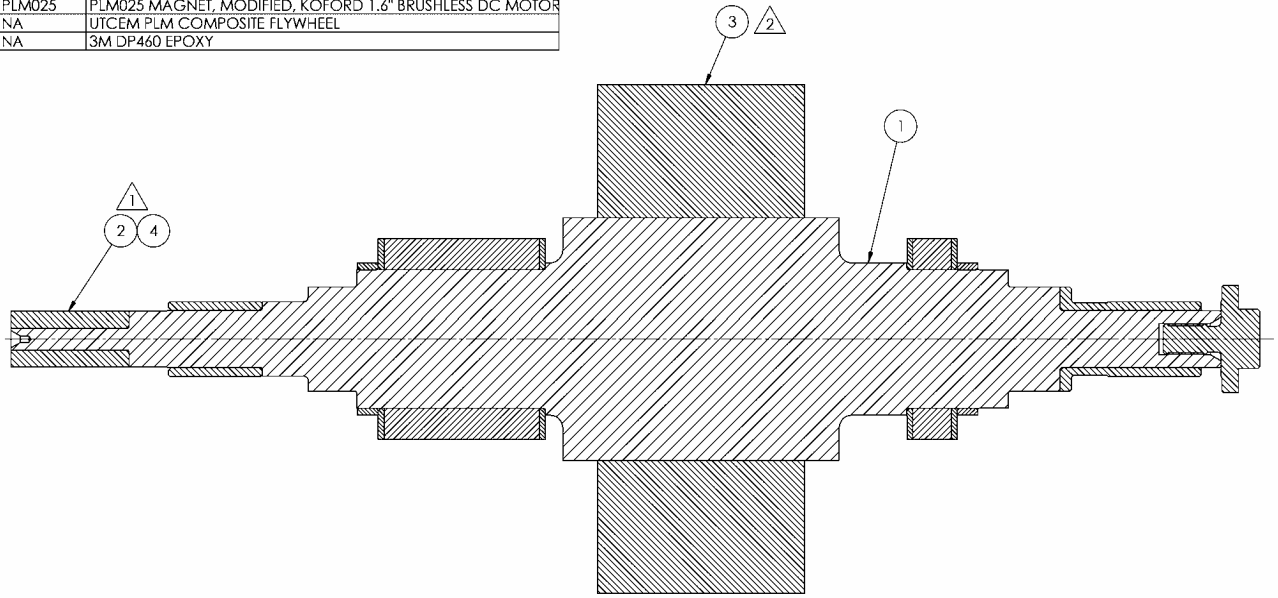

UNLESS OTHERWISE SPECIFIED TOLERANCES ARE:
.X = ± .030
.XX = ± .010
.XXX = ± .005
.XXXX = ± .0005
ANGULAR = ± .5°
FILLET RADIUS .035 MAX
BREAK CORNERS .005 - .015
DIMENSIONS ARE IN INCHES

MATERIAL

FINISH

DO NOT SCALE DRAWING

DIMENSIONING AND TOLERANCING PER ASME Y14.5M-1994

APPROVALS

DRAWN J. PREUSS DATE MAY 2003

CHECKED

TAMU VIBRATION CONTROL & ELECTROMECHANICS LABRATORY

ASS'Y, ROTOR, COMPLETE

SIZE C | DWG. NO. PLM002 | REV.

SCALE 1:1 | SHEET 1 1

ITEM NO.	QTY.	PART NO.	DESCRIPTION
1	1	PLM015	HOUSING, RADIAL SENSORS, COMBO & RADIAL
2	2	NA	BENTLY NEVADA 330171-00-08-10-02-00
3	2	NA	1/4-28 HEX NUT

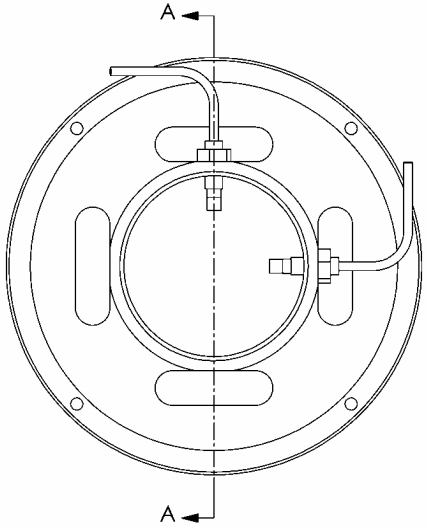

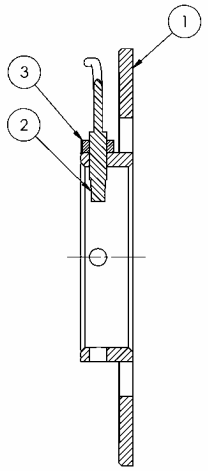

SECTION A-A

DO NOT SCALE DRAWING

UNLESS OTHERWISE SPECIFIED TOLERANCES ARE: .X = ± .030 .XX = ±.010 .XXX = ± .005 .XXXX = ±.0005 ANGULAR = ±.5° FILLET RADIUS .035 MAX BREAK CORNERS .005 - .015 DIMENSIONS ARE IN INCHES	DIMENSIONING AND TOLERANCING PER ASME Y14.5M-1994	TAMU VIBRATION CONTROL & ELECTROMECHANICS LABRATORY
	APPROVALS	ASS'Y, RADIAL SENSORS, COMBO & RADIAL
	DRAWN J. PREUSS — DATE MAY 2003	
MATERIAL	CHECKED	
FINISH OR BETTER		SIZE C — DWG. NO. PLM003 — REV.
		SCALE 1:1 — SHEET 1 1

ITEM NO.	QTY.	PART NO.	DESCRIPTION
1	2	NA	BARDEN CZSB107JSSDL ANGULAR CONTACT BEARING
2	1	PLM018	CATCHER SURFACE, STATOR, COMBO & RADIAL END
3	1	NA	W07 LOCKWASHER
4	1	NA	N07 LOCKNUT
5	1	PLM016	HOUSING, CATCHER BRGS, COMBO & RADIAL
6	2	NA	.188 DIA. X .5 LG. DOWEL PIN
7	2	NA	O-RING #2-343
8	2	NA	O-RING #2-350
9	1	PLM017	RETAINER, CATCHER BRGS, COMBO & RADIAL END
10	1	PLM019	HOUSING, CATCHER BRG HOUSING, COMBO & RADIAL END
11	6	NA	KEENSERT KN420, .250-20
12	1	PLM020	RETAINER, CATCHER BRG HOUSING, COMBO END
13	1	PLM023	MOUNT, KEYPHASOR
14	1	NA	BENTLY NEVADA 330171-00-08-10-02-00
15	4	NA	1/4" SPLIT LOCKWASHER
16	4	NA	1/4-20 X 1.0 LG. SOCKET HEAD CAP SCREW
17	6	NA	#8 SPLIT LOCKWASHER
18	6	NA	#8-32 X .5 LG. SOCKET HEAD CAP SCREW
19	2	NA	#4 SPLIT LOCKWASHER
20	2	NA	#4-40 X .438 LG. SOCKET HEAD CAP SCREW
21	1	NA	THERMAL GREASE, MCMASTER P/N 3883K22

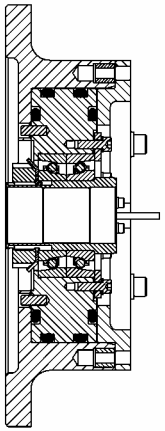

SECTION A-A

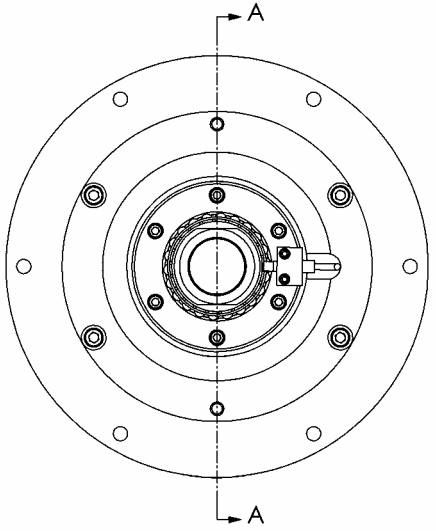

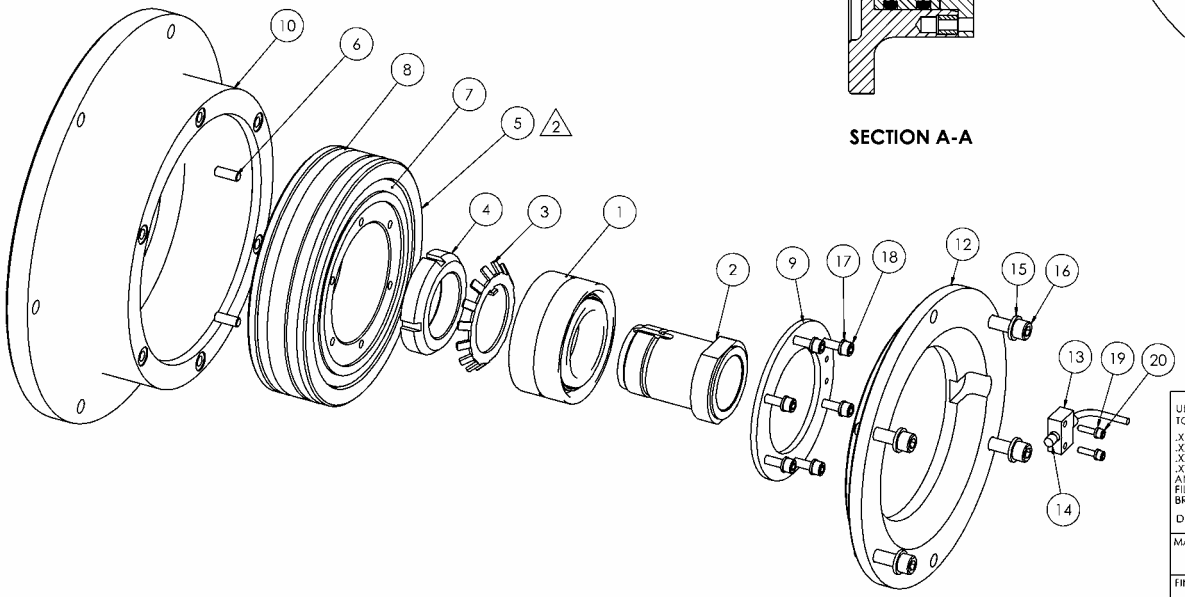

NOTES:

1. ASSEMBLY TO BE ALIGNED WITH ROTOR LEVITATED. USE 1/4" DOWEL PINS TO MAINTAIN LOCATION.

2 APPLY THERMAL GREASE TO EASE ASSEMBLY AND PROMOTE HEAT TRANSFER.

UNLESS OTHERWISE SPECIFIED TOLERANCES ARE: .X = ± .030 .XX = ± .010 .XXX = ± .005 .XXXX = ± .0005 ANGULAR = ± .5° FILLET RADIUS .035 MAX BREAK CORNERS .005 - .015 DIMENSIONS ARE IN INCHES	DIMENSIONING AND TOLERANCING PER ASME Y14.5M-1994	TAMU	VIBRATION CONTROL & ELECTROMECHANICS LABRATORY
	APPROVALS / DATE		ASS'Y, CATCHER BRG, COMBO END
	DRAWN: J. PREUSS / DATE: MAY 2003		
MATERIAL	CHECKED / DATE	SIZE: D	DWG. NO.: PLM004 / REV.
FINISH: OR BETTER		SCALE: 1:1	CAD FILE: / SHEET: 1 OF 1

ITEM NO.	QTY.	PART NO.	DESCRIPTION
1	2	NA	BARDEN CZSB107JSSDL ANGULAR CONTACT BEARING
2	1	PLM018	CATCHER SURFACE, STATOR, COMBO & RADIAL END
3	1	NA	W07 LOCKWASHER
4	1	NA	N07 LOCKNUT
5	1	PLM016	HOUSING, CATCHER BRGS, COMBO & RADIAL
6	2	NA	.188 DIA. X .5 LG. DOWEL PIN
7	2	NA	O-RING #2-343
8	2	NA	O-RING #2-350
9	1	PLM017	RETAINER, CATCHER BRGS, COMBO & RADIAL END
10	6	NA	#8 SPLIT LOCKWASHER
11	6	NA	#8-32 X .5 LG. SOCKET HEAD CAP SCREW
12	1	PLM019	HOUSING, CATCHER BRG HOUSING, COMBO & RADIAL END
13	6	NA	KEENSERT KN420, .250-20
14	1	PLM021	HOUSING, MOTOR
15	6	NA	1/4" SPLIT LOCKWASHER
16	6	NA	1/4-20 X 1.0 LG. SOCKET HEAD CAP SCREW
17	1	NA	1/8" - 3/16" O.D. COPPER TUBING
18	1	PLM026	STATOR, MODIFIED, KOFORD 1.6" BRUSHLESS DC MOTOR
19	1	PLM022	RETAINER, MOTOR
20	6	NA	#4 SPLIT LOCKWASHER
21	6	NA	#4-40 X .438 LG. SOCKET HEAD CAP SCREW
22	1	PLM023	MOUNT, KEYPHASOR
23	1	NA	BENTLY NEVADA 330171-00-08-10-02-00
24	1	NA	THERMAL GREASE, MCMASTER P/N 3883K22

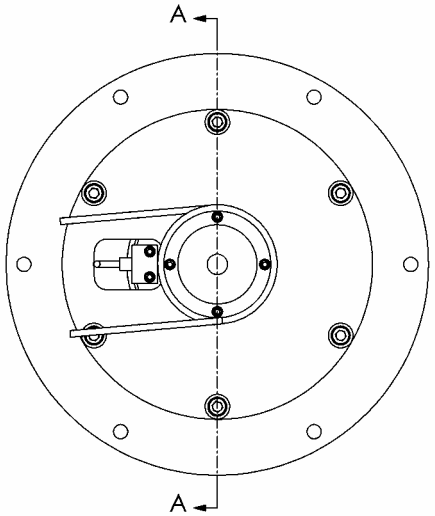

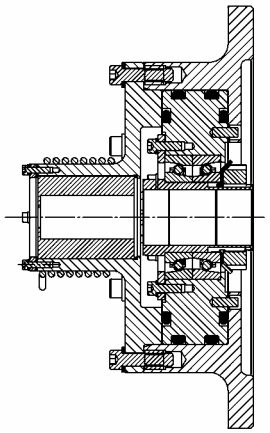

SECTION A-A

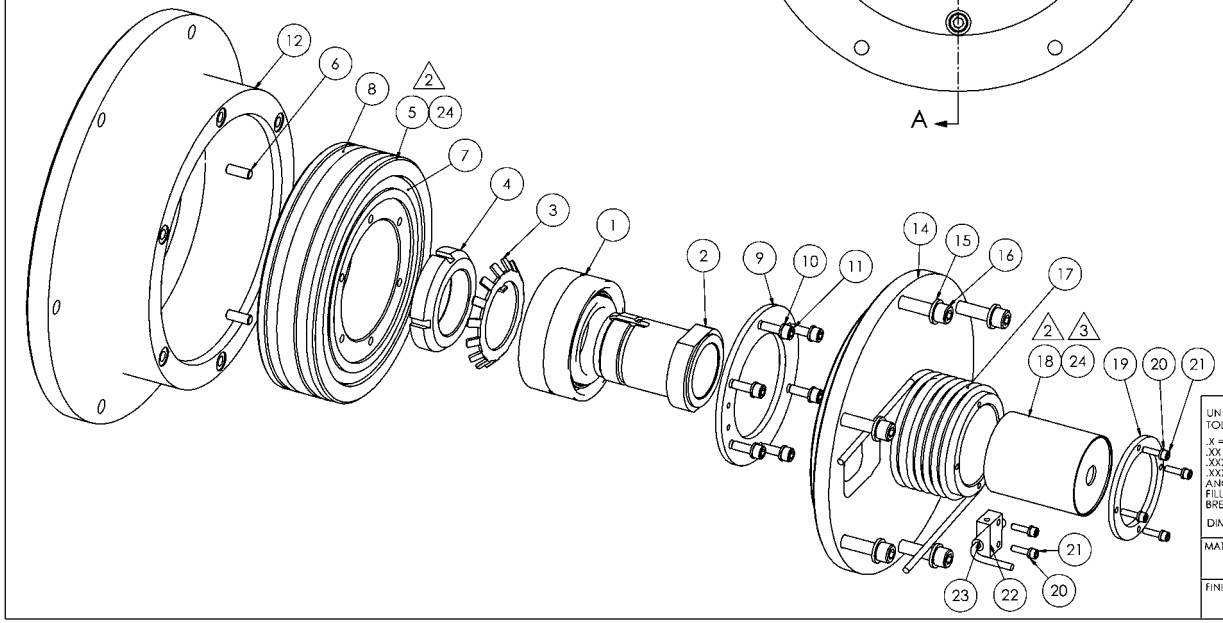

NOTES:

1. ASSEMBLY TO BE ALIGNED WITH ROTOR LEVITATED. USE 1/4" DOWEL PINS TO MAINTAIN LOCATION.
2. APPLY THERMAL GREASE TO EASE ASSEMBLY AND PROMOTE HEAT TRANSFER.
3. SEE NOTE 1 IN PLM001, PAGE 4 TO SET AXIAL AIR GAP BETWEEN MAGNET AND MOTOR HALL SENSORS.

UNLESS OTHERWISE SPECIFIED TOLERANCES ARE: .X = ± .030 .XX = ±.010 .XXX = ± .005 .XXXX = ±.0005 ANGULAR = ± .5° FILLET RADIUS .035 MAX BREAK CORNERS .005 - .015 DIMENSIONS ARE IN INCHES	DIMENSIONING AND TOLERANCING PER ASME Y14.5M-1994	TAMU	VIBRATION CONTROL & ELECTROMECHANICS LABRATORY
	APPROVALS / DATE	ASS'Y, CATCHER BRGS & MOTOR, RADIAL END	
	DRAWN: J. PREUSS / DATE: MAY 2003		
MATERIAL	CHECKED / DATE	SIZE: D	DWG. NO.: PLM005 / REV.
FINISH: OR BETTER		SCALE: 1:1	SHEET: 1 OF 1

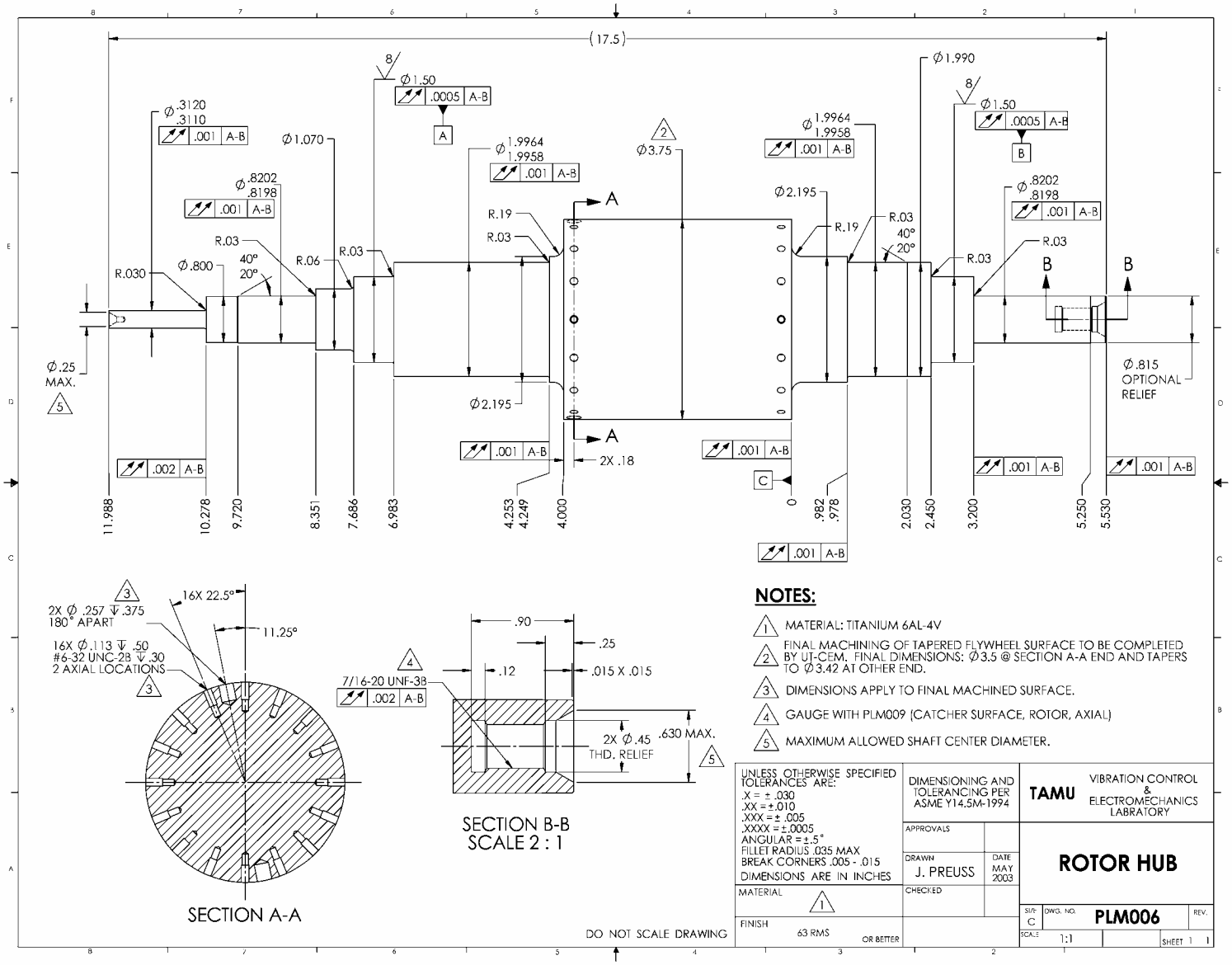

NOTES:

1. MATERIAL: TITANIUM 6AL-4V
2. FINAL MACHINING OF TAPERED FLYWHEEL SURFACE TO BE COMPLETED BY UT-CEM. FINAL DIMENSIONS: Ø3.5 @ SECTION A-A END AND TAPERS TO Ø3.42 AT OTHER END.
3. DIMENSIONS APPLY TO FINAL MACHINED SURFACE.
4. GAUGE WITH PLM009 (CATCHER SURFACE, ROTOR, AXIAL)
5. MAXIMUM ALLOWED SHAFT CENTER DIAMETER.

UNLESS OTHERWISE SPECIFIED TOLERANCES ARE: .X = ± .030 .XX = ± .010 .XXX = ± .005 .XXXX = ± .0005 ANGULAR = ± .5° FILLET RADIUS .035 MAX BREAK CORNERS .005 - .015 DIMENSIONS ARE IN INCHES	DIMENSIONING AND TOLERANCING PER ASME Y14.5M-1994	TAMU VIBRATION CONTROL & ELECTROMECHANICS LABRATORY
	APPROVALS	ROTOR HUB
	DRAWN J. PREUSS DATE MAY 2003	
MATERIAL 1	CHECKED	
FINISH 63 RMS OR BETTER		SIZE C DWG. NO. PLM006 REV.
DO NOT SCALE DRAWING		SCALE 1:1 SHEET 1 1

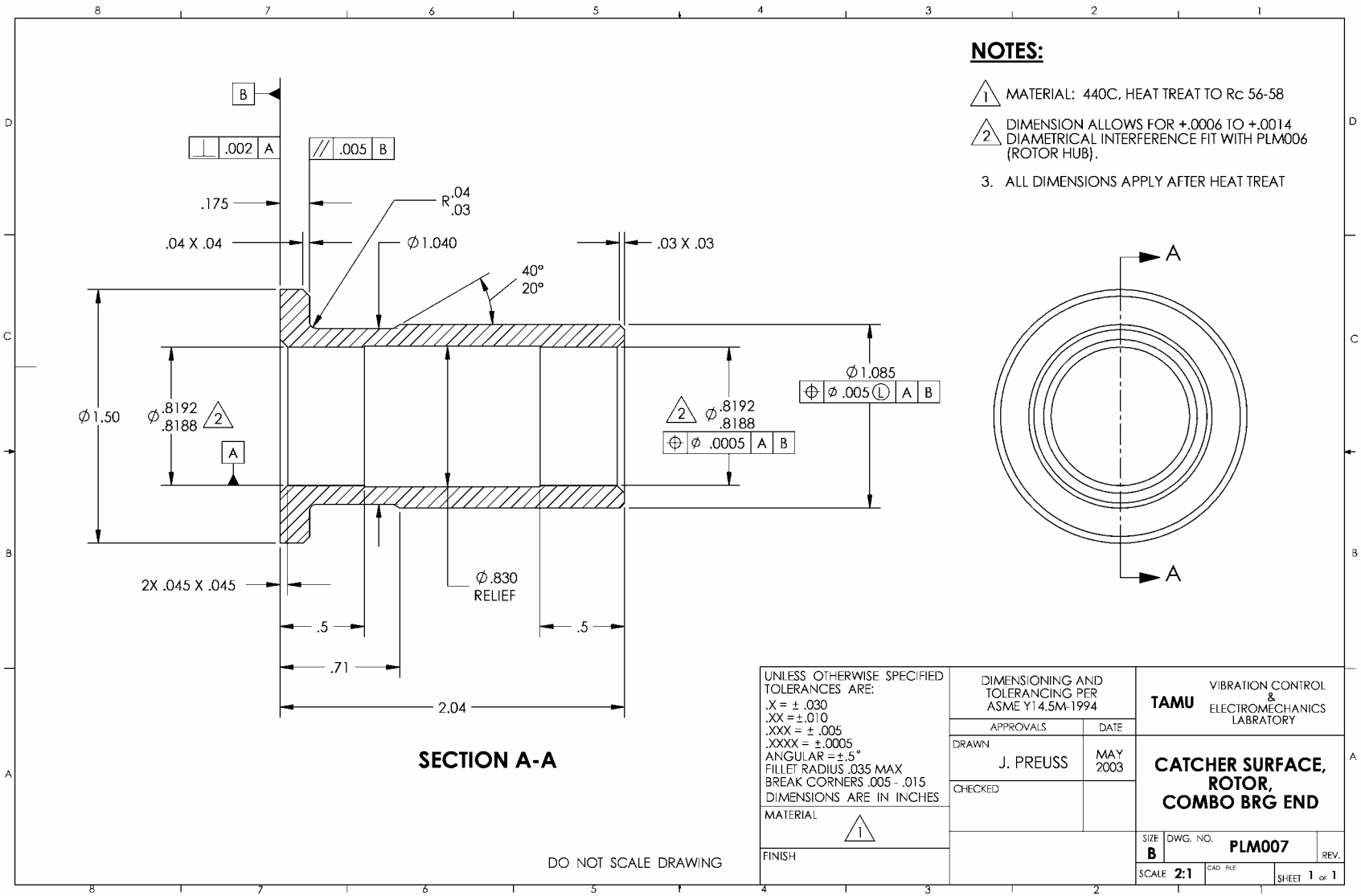

SECTION A-A

NOTES:

1. MATERIAL: 440C, HEAT TREAT TO Rc 56-58
2. DIMENSION ALLOWS FOR +.0006 TO +.0014 DIAMETRICAL INTERFERENCE FIT WITH PLM006 (ROTOR HUB).
3. ALL DIMENSIONS APPLY AFTER HEAT TREAT

DO NOT SCALE DRAWING

UNLESS OTHERWISE SPECIFIED TOLERANCES ARE: .X = ± .030 .XX = ±.010 .XXX = ± .005 .XXXX = ±.0005 ANGULAR = ±.5° FILLET RADIUS .035 MAX BREAK CORNERS .005 - .015 DIMENSIONS ARE IN INCHES	DIMENSIONING AND TOLERANCING PER ASME Y14.5M-1994		TAMU VIBRATION CONTROL & ELECTROMECHANICS LABRATORY
	APPROVALS	DATE	
	DRAWN J. PREUSS	MAY 2003	CATCHER SURFACE, ROTOR, COMBO BRG END
	CHECKED		
MATERIAL 1			SIZE B DWG. NO. PLM007 REV.
FINISH			SCALE 2:1 CAD FILE: SHEET 1 OF 1

NOTES:

1. MATERIAL: 440C, HEAT TREAT TO Rc 56-58
2. DIMENSION ALLOWS FOR +.0006 TO +.0014 DIAMETRICAL INTERFERENCE FIT WITH PLM006 (ROTOR HUB).
3. ALL DIMENSIONS APPLY AFTER HEAT TREAT

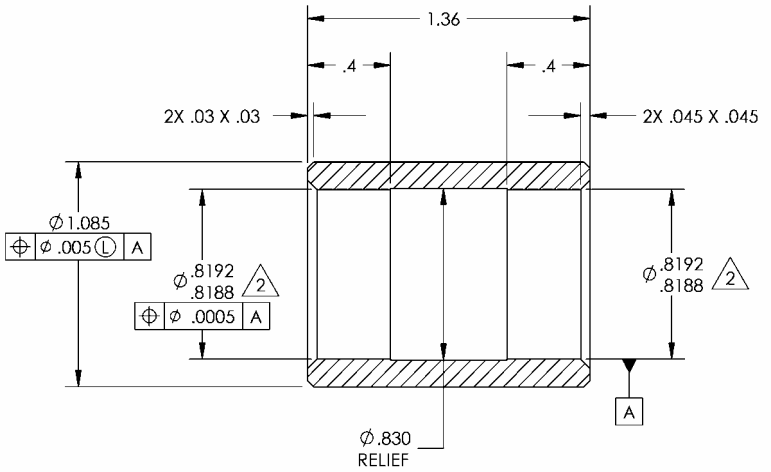

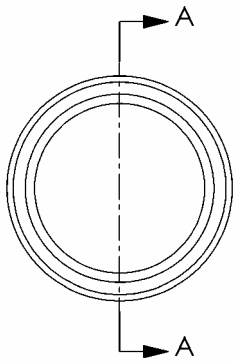

SECTION A-A

DO NOT SCALE DRAWING

UNLESS OTHERWISE SPECIFIED TOLERANCES ARE: .X = ± .030 .XX = ±.010 .XXX = ± .005 .XXXX = ±.0005 ANGULAR = ±.5° FILLET RADIUS .035 MAX BREAK CORNERS .005 - .015 DIMENSIONS ARE IN INCHES	DIMENSIONING AND TOLERANCING PER ASME Y14.5M-1994	TAMU VIBRATION CONTROL & ELECTROMECHANICS LABRATORY
MATERIAL 1	APPROVALS / DATE	
FINISH	DRAWN J. PREUSS — MAY 2003	CATCHER SURFACE, ROTOR, RADIAL BRG END
	CHECKED	
		SIZE B — DWG. NO. PLM008 — REV.
		SCALE 2:1 — CAD FILE: — SHEET 1 OF 1

NOTES:

1. MATERIAL: 440C, HEAT TREAT TO Rc 56-58
2. ALL DIMENSIONS APPLY AFTER HEAT TREAT
3. NO CENTER ALLOWED ON HEX END.

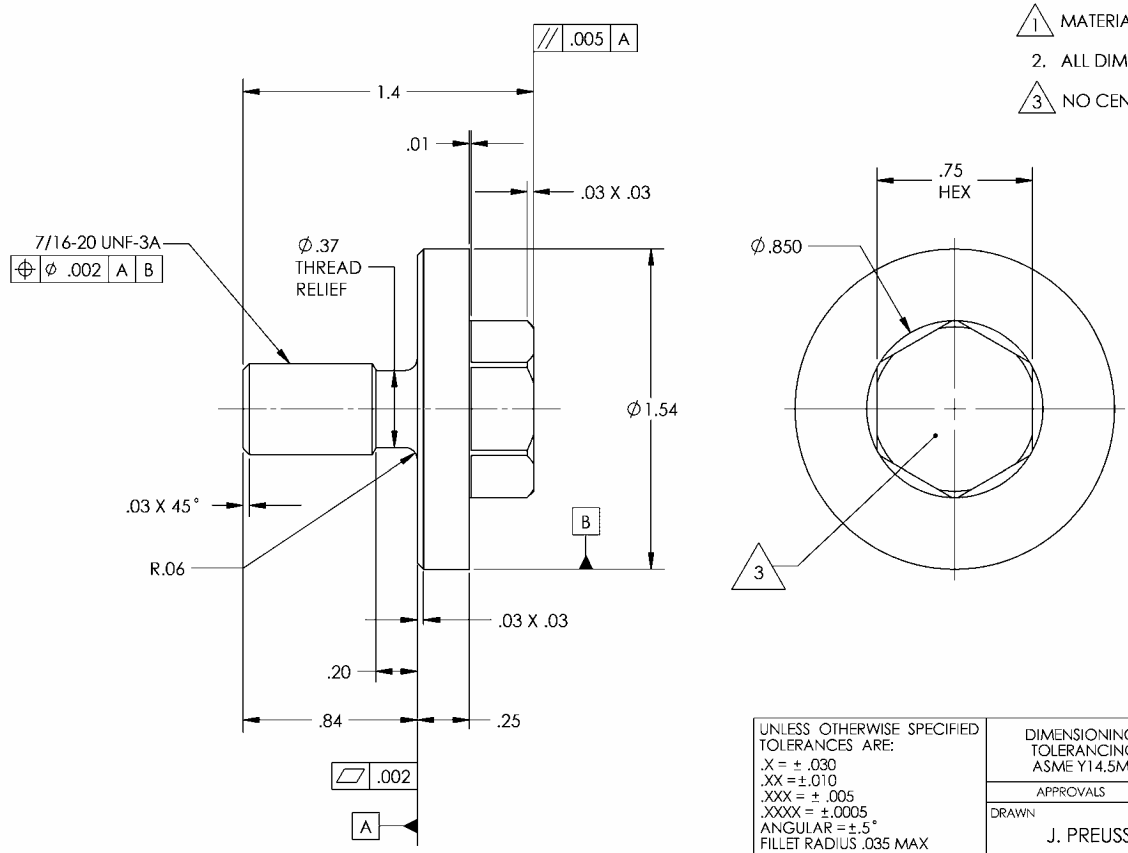

UNLESS OTHERWISE SPECIFIED TOLERANCES ARE: .X = ± .030 .XX = ±.010 .XXX = ± .005 .XXXX = ±.0005 ANGULAR = ±.5° FILLET RADIUS .035 MAX BREAK CORNERS .005 - .015 DIMENSIONS ARE IN INCHES	DIMENSIONING AND TOLERANCING PER ASME Y14.5M-1994	TAMU VIBRATION CONTROL & ELECTROMECHANICS LABRATORY
MATERIAL 1	APPROVALS / DATE	
FINISH	DRAWN J. PREUSS — MAY 2003	CATCHER SURFACE, AXIAL, ROTOR
DO NOT SCALE DRAWING	CHECKED	SIZE B — DWG. NO. PLM009 — REV.
		SCALE 2:1 — CAD FILE: — SHEET 1 OF 1

NOTES:

1. MATERIAL: TITANIUM 6AL-4V
2. DIMENSION ALLOWS FOR +.0023 TO +.0034 DIAMETRICAL INTERFERENCE FIT WITH PLM006 (ROTOR HUB)

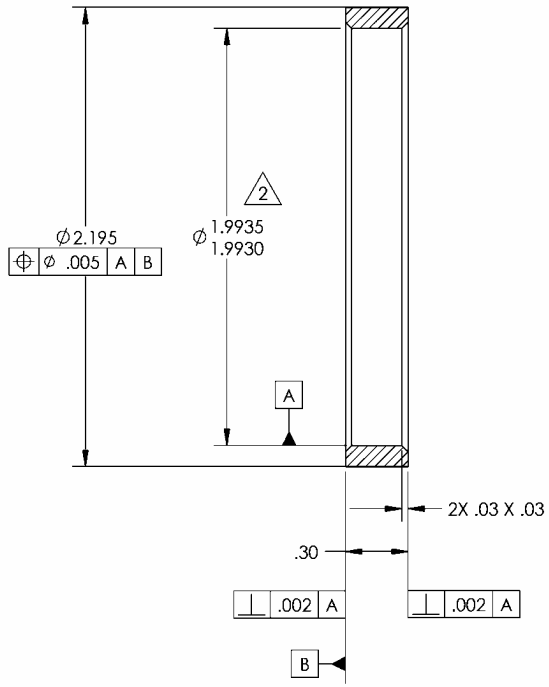

SECTION A-A

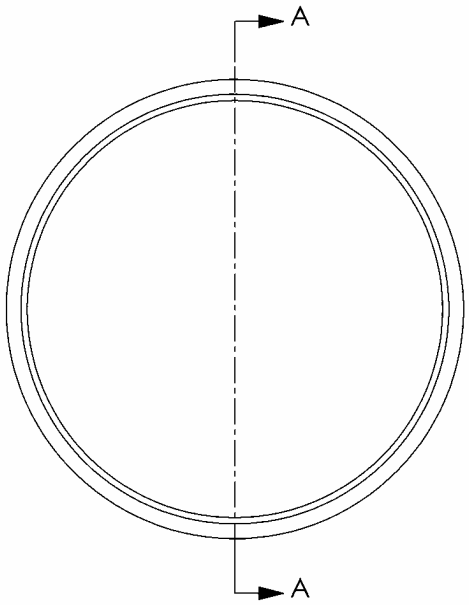

DO NOT SCALE DRAWING

UNLESS OTHERWISE SPECIFIED TOLERANCES ARE: .X = ± .030 .XX = ±.010 .XXX = ± .005 .XXXX = ±.0005 ANGULAR = ±.5° FILLET RADIUS .035 MAX BREAK CORNERS .005 - .015 DIMENSIONS ARE IN INCHES	DIMENSIONING AND TOLERANCING PER ASME Y14.5M-1994	TAMU VIBRATION CONTROL & ELECTROMECHANICS LABRATORY
MATERIAL 1	APPROVALS / DATE	
FINISH 63 RMS OR BETTER	DRAWN J. PREUSS — MAY 2003 CHECKED	**RETAINER, ROTOR LAM ASS'Y, COMBO & RADIAL**
		SIZE B — DWG. NO. PLM010 — REV. SCALE 2:1 — CAD FILE: — SHEET 1 OF 1

ITEM NO.	QTY.	PART NO.	DESCRIPTION
1	1	PLM006	ROTOR HUB
2	1	PLM007	CATCHER SURFACE, ROTOR, COMBO BRG END
3	1	PLM008	CATCHER SURFACE, ROTOR, RADIAL BRG END
4	1	CB006	ASS'Y, ROTOR LAMINATIONS, COMBO BRG
	1	CB004	ROTOR LAMINATION, COMBO BRG
	2	CB005	END PLATE, ROTOR LAM STACK, COMBO BRG
5	1	RB006	ASS'Y, Rotor Laminations, Radial Brg
	1	RB004	Rotor Lamination, Radial Brg
	2	RB005	End Plate, Rotor Lam Stack, Radial Brg
6	1	PLM009	CATCHER SURFACE, AXIAL, ROTOR
7	2	PLM010	RETAINER, ROTOR LAM ASS'Y, COMBO & RADIAL
8	1	NA	LOCTITE 609

NOTES:

1. ASSEMBLE WITH LOCTITE 609 PER MFG'S INSTRUCTIONS. -.0002 TO -.0010 FIT. ITEM 4 (CB006) AND ITEM 5 (RB006) CAN BE HEATED TO 250°F MAX. TO EASE ASSEMBLY.
2. HEAT ITEM 7 (PLM010) AND SHRINK ONTO ITEM 1 (PLM006). + .0023 TO +.0034 DIAMETRICAL INTERFERENCE FIT. 400°F MINIMUM TEMPERATURE DIFFERENCE REQ'D FOR ASS'Y.
3. HEAT ITEMS 2 (PLM007) & 3 (PLM008) AND SHRINK ONTO ITEM 1 (PLM006). +.0006 TO +.0014 DIAMETRICAL INTERFERENCE FIT. 450°F MIN. TEMPERATURE DIFFERENCE REQ'D FOR ASS'Y.
4. TORQUE TO 50-60 FT-LBS.
5. NOMINAL MATERIAL TO BE REMOVED FROM FACES OF ITEM 4 (CB006)
6. MAXIMUM EXTENT OF RADIUS.

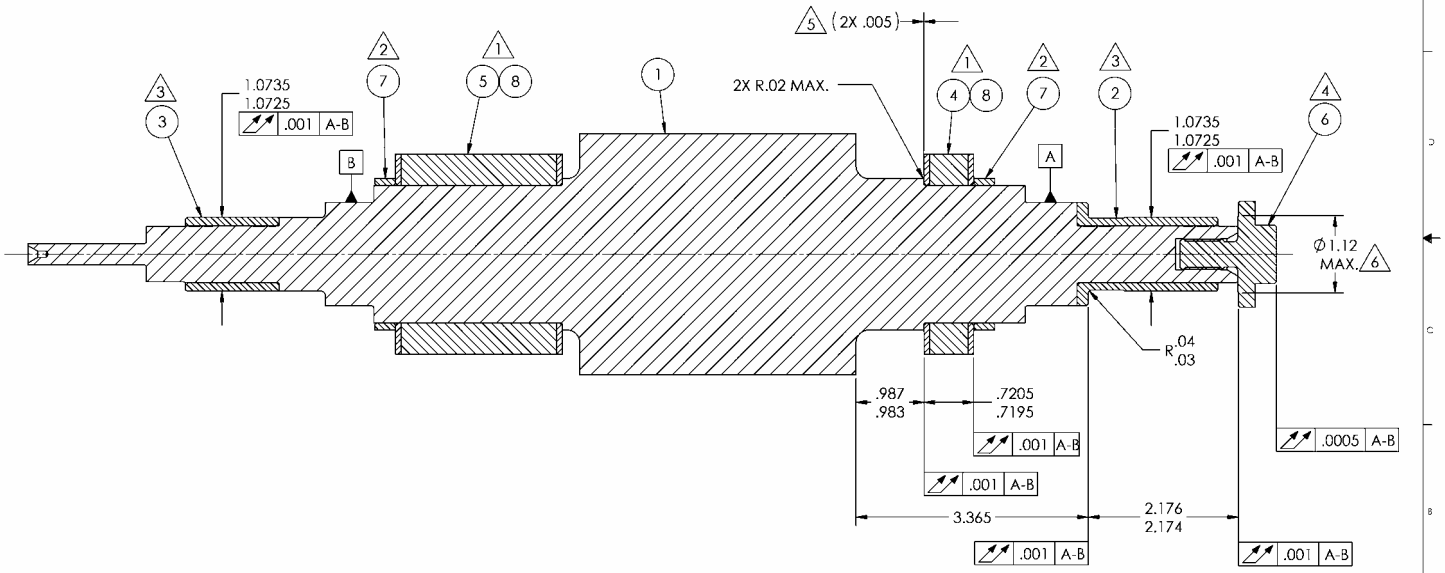

UNLESS OTHERWISE SPECIFIED TOLERANCES ARE:
.X = ± .030
.XX = ±.010
.XXX = ± .005
.XXXX = ±.0005
ANGULAR = ±.5°
FILLET RADIUS .035 MAX
BREAK CORNERS 45° X .015
DIMENSIONS ARE IN INCHES

MATERIAL

FINISH OR BETTER

DO NOT SCALE DRAWING

DIMENSIONING AND TOLERANCING PER ASME Y14.5M-1994

APPROVALS

DRAWN J. PREUSS DATE MAY 2003

CHECKED

TAMU VIBRATION CONTROL & ELECTROMECHANICS LABRATORY

ASS'Y, ROTOR, GRINDING

SIZE C DWG. NO. PLM011 REV.

SCALE 1:1 SHEET 1 1

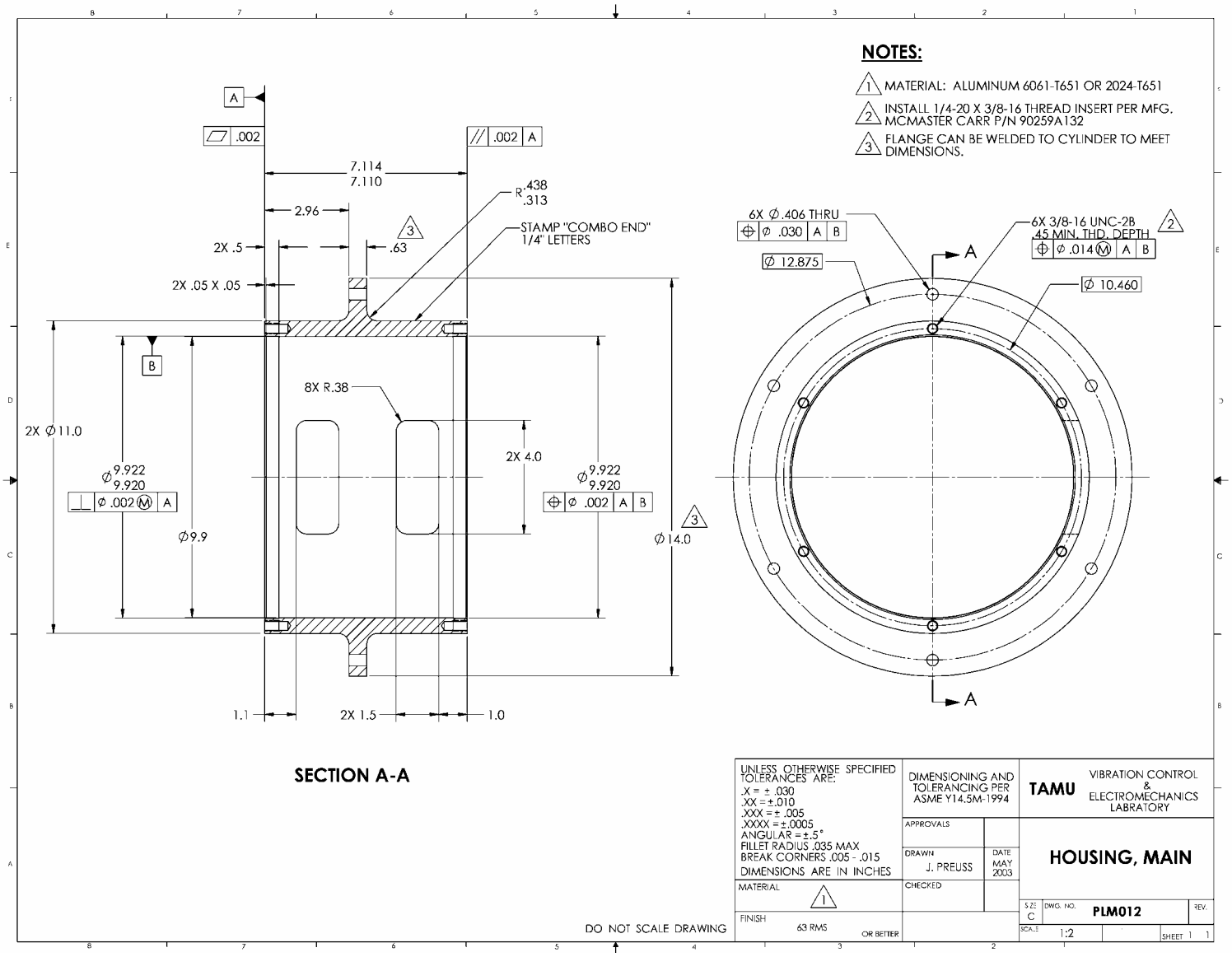
NOTES:
1 MATERIAL: ALUMINUM 6061-T651 OR 2024-T651
2 INSTALL 1/4-20 X 3/8-16 THREAD INSERT PER MFG. MCMASTER CARR P/N 90259A132
3 FLANGE CAN BE WELDED TO CYLINDER TO MEET DIMENSIONS.
A
.002
.002 A
7.114
7.110
2.96
2X .5
.63
R:.438
.313
STAMP "COMBO END"
1/4" LETTERS
2X .05 X .05
B
8X R.38
2X Ø11.0
Ø9.922
9.920
Ø .002 M A
2X 4.0
Ø9.922
9.920
Ø .002 A B
Ø9.9
Ø14.0
1.1
2X 1.5
1.0
6X Ø.406 THRU
Ø .030 A B
Ø 12.875
6X 3/8-16 UNC-2B
.45 MIN. THD. DEPTH
Ø .014 M A B
Ø 10.460
SECTION A-A
UNLESS OTHERWISE SPECIFIED TOLERANCES ARE:
.X = ± .030
.XX = ±.010
.XXX = ± .005
.XXXX = ±.0005
ANGULAR = ±.5°
FILLET RADIUS .035 MAX
BREAK CORNERS .005 - .015
DIMENSIONS ARE IN INCHES
MATERIAL 1
FINISH 63 RMS OR BETTER
DO NOT SCALE DRAWING
DIMENSIONING AND TOLERANCING PER ASME Y14.5M-1994
APPROVALS
DRAWN J. PREUSS
DATE MAY 2003
CHECKED
TAMU VIBRATION CONTROL & ELECTROMECHANICS LABRATORY
HOUSING, MAIN
SIZE C
DWG. NO. PLM012
REV.
SCALE 1:2
SHEET 1 1

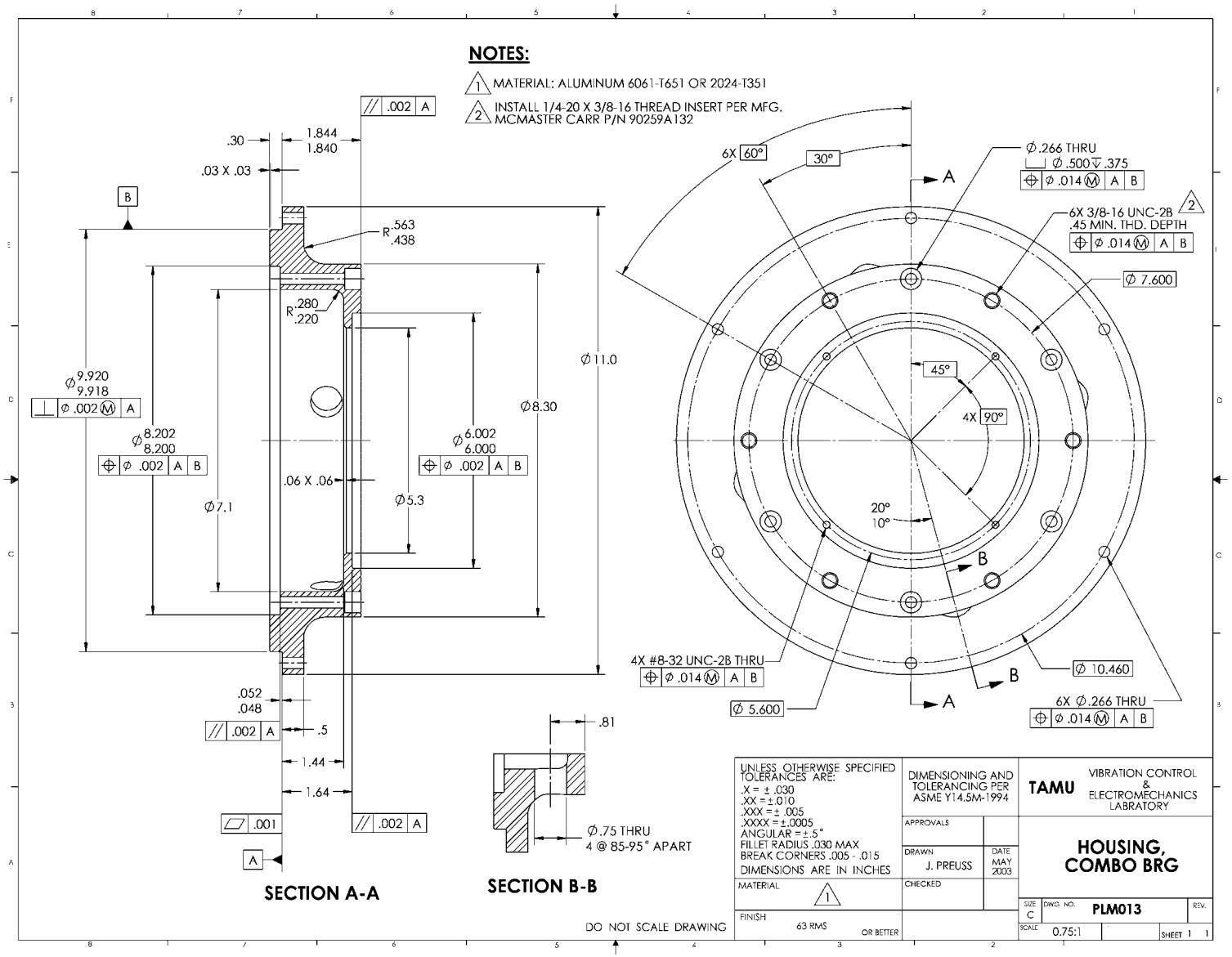
NOTES:
1 MATERIAL: ALUMINUM 6061-T651 OR 2024-T351
2 INSTALL 1/4-20 X 3/8-16 THREAD INSERT PER MFG. MCMASTER CARR P/N 90259A132
.002 A
.30
1.844
1.840
.03 X .03
B
R.563
.438
R.280
.220
Ø11.0
Ø8.30
Ø9.920
9.918
Ø .002 M A
Ø8.202
8.200
Ø .002 A B
Ø6.002
6.000
Ø .002 A B
.06 X .06
Ø7.1
Ø5.3
.052
.048
.002 A
.5
1.44
1.64
.001
.002 A
A
SECTION A-A
.81
Ø.75 THRU
4 @ 85-95° APART
SECTION B-B
6X 60°
30°
Ø.266 THRU
Ø.500↧.375
Ø .014 M A B
6X 3/8-16 UNC-2B
.45 MIN. THD. DEPTH
Ø .014 M A B
2
Ø 7.600
45°
4X 90°
20°
10°
4X #8-32 UNC-2B THRU
Ø .014 M A B
Ø 5.600
Ø 10.460
6X Ø.266 THRU
Ø .014 M A B
UNLESS OTHERWISE SPECIFIED TOLERANCES ARE:
.X = ± .030
.XX = ± .010
.XXX = ± .005
.XXXX = ± .0005
ANGULAR = ± .5°
FILLET RADIUS .030 MAX
BREAK CORNERS .005 - .015
DIMENSIONS ARE IN INCHES
MATERIAL 1
FINISH 63 RMS OR BETTER
DO NOT SCALE DRAWING
DIMENSIONING AND TOLERANCING PER ASME Y14.5M-1994
APPROVALS
DRAWN J. PREUSS
DATE MAY 2003
CHECKED
TAMU VIBRATION CONTROL & ELECTROMECHANICS LABRATORY
HOUSING, COMBO BRG
SIZE C
DWG. NO. PLM013
REV.
SCALE 0.75:1
SHEET 1 1

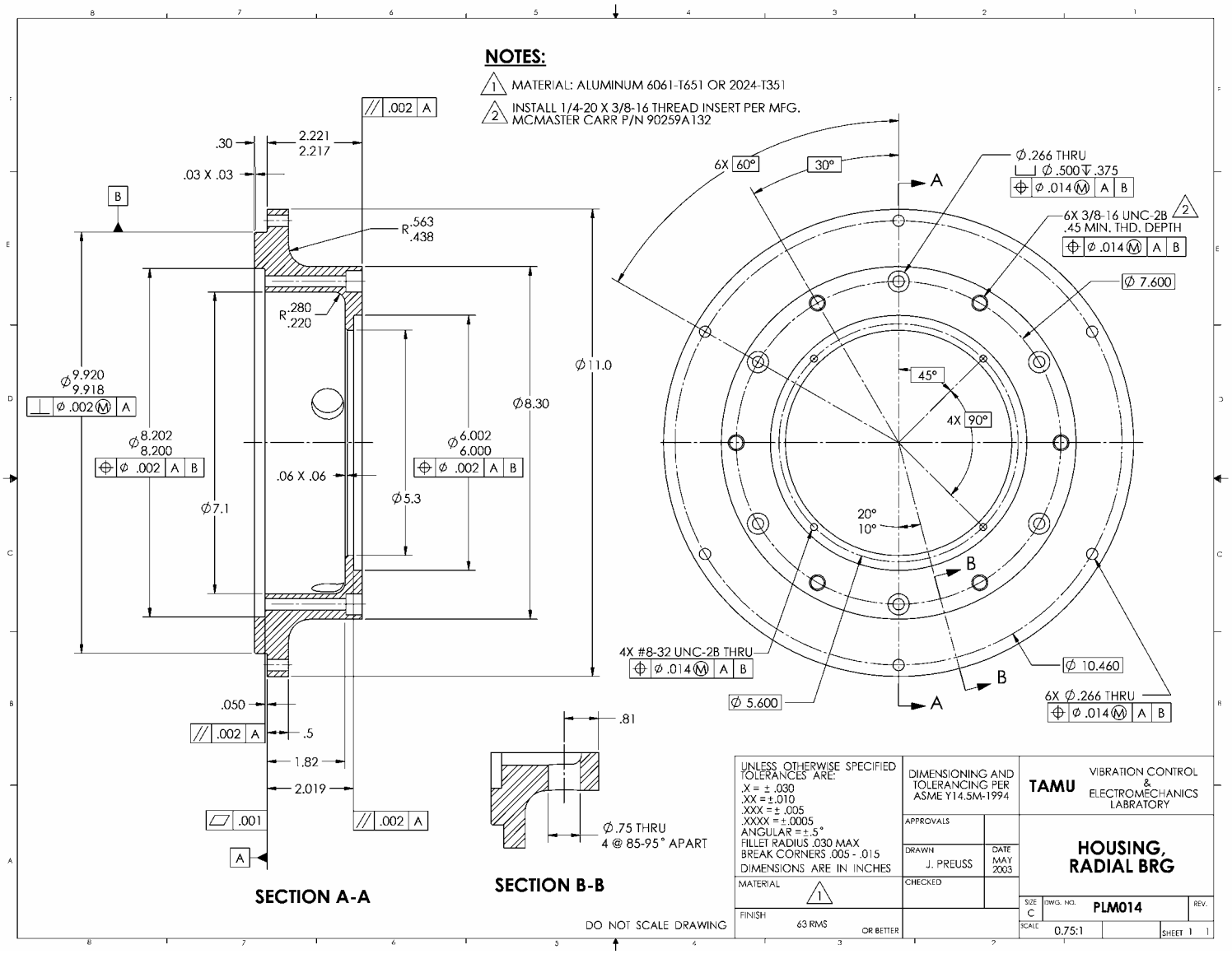
NOTES:
1 MATERIAL: ALUMINUM 6061-T651 OR 2024-T351
2 INSTALL 1/4-20 X 3/8-16 THREAD INSERT PER MFG. MCMASTER CARR P/N 90259A132
SECTION A-A
SECTION B-B
DO NOT SCALE DRAWING
UNLESS OTHERWISE SPECIFIED TOLERANCES ARE:
.X = ± .030
.XX = ±.010
.XXX = ± .005
.XXXX = ±.0005
ANGULAR = ±.5°
FILLET RADIUS .030 MAX
BREAK CORNERS .005 - .015
DIMENSIONS ARE IN INCHES
MATERIAL 1
FINISH 63 RMS OR BETTER
DIMENSIONING AND TOLERANCING PER ASME Y14.5M-1994
APPROVALS
DRAWN J. PREUSS
DATE MAY 2003
CHECKED
TAMU VIBRATION CONTROL & ELECTROMECHANICS LABRATORY
HOUSING, RADIAL BRG
SIZE C
DWG. NO. PLM014
REV.
SCALE 0.75:1
SHEET 1 1

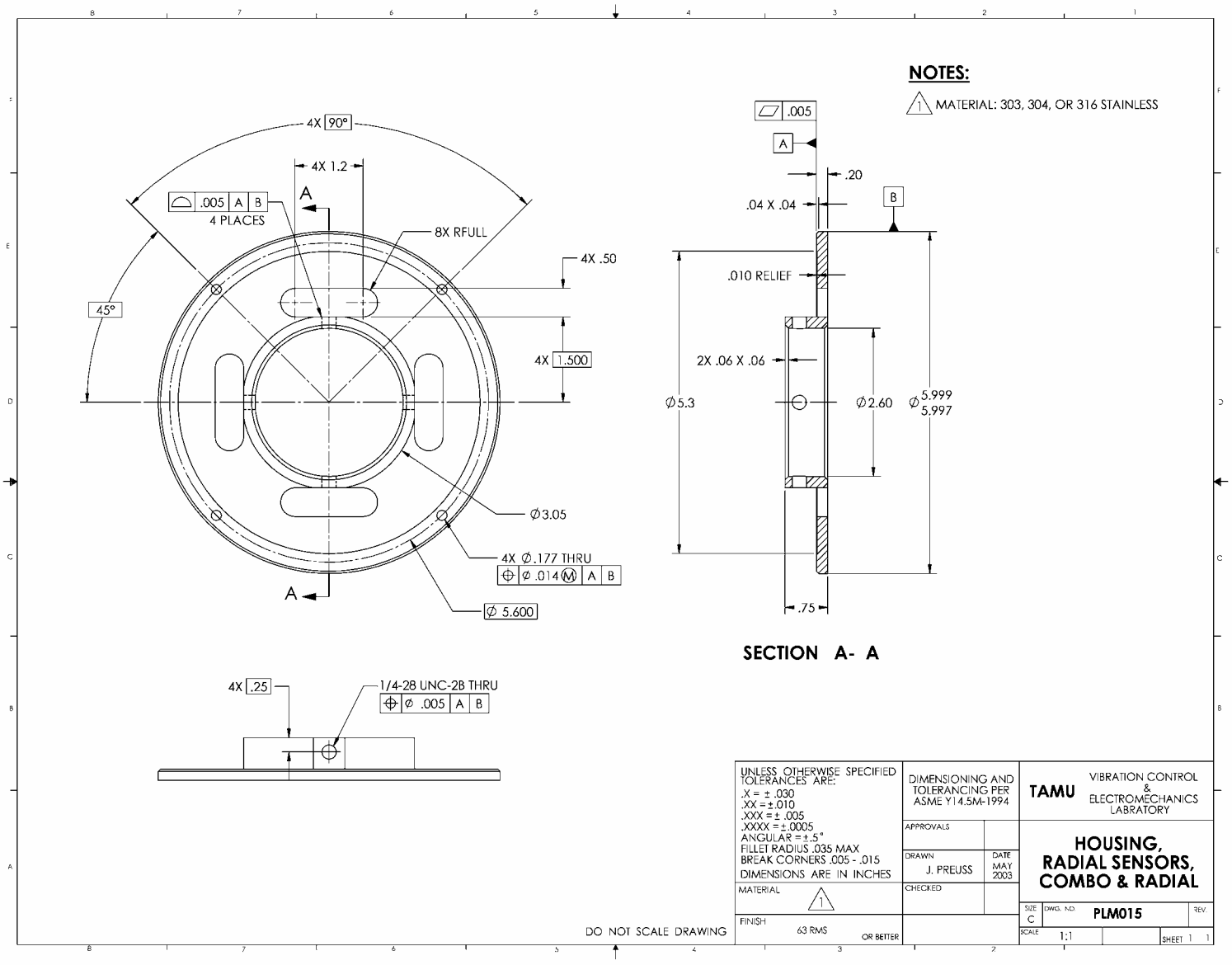
NOTES:
1 MATERIAL: 303, 304, OR 316 STAINLESS
4X 90°
4X 1.2
.005 A B
4 PLACES
8X RFULL
4X .50
45°
4X 1.500
Ø3.05
4X Ø.177 THRU
Ø .014 M A B
Ø 5.600
A
.005
A
.20
.04 X .04
B
.010 RELIEF
2X .06 X .06
Ø5.3
Ø2.60
Ø5.999
5.997
.75
SECTION A- A
4X .25
1/4-28 UNC-2B THRU
Ø .005 A B
UNLESS OTHERWISE SPECIFIED TOLERANCES ARE:
.X = ± .030
.XX = ±.010
.XXX = ± .005
.XXXX = ± .0005
ANGULAR = ±.5°
FILLET RADIUS .035 MAX
BREAK CORNERS .005 - .015
DIMENSIONS ARE IN INCHES
MATERIAL
1
FINISH
63 RMS
OR BETTER
DO NOT SCALE DRAWING
DIMENSIONING AND TOLERANCING PER ASME Y14.5M-1994
APPROVALS
DRAWN
J. PREUSS
DATE
MAY 2003
CHECKED
TAMU
VIBRATION CONTROL & ELECTROMECHANICS LABRATORY
HOUSING, RADIAL SENSORS, COMBO & RADIAL
SIZE C
DWG. NO. PLM015
REV.
SCALE 1:1
SHEET 1 1

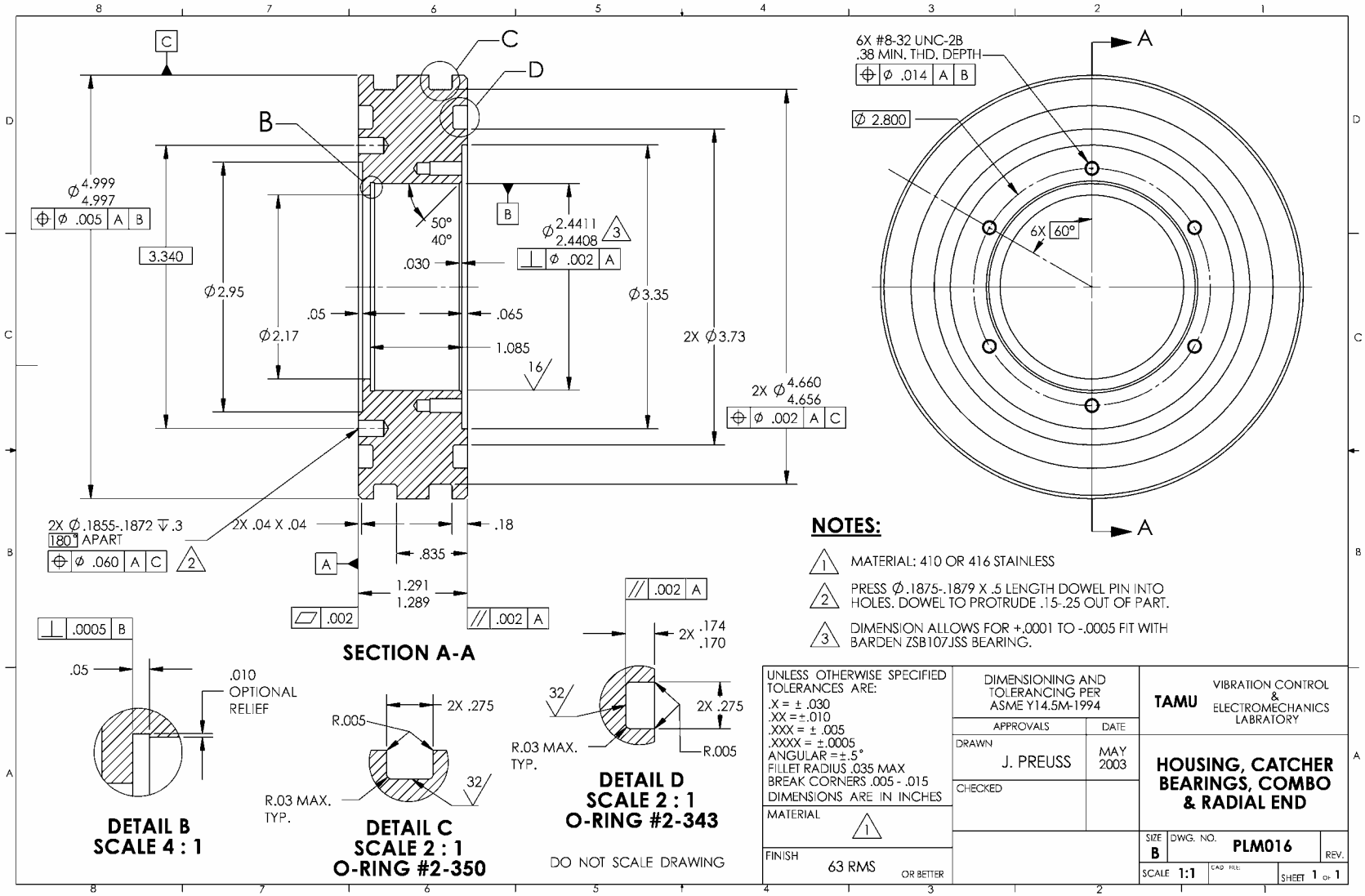

NOTES:

1. MATERIAL: 410 OR 416 STAINLESS
2. PRESS Ø.1875-.1879 X .5 LENGTH DOWEL PIN INTO HOLES. DOWEL TO PROTRUDE .15-.25 OUT OF PART.
3. DIMENSION ALLOWS FOR +.0001 TO -.0005 FIT WITH BARDEN ZSB107JSS BEARING.

UNLESS OTHERWISE SPECIFIED TOLERANCES ARE: .X = ± .030 .XX = ±.010 .XXX = ± .005 .XXXX = ±.0005 ANGULAR = ±.5° FILLET RADIUS .035 MAX BREAK CORNERS .005 - .015 DIMENSIONS ARE IN INCHES	DIMENSIONING AND TOLERANCING PER ASME Y14.5M-1994	TAMU VIBRATION CONTROL & ELECTROMECHANICS LABRATORY
MATERIAL 1	APPROVALS / DATE	HOUSING, CATCHER BEARINGS, COMBO & RADIAL END
FINISH 63 RMS OR BETTER	DRAWN J. PREUSS MAY 2003 CHECKED	SIZE B · DWG. NO. PLM016 · REV. SCALE 1:1 · CAD FILE: · SHEET 1 OF 1

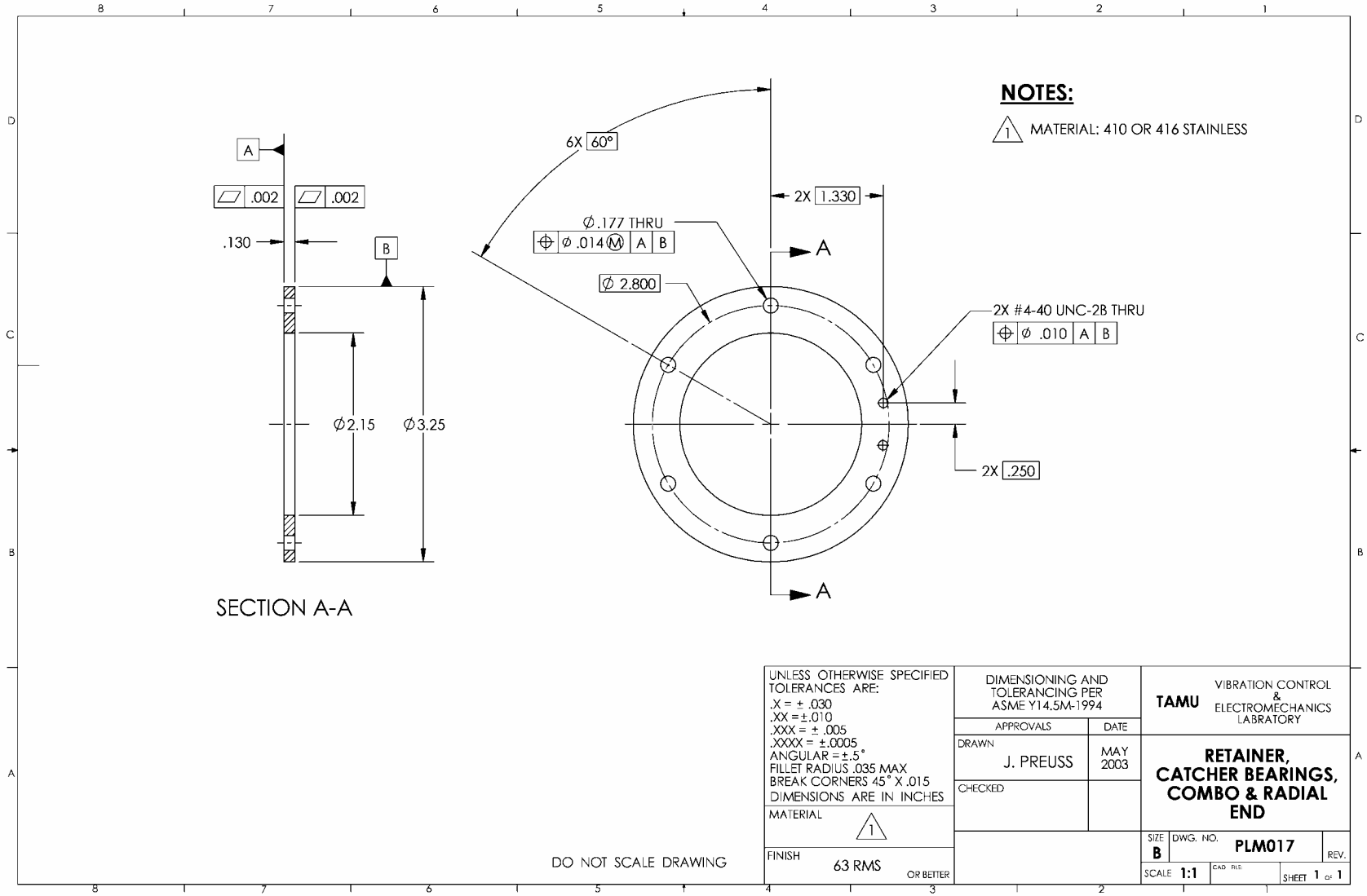
NOTES:
1 MATERIAL: 410 OR 416 STAINLESS
A
.002
.002
.130
B
Ø2.15
Ø3.25
SECTION A-A
6X 60°
2X 1.330
Ø.177 THRU
Ø .014 M A B
Ø 2.800
2X #4-40 UNC-2B THRU
Ø .010 A B
2X .250
A
A
UNLESS OTHERWISE SPECIFIED TOLERANCES ARE:
.X = ± .030
.XX = ±.010
.XXX = ± .005
.XXXX = ±.0005
ANGULAR = ±.5°
FILLET RADIUS .035 MAX
BREAK CORNERS 45° X .015
DIMENSIONS ARE IN INCHES
MATERIAL
1
FINISH
63 RMS
OR BETTER
DO NOT SCALE DRAWING
DIMENSIONING AND TOLERANCING PER ASME Y14.5M-1994
APPROVALS
DATE
DRAWN
J. PREUSS
MAY 2003
CHECKED
TAMU
VIBRATION CONTROL & ELECTROMECHANICS LABRATORY
RETAINER, CATCHER BEARINGS, COMBO & RADIAL END
SIZE
B
DWG. NO.
PLM017
REV.
SCALE 1:1
CAD FILE:
SHEET 1 OF 1

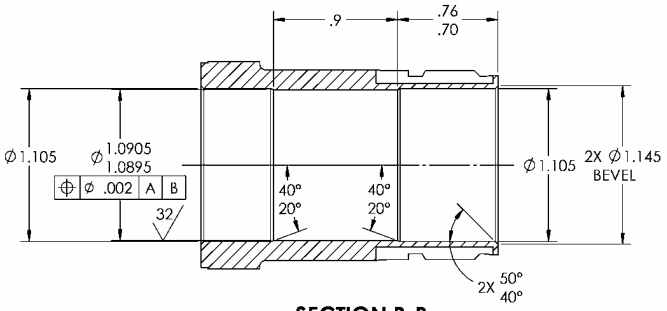

SECTION B-B

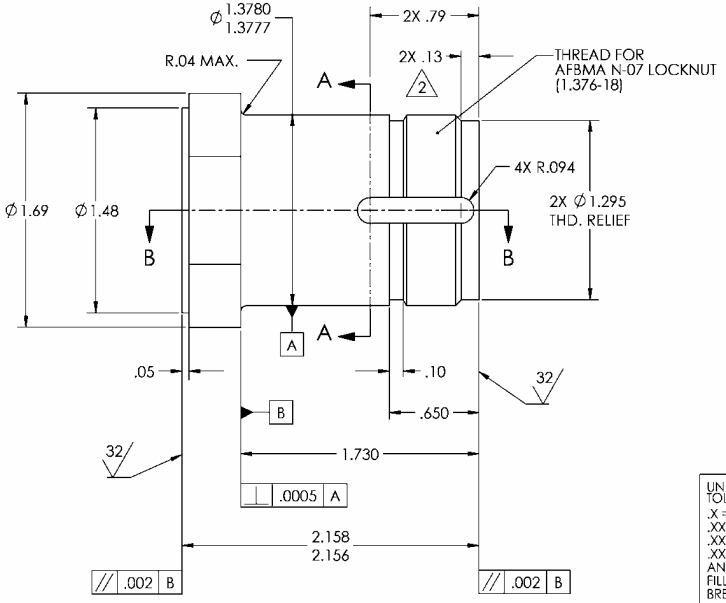

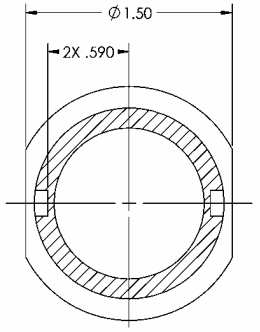

SECTION A-A

NOTES:

1. MATERIAL: AISI 52100
2. DIMENSION APPLIES TO CENTER OF KEYWAY RADIUS.
3. DIMENSION ALLOWS FOR +.0003 TO -.0003 DIAMETRICAL FIT WITH BARDEN BEARING ZSB107JSS.

UNLESS OTHERWISE SPECIFIED TOLERANCES ARE: .X = ± .030 .XX = ± .010 .XXX = ± .005 .XXXX = ± .0005 ANGULAR = ± .5° FILLET RADIUS .035 MAX BREAK CORNERS 45° X .015 DIMENSIONS ARE IN INCHES	DIMENSIONING AND TOLERANCING PER ASME Y14.5M-1994	TAMU VIBRATION CONTROL & ELECTROMECHANICS LABRATORY
	APPROVALS	CATCHER SURFACE, STATOR, COMBO & RADIAL END
	DRAWN J. PREUSS DATE MAY 2003	
MATERIAL 1	CHECKED	
FINISH 63 RMS OR BETTER		SIZE C DWG. NO. PLM018 REV.
DO NOT SCALE DRAWING		SCALE 2:1 SHEET 1 1

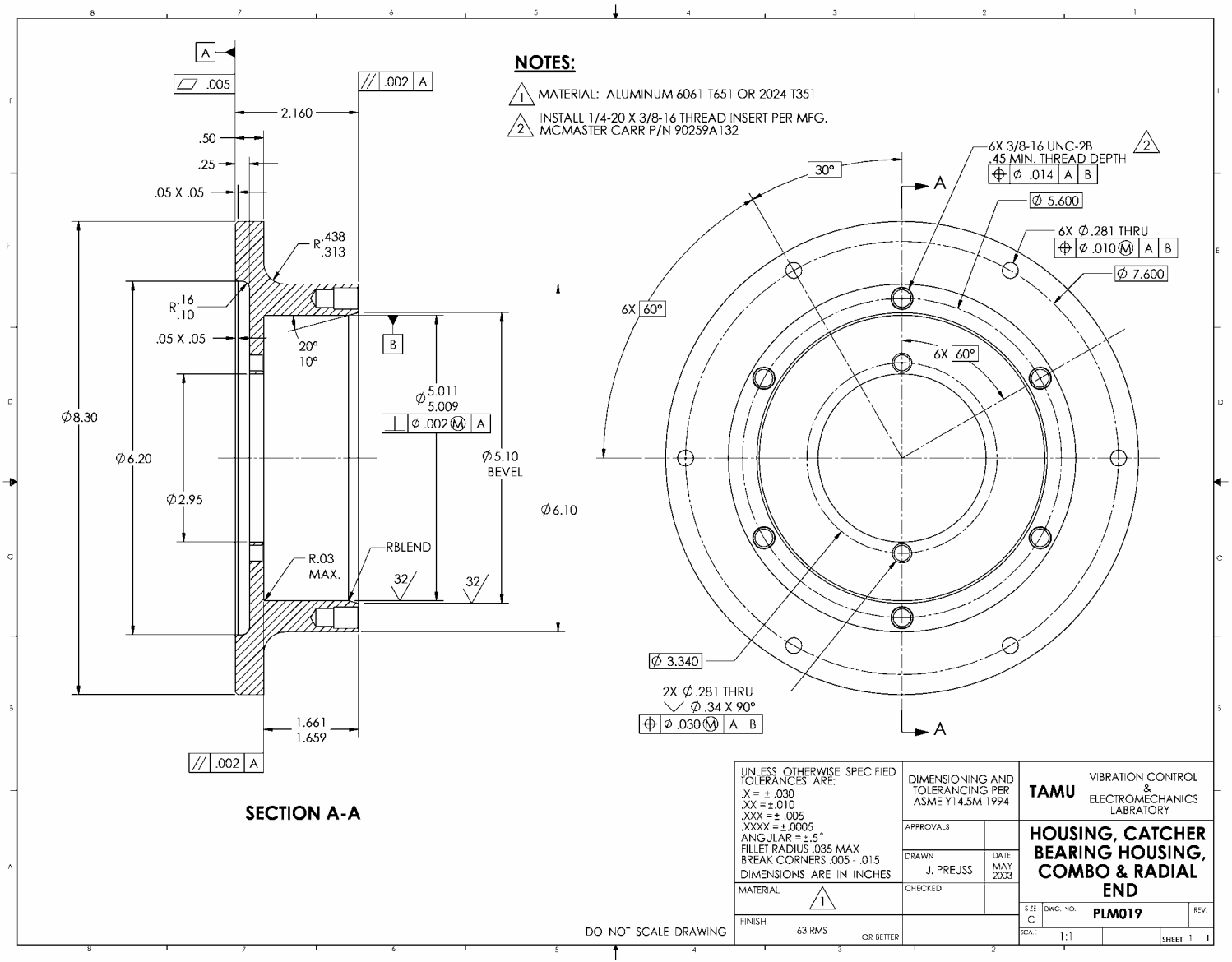
NOTES:
1 MATERIAL: ALUMINUM 6061-T651 OR 2024-T351
2 INSTALL 1/4-20 X 3/8-16 THREAD INSERT PER MFG. MCMASTER CARR P/N 90259A132
A
.005
.002 A
2.160
.50
.25
.05 X .05
R.438
.313
R.16
.10
.05 X .05
20°
10°
B
Ø8.30
Ø6.20
Ø2.95
Ø5.011
5.009
Ø .002 M A
Ø5.10
BEVEL
Ø6.10
R.03
MAX.
RBLEND
32
32
1.661
1.659
.002 A
SECTION A-A
30°
6X 60°
6X 3/8-16 UNC-2B
.45 MIN. THREAD DEPTH
Ø .014 A B
Ø 5.600
6X Ø.281 THRU
Ø .010 M A B
Ø 7.600
6X 60°
Ø 3.340
2X Ø.281 THRU
Ø .34 X 90°
Ø .030 M A B
A
UNLESS OTHERWISE SPECIFIED TOLERANCES ARE:
.X = ± .030
.XX = ± .010
.XXX = ± .005
.XXXX = ± .0005
ANGULAR = ± .5°
FILLET RADIUS .035 MAX
BREAK CORNERS .005 - .015
DIMENSIONS ARE IN INCHES
MATERIAL 1
FINISH 63 RMS OR BETTER
DO NOT SCALE DRAWING
DIMENSIONING AND TOLERANCING PER ASME Y14.5M-1994
APPROVALS
DRAWN J. PREUSS
DATE MAY 2003
CHECKED
TAMU VIBRATION CONTROL & ELECTROMECHANICS LABRATORY
HOUSING, CATCHER BEARING HOUSING, COMBO & RADIAL END
SIZE C
DWG. NO. PLM019
REV.
SCALE 1:1
SHEET 1 1

NOTES:

1. MATERIAL: ALUMINUM 6061-T651 OR 2024-T351

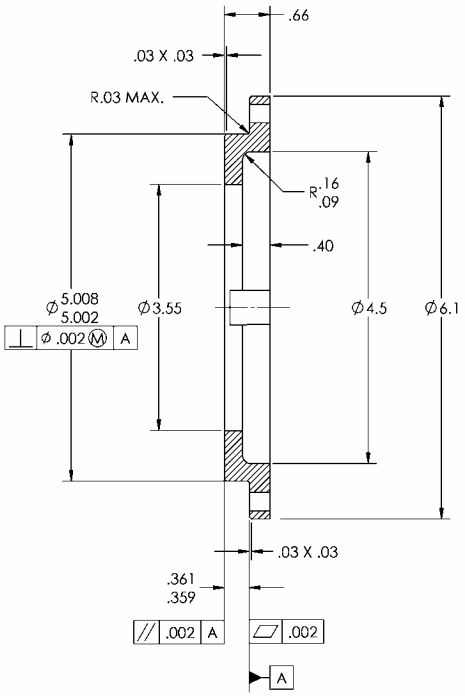

SECTION A-A

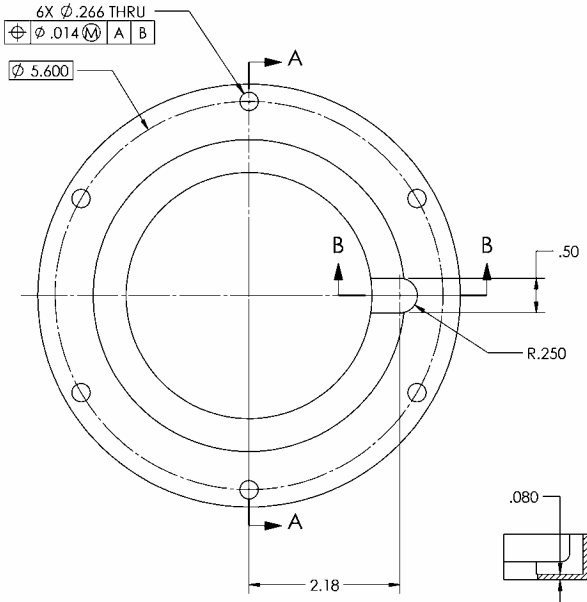

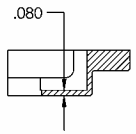

SECTION B-B

UNLESS OTHERWISE SPECIFIED TOLERANCES ARE: .X = ± .030 .XX = ±.010 .XXX = ± .005 .XXXX = ±.0005 ANGULAR = ±.5° FILLET RADIUS .035 MAX BREAK CORNERS .005 - .015 DIMENSIONS ARE IN INCHES	DIMENSIONING AND TOLERANCING PER ASME Y14.5M-1994	TAMU VIBRATION CONTROL & ELECTROMECHANICS LABRATORY
	APPROVALS	RETAINER, CATCHER BEARING HOUSING, COMBO END
	DRAWN J. PREUSS — DATE MAY 2003	
MATERIAL 1	CHECKED	SIZE C — DWG. NO. PLM020 — REV.
FINISH 63 RMS OR BETTER		SCA. 1:1 — SHEET 1 1

DO NOT SCALE DRAWING

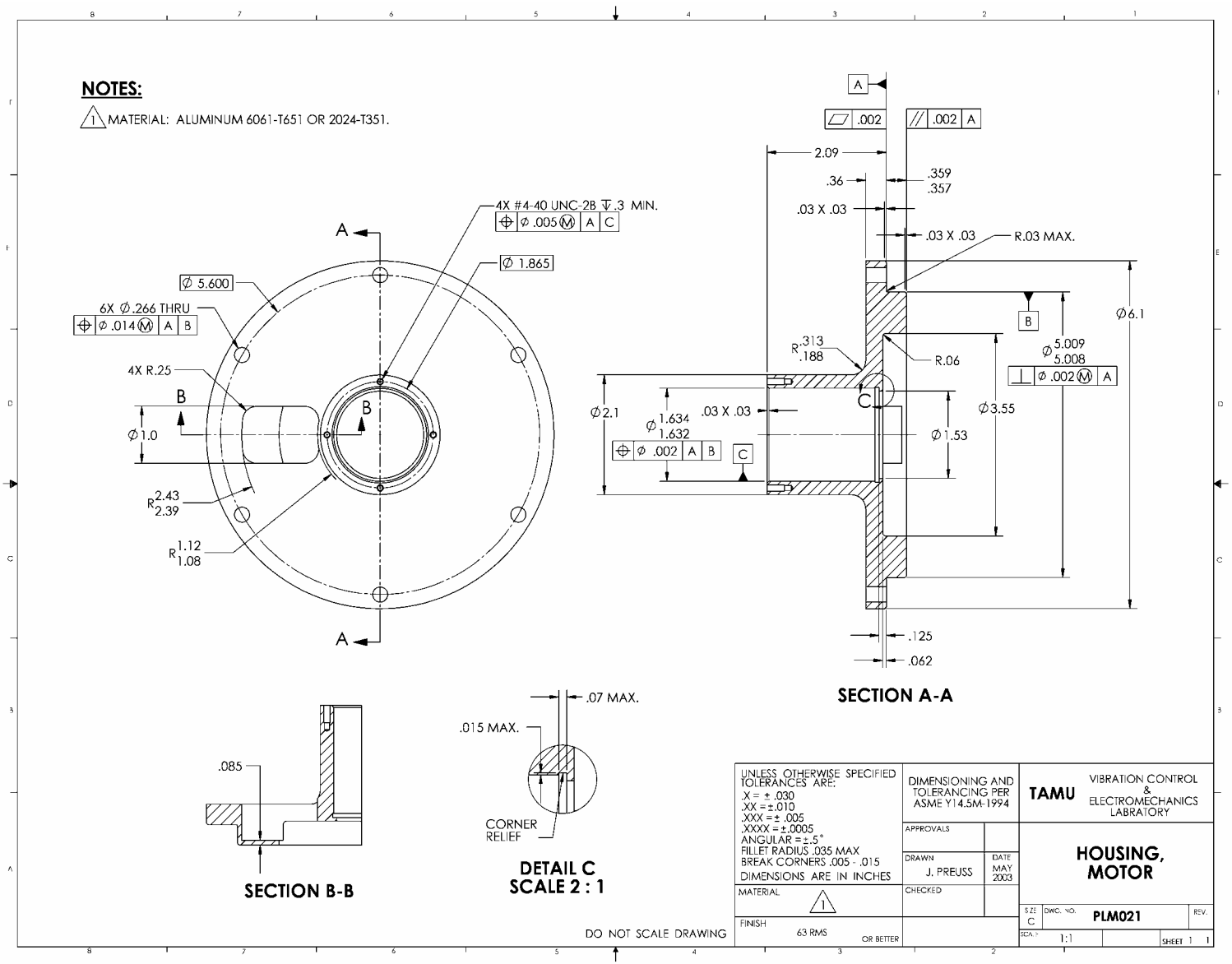
NOTES:
1 MATERIAL: ALUMINUM 6061-T651 OR 2024-T351.
4X #4-40 UNC-2B ↧.3 MIN.
⌖ Ø .005 Ⓜ A C
Ø 1.865
Ø 5.600
6X Ø.266 THRU
⌖ Ø .014 Ⓜ A B
4X R.25
B
Ø1.0
R2.43 2.39
R1.12 1.08
A
.002
// .002 A
2.09
.36
.359 .357
.03 X .03
.03 X .03
R.03 MAX.
Ø6.1
R.313 .188
R.06
Ø 5.009 5.008
⊥ Ø .002 Ⓜ A
Ø2.1
Ø 1.634 1.632
.03 X .03
⌖ Ø .002 A B C
Ø3.55
Ø1.53
.125
.062
SECTION A-A
.085
SECTION B-B
.07 MAX.
.015 MAX.
CORNER RELIEF
DETAIL C
SCALE 2 : 1
DO NOT SCALE DRAWING
UNLESS OTHERWISE SPECIFIED TOLERANCES ARE:
.X = ± .030
.XX = ± .010
.XXX = ± .005
.XXXX = ± .0005
ANGULAR = ± .5°
FILLET RADIUS .035 MAX
BREAK CORNERS .005 - .015
DIMENSIONS ARE IN INCHES
MATERIAL 1
FINISH 63 RMS OR BETTER
DIMENSIONING AND TOLERANCING PER ASME Y14.5M-1994
APPROVALS
DRAWN J. PREUSS
DATE MAY 2003
CHECKED
TAMU VIBRATION CONTROL & ELECTROMECHANICS LABRATORY
HOUSING, MOTOR
SIZE C
DWG. NO. PLM021
REV.
SCA. 1:1
SHEET 1 1

NOTES:

1. MATERIAL: ALUMINUM 6061-T651 OR 2024-T351

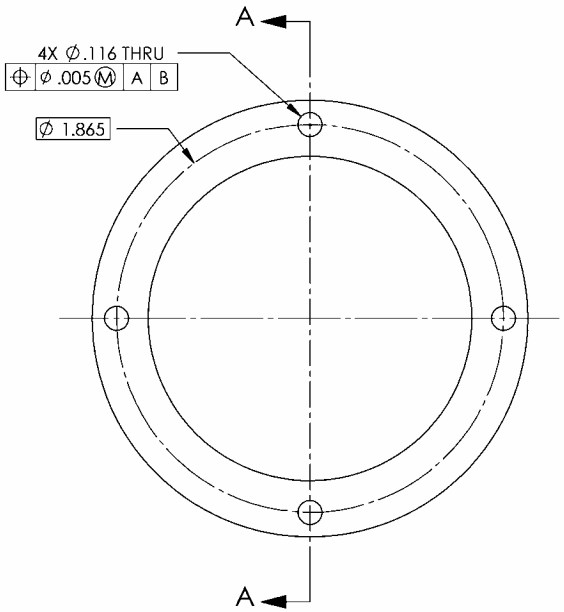

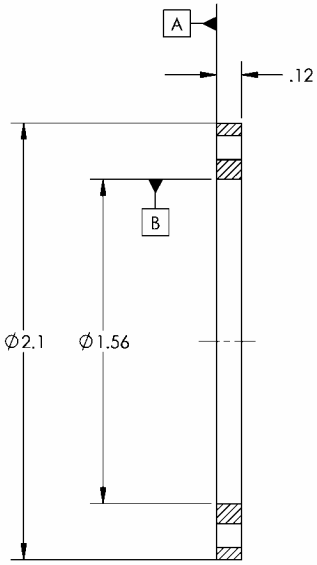

SECTION A-A

DO NOT SCALE DRAWING

UNLESS OTHERWISE SPECIFIED TOLERANCES ARE: .X = ± .030 .XX = ±.010 .XXX = ± .005 .XXXX = ±.0005 ANGULAR = ±.5° FILLET RADIUS .035 MAX BREAK CORNERS 45° X .015 DIMENSIONS ARE IN INCHES	DIMENSIONING AND TOLERANCING PER ASME Y14.5M-1994	TAMU VIBRATION CONTROL & ELECTROMECHANICS LABRATORY
MATERIAL 1	APPROVALS / DATE	
FINISH	DRAWN J. PREUSS — DEC 2002	**RETAINER, MOTOR**
	CHECKED	SIZE B — DWG. NO. PLM022 — REV.
		SCALE 2:1 — CAD FILE: — SHEET 1 OF 1

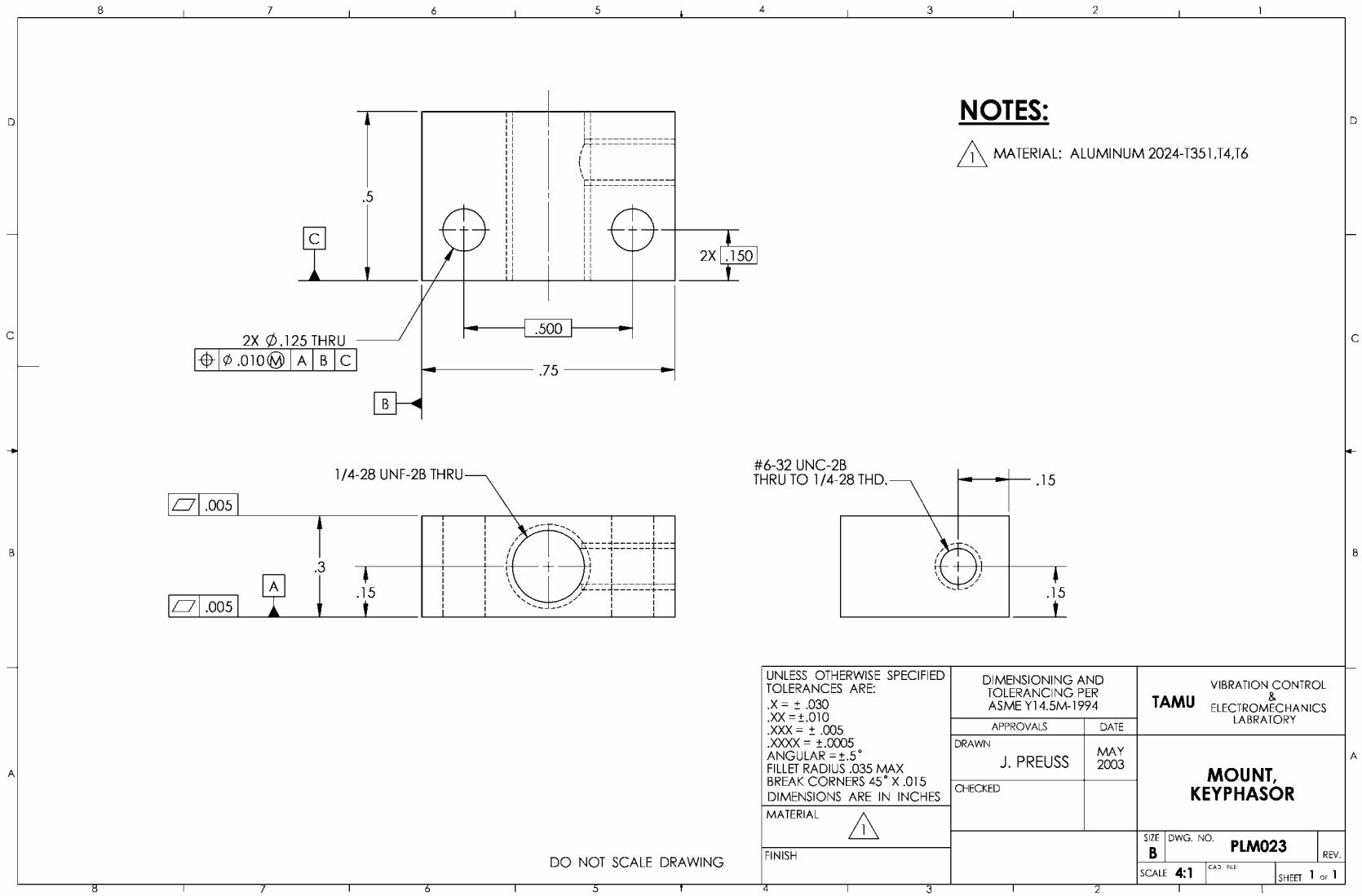
NOTES:
1 MATERIAL: ALUMINUM 2024-T351,T4,T6
.5
C
2X .150
2X Ø.125 THRU
⌖ Ø .010 Ⓜ A B C
.500
.75
B
1/4-28 UNF-2B THRU
.005
.3
A
.15
.005
#6-32 UNC-2B
THRU TO 1/4-28 THD.
.15
.15
DO NOT SCALE DRAWING
UNLESS OTHERWISE SPECIFIED TOLERANCES ARE:
.X = ± .030
.XX = ±.010
.XXX = ± .005
.XXXX = ±.0005
ANGULAR = ±.5°
FILLET RADIUS .035 MAX
BREAK CORNERS 45° X .015
DIMENSIONS ARE IN INCHES
MATERIAL 1
FINISH
DIMENSIONING AND TOLERANCING PER ASME Y14.5M-1994
APPROVALS
DATE
DRAWN J. PREUSS MAY 2003
CHECKED
TAMU VIBRATION CONTROL & ELECTROMECHANICS LABRATORY
MOUNT, KEYPHASOR
SIZE B
DWG. NO. PLM023
REV.
SCALE 4:1
CAD FILE:
SHEET 1 OF 1

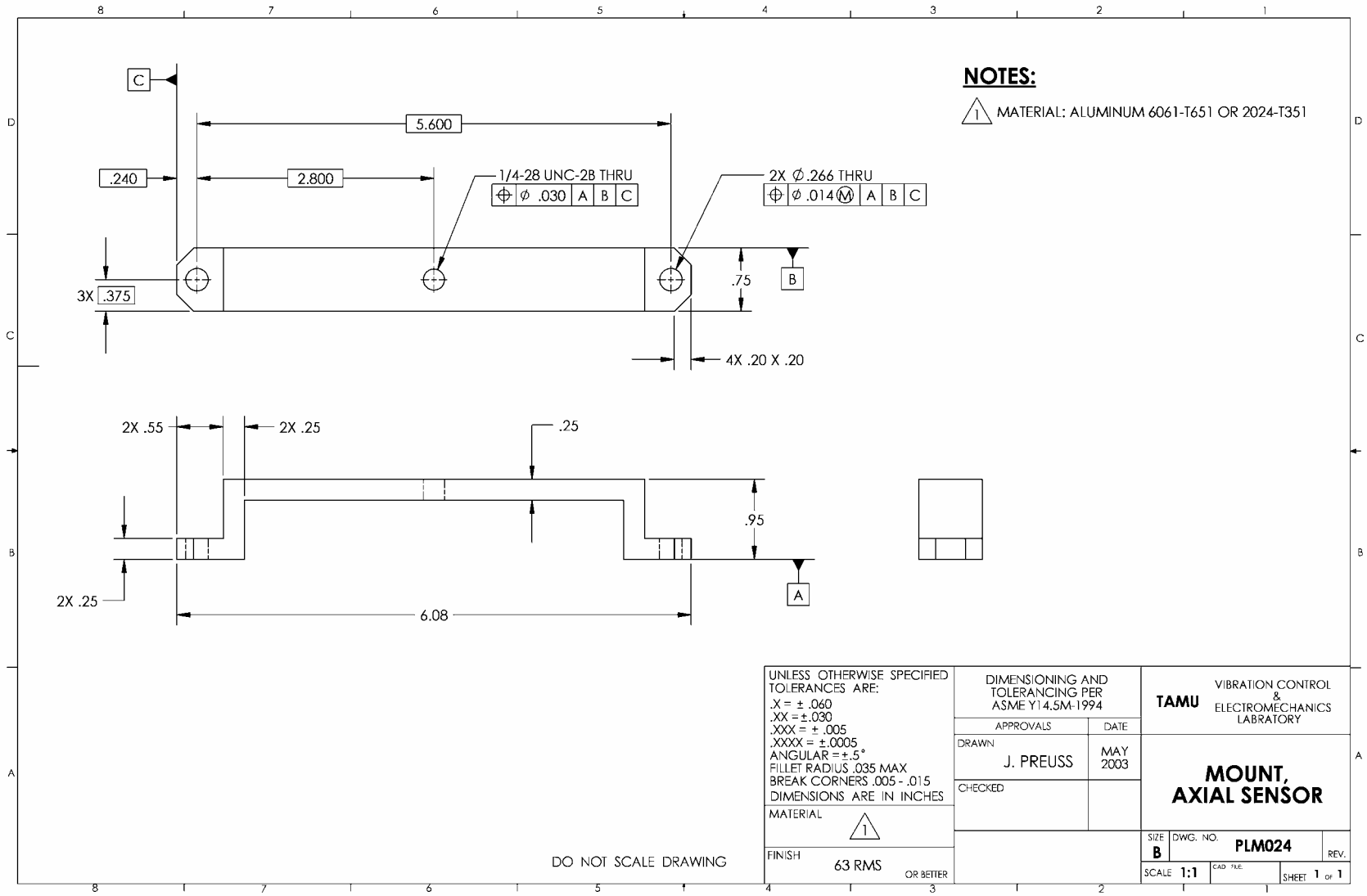
C
5.600
.240
2.800
1/4-28 UNC-2B THRU
⌖ Ø .030 A B C
2X Ø.266 THRU
⌖ Ø .014 M A B C
3X .375
.75
B
4X .20 X .20
2X .55
2X .25
.25
.95
2X .25
A
6.08
NOTES:
1 MATERIAL: ALUMINUM 6061-T651 OR 2024-T351
UNLESS OTHERWISE SPECIFIED TOLERANCES ARE:
.X = ± .060
.XX = ±.030
.XXX = ± .005
.XXXX = ±.0005
ANGULAR = ±.5°
FILLET RADIUS .035 MAX
BREAK CORNERS .005 - .015
DIMENSIONS ARE IN INCHES
MATERIAL 1
FINISH 63 RMS OR BETTER
DO NOT SCALE DRAWING
DIMENSIONING AND TOLERANCING PER ASME Y14.5M-1994
APPROVALS DATE
DRAWN J. PREUSS MAY 2003
CHECKED
TAMU VIBRATION CONTROL & ELECTROMECHANICS LABRATORY
MOUNT, AXIAL SENSOR
SIZE B DWG. NO. PLM024 REV.
SCALE 1:1 CAD FILE SHEET 1 OF 1

NOTES:

1. REFERENCE MATERIAL: NdFeB CYLINDRICAL MAGNET FOR KOFORD 1.6" BRUSHLESS FRAMELESS MOTOR. SPECIAL ORDER MAGNET WITH 5/16" BORE VS. 1/4" STOCK BORE.

△2 CHAMFER TO CLEAR .025-.035 SHAFT RADIUS.

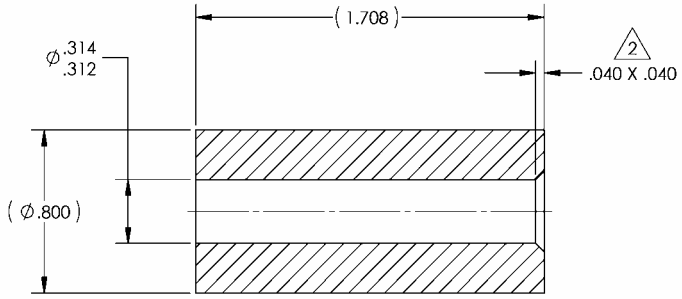

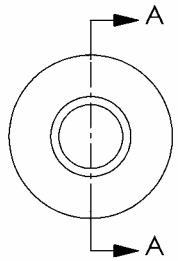

SECTION A-A

DO NOT SCALE DRAWING

UNLESS OTHERWISE SPECIFIED TOLERANCES ARE: .X = ± .030 .XX = ± .010 .XXX = ± .005 .XXXX = ± .0005 ANGULAR = ± .5° FILLET RADIUS .035 MAX BREAK CORNERS .005 - .015 DIMENSIONS ARE IN INCHES	DIMENSIONING AND TOLERANCING PER ASME Y14.5M-1994	TAMU VIBRATION CONTROL & ELECTROMECHANICS LABRATORY
MATERIAL	APPROVALS / DATE	
FINISH	DRAWN J. PREUSS — MAY 2003	**MAGNET, KOFORD 1.6" FRAMELESS BRUSHLESS DC MOTOR, MODIFICATIONS**
	CHECKED	SIZE B — DWG. NO. PLM025 — REV.
		SCALE 2:1 — CAD FILE — SHEET 1 OF 1

NOTES:

1. DIMENSIONS MEASURED 06/25/03 FROM KOFORD MOTOR WITH ETCHING "VCEL #2" ON O.D.
2. REMOVE MATERIAL FROM THIS FACE TO ACHIEVE ASSEMBLED DIMENSIONED DESCRIBED IN PLM001, PAGE 4, NOTE 1. .015" NOMINAL AMOUNT OF MATERIAL TO BE REMOVED.

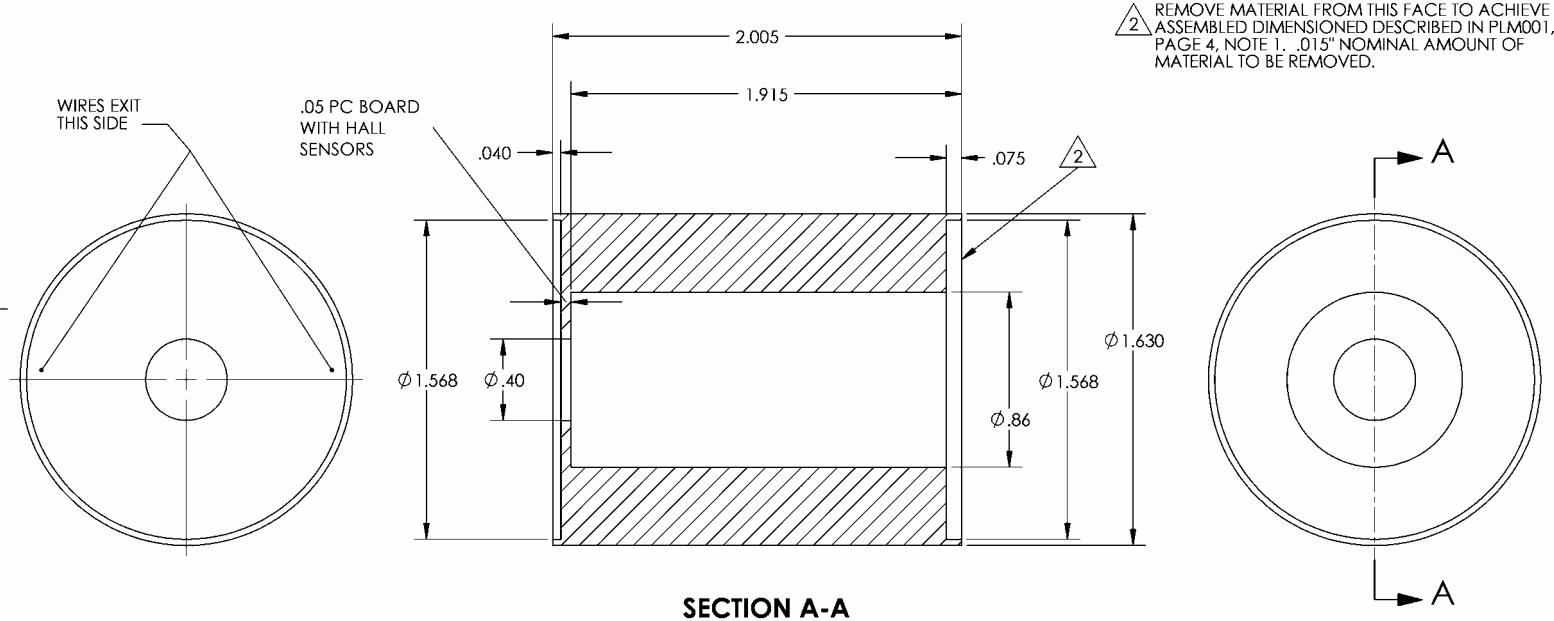

SECTION A-A

UNLESS OTHERWISE SPECIFIED TOLERANCES ARE: .X = ± .030 .XX = ±.010 .XXX = ± .005 .XXXX = ±.0005 ANGULAR = ±.5° FILLET RADIUS .035 MAX BREAK CORNERS .005 - .015 DIMENSIONS ARE IN INCHES	DIMENSIONING AND TOLERANCING PER ASME Y14.5M-1994	TAMU VIBRATION CONTROL & ELECTROMECHANICS LABRATORY
MATERIAL	APPROVALS / DATE	
FINISH	DRAWN J. PREUSS — MAY 2003	**STATOR, KOFORD 1.6" FRAMELESS BRUSHLESS DC MOTOR, MODIFICATIONS**
DO NOT SCALE DRAWING	CHECKED	SIZE B — DWG. NO. PLM026 — REV.
		SCALE 2:1 — CAD FILE: — SHEET 1 OF 1

VITA

Jason Lee Preuss graduated from Brenham High School in May 1993 and upon graduation began coursework at Blinn College while working in residential construction. Jason transferred to Texas A&M in the spring of 1997 and soon after completed a one year cooperative education position at Sperry-Sun Drilling Services in Houston, Texas. In the fall of 1999 he began employment in the Vibration Controls and Electromechanics Lab (VCEL) at Texas A&M University. In May, 2001 Jason received his Bachelor of Science degree in Mechanical Engineering from Texas A&M University. He continued his education and work at Texas A&M University and was awarded a Master of Science degree in Mechanical Engineering in May, 2004. Jason began employment in January, 2004 with Honeywell (Engines, Systems, & Services: Air Frame Systems) in Torrance, California.

Jason may be reached at the following address:

2758 Old Masonic Road

Brenham, TX 77833

979-836-5715